IMPROVING ELECTROCHEMICAL CAPACITOR PERFORMANCE THROUGH STUDIES OF MANGANESE OXIDE HYDRATION AND REDUCED GRAPHENE OXIDE SELF-DISCHARGE

by

Mallory A. Davis

Submitted in partial fulfillment of the requirements
for the degree of Master of Science

at

Dalhousie University
Halifax, Nova Scotia
June 2018

To Didi, with so much love

Table of Contents

List of Tables

List of Figures

Abstract

Electrochemical capacitors (ECs) store energy in a double layer of charge at an electrode/electrolyte interface and/or through rapid redox reactions. The first project discussed herein is a comprehensive study of the effect drying/storage procedures have on manganese oxide (MnOx)'s performance as an EC material. Capacitive properties are enhanced in hydrous MnOx; power-related properties are enhanced in anhydrous MnOx. A novel film synthesis combining hydrous and anhydrous films is developed, generating films with benefits of both hydrous and heat-treated MnOx.

The second project discussed herein addresses self-discharge (SD), a spontaneous potential loss following charging, in reduced graphene oxide (rGO). Carbon oxidation is a minor contributor to SD, while charge redistribution, the spontaneous movement of charge within a material, causes significant SD. Differentiating between these phenomena proves challenging; both processes present similar SD profiles. A method to discern between these mechanisms is presented, determining both processes contribute to rGO SD.

List of Abbreviations and Symbols Used

A	ampere
A	electrode area
A	symmetry factor
AC	activated carbon
C	coulomb
°C	degrees Celsius
c_o	concentration (of species responsible for self-discharge)
CE	coulombic efficiency, counter electrode
CNT	carbon nanotube
C_{Qdep}	capacitance (normalized to deposition charge)
CR	charge redistribution
CV	cyclic voltammetry/cyclic voltammogram
D	diffusion coefficient
E	energy
E_a	anodic energy
E_B	binding energy
E_c	cathodic energy
EC	electrochemical capacitor
EDLC	electrochemical double-layer capacitor
EE	energy efficiency
E_{If}	float current potential
E_K	kinetic energy

F	farad
F	Faraday's constant (96 485 C mol^{-1})
GC	glassy carbon
GCD	galvanostatic charge/discharge
h	Planck's constant (6.626 x 10^{-34} $m^2kg\ s^{-1}$)
H_{upd}	hydrogen underpotential deposition
i	current
I_a	anodic current
$I_{a,\ 0.3\ V}$	anodic current at 0.3 volts
ICP-OES	inductively-coupled plasma optical emission spectroscopy
I_f	float current
i_o	exchange current density
I_p	peak current
I_{test}	constant current applied in galvanostatic charge/discharge test
$I_{0.58\ V}$	current at 0.58 volts
J	Joule
M	molar
MnOx	manganese oxide
OCP	open-circuit potential
OCV	open-circuit voltage
Ox-NS	oxidized negative-sweep
Ox-PS	oxidized positive-sweep
P	power

Q_{ch}	charging charge (cathodic)
Q_{dch}	discharging charge (anodic)
Q_{dep}	deposition charge
Q_i	charge at point i
R	resistance
R	gas constant
RE	reference electrode
rGO	reduced graphene oxide
SCE	saturated calomel electrode
SEM	scanning electron microscopy
SHE	standard hydrogen electrode
t	time
T	temperature
t_{test}	time of discharge during galvanostatic discharge
TGA	thermogravimetric analysis
UnOx	unoxidized
V	volt
V	potential
V_{drop}	potential drop due to ohmic resistance
V_i	initial potential
V_{max}	maximum potential
V_t	potential at time t
V_{test}	potential window of galvanostatic discharge, excluding iR drop

W	watt
W	work function
Wh	watt-hour
XPS	X-ray photoelectron spectroscopy
z	charge
v	speed of light (2.998×10^{8} m s^{-1}), sweep rate
Ω	ohm
τ	integration constant
>	greater than
<	less than

Acknowledgements

Firstly, I would like to thank my supervisor, Dr. Heather Andreas, who has taught me so much, from how to write and present better to how to improve my critical thinking, and how to believe in myself as a scientist. She has been endlessly encouraging, inspiring, and supportive, especially through the difficult times during my Master's when things were overwhelming. I honestly do not think I could have completed this degree without her advice, both with regards to research and theories, but also with how to tackle the challenges life can throw at you, and I could not have imagined doing graduate school under anyone else. I really enjoyed my MSc. experience and I owe it all to her. She is the sweetest and smartest human being, and it was an absolute pleasure to work for her.
I would also like to acknowledge my committee members, Dr. Mita Dasog and Dr. Peng Zhang, for your advice and input into making this project and thesis the best it could be.

In addition, I would like to acknowledge several other Faculty and Staff members of Dalhousie who helped me along the way. A special thank you to Todd Carter, for being an amazing glass blower and making and fixing so many important things for our lab. I also owe thanks to Dr. Alex Speed for the use of his oven and sonicator when ours were broken, and for lending a helping hand when no one else was around the department during my early mornings, and to Dr. Alan Doucette for the use of his deionized water machine when ours was out of commission. Dr. Jeff Dahn and Dr. Robbie Sanderson also deserve thanks for allowing me to use their TGA and for training me on it, respectively, and I am also grateful to Andy George for running my XPS samples. I would like to express my gratitude to Dr. Ping Li and Dr. Pat Scallion for helping me collect SEM images and to Dr. Alicia Oickle for helping run ICP-OES samples.

Next, I would like to give a huge thank you and big hug to all the members of the Andreas lab, past and present. In particular, Dr. Justin Tom, thank you for being a fountain of knowledge and showing me how to do pretty much everything, from XPS fitting to changing gas tanks (and for supplying me with forks for all the times I forgot to pack one in my lunch). Adrienne Allison, I am so grateful to have had you by my side in this lab since I started. You are so smart and talented, not just in electrochemistry, but in literally everything (especially baking – thank you for all the deliciousness you brought to the office to share). I could not have asked for a better crossword buddy, trivia buddy, tea buddy, and someone to bounce ideas and theories back and forth with. We started out as coworkers but now you are genuinely one of my best friends, and I cannot wait to see all the impressive work you will do as you complete your degree. You are actually one of the kindest, most intelligent and genuine people I know and I am confident you will do amazing things in life. Alex Hare and Felicia Licht, thanks for being a great addition to our lab. You are both honours student supremes and it was a pleasure working with you. Alex, you are such a pleasant and thoughtful person and I think you will do fantastic as your switch focus from chemistry to psychology – you were definitely meant to help people and be a source of comfort and inspiration. Felicia, you are a so much fun to work with and can always make me laugh and have made such a contribution to Dal for helping create an amazing new undergrad lab based on experiments we do every day. I am looking forward to seeing what you do next.

Matt Adams, thank you for being the main reason I could finish this degree. No matter how stressed and overworked you were from your own research, you were always there for me, bringing me tea on bad days and poutine on really bad days, being my

shoulder to cry on, and being a good listener when I woke up in the middle of the night super overthinking data. Thank you for always believing I could do this, being understanding when I had to stay late in the lab, and watching so many of my practice runs of my presentations. Thank you for all the hugs, the times you brought me lunch, and the times you would just sit there with me whenever I needed comfort. I think I developed into a better person from spending my undergrad and MSc. with you. You are my favourite person and I am so proud of you, always. Love you.

Finally, I would like to thank my parents for doing so much for me over my years at Dal and my entire life. All the times you were my chauffeur, all the times you changed your schedule around to fit when I needed to be in the lab, all the meals you made for me, every time you helped with errands when I was just too busy – I am so grateful. Love you both so much. Thank you for always being on my team and supporting me through everything I do. I will miss you guys so much as I move to start my finally-done-school life, but don't worry – I'll visit often, and you're always welcome to come visit me too

Chapter 1 Introduction

Electrochemical capacitors (ECs), also known as supercapacitors, are energy storage devices that can store charge in two different ways. The first is double-layer charge storage, which stores charge electrostatically between a layer of charge on the electrode's surface and a layer of oppositely charged ions in the electrolyte[1–3]. The second method is pseudocapacitance, which stores charge in very rapid redox reactions, intercalation, or adsorption processes[2–4]. Of the two processes, double-layer charge storage is higher power, a consequence of the speed at which formation/relaxation of the double layer can take place[5], but pseudocapacitive charge storage is higher in energy[1]. High-surface-area carbon materials are often employed in double-layer ECs[5]; the large surface area allows for a larger double layer and therefore more stored charge. While certain functional groups present on carbon, such as quinones, can participate in pseudocapacitance[2,6–8], transition metal oxides and electronically conductive polymers are more typical pseudocapacitive materials[9]. In this work, reduced graphene oxide (rGO) and manganese oxide (MnOx) are examined as a high-surface-area carbon and pseudocapacitive EC material, respectively.

ECs are advantageous in that they can charge and discharge rapidly, outperform other charge storage devices such as batteries in terms of cycle life, and offer elevated power densities[2,5,10,11]. This permits ECs to step in when other devices might fail, such as powering the emergency exit on aircraft[12] or a camera flash[13,14], or in accelerating an electric vehicle[9,15], applications which all require a lot of charge to be supplied in a brief

time frame. However, ECs require substantial improvement in a few key areas in order to expand their range of applications.

One area where ECs fall short is their low energy densities in comparison to batteries and fuel cells[16–19]. Another problem, applying especially to pseudocapacitive materials, is their poor stability[9]. For example, MnOx commonly dissolves with long-term cycling[9,20–25]. Electrode preparation, including heat treatment methods that impact degree of hydration, influences the performance of pseudocapacitive materials. Thus, identifying an appropriate drying/storage procedure proves pivotal in minimizing both stability and energy concerns. In general, literature results suggest a trend where more hydrous MnOx has higher capacitance[26–30], and therefore higher energy. However, heat-treated films have offered improved stability[26,31] and low resistance[30–32], which is critical for the high-power applications in which ECs are commonly used. While these figures of merit are essential to EC performance, the relationship between degree of hydration and other important parameters, such as film usage, power, and energy efficiency, have been under-examined.

Anhydrous transition metal oxide films are known to provide enhanced electronic conductivity[26,33], but hydrous regions are required to promote the cation movement and insertion necessary for pseudocapacitance[2,28,34,35]. Clearly, a thorough evaluation of the effect hydration has on all parameters related to the electrochemical performance of MnOx in one unique system is required. Thus, the work presented in Chapter 4 provides an in-depth evaluation of how hydration impacts a vast scope of electrochemical properties. Five drying/storage conditions are examined to evaluate how film hydration

influences capacitance, energy and energy efficiency (EE), power, film usage, coulombic efficiency (CE), resistance, cycle life, and physical stability.

The work comprising Chapter 5 builds on the findings discussed in Chapter 4 and presents a novel film synthesis that combines both heat treatment and wet storage in order to generate a stable, low-resistance MnOx film without sacrificing high capacitance and energy. This method, termed the double-deposition method, merges heat-treated and hydrous MnOx. A variety of ratios of heat-treated to hydrous films are examined to identify the balance of ionic to electronic conductivity necessary to generate an optimized film that performs well across all electrochemical figures of merit. Using the knowledge obtained regarding how hydration impacts MnOx performance, thoughtful selection of a drying/storage method can be employed to optimize device performance based on the desired application. In addition, the innovative double-deposition presented herein could be applied to a variety of substrates to further optimize MnOx electrodes for EC applications.

A second drawback prevalent with ECs, addressed in the second project presented in this thesis, is their high degree of self-discharge (SD). SD is the spontaneous decline of potential that occurs following charging when a device is left in open-circuit configuration[36]. Several factors can contribute to SD such as ohmic leakage, or a diffusion- or activation-controlled parasitic Faradaic reaction[37–39]. Conway *et al*. developed a model to identify and distinguish these SD mechanisms by examining the SD profile plotted in different ways[37–39].

However, a fourth mechanism of potential loss exists: charge redistribution (CR). CR is the spontaneous movement of charge throughout electrode pores that takes place to

eliminate a potential gradient within the pores and has been identified as a significant contributor to SD in porous materials[40–47]. Following charging, a potential gradient exists within a material because the potential at the pore base does not necessarily match the potential at the pore opening[48–50]. This is because the movement of ions within a pore is necessary for both formation of the double layer and for regions deep within the pores to partake in pseudocapacitance. However, the increased solution resistance ions experience moving to the base of a pore compared to accessing a pore tip causes potential changes to happen slower deep within pores than at the pore mouths, resulting in a non-uniform potential throughout the pore[48–50]. This potential gradient provides a driving force for CR to take place to equalize the potential, which complicates the analysis of SD for porous carbons in aqueous electrolyte in which both activation-controlled oxidation[36] and CR can arise[40]. This is because separation of SD due to CR and an activation-controlled reaction poses a challenge since both mechanisms result in similar SD profiles[36,40] when applying Conway's[37–39] method.

For carbons, SD is generally amplified when oxygen- and nitrogen-containing functional groups are present on the carbon surface[7,51–54]. Recently, Oickle and coworkers reported a direct relationship between degree of carbon oxidation and the extent of SD for Spectracarb 2225 carbon cloth in aqueous electrolyte, identifying activation-controlled oxidation as a cause for SD[36]. Even more recently, Subramanian and coworkers identified CR as the primary process responsible for SD of graphene-based ECs with organic electrolyte[47]. In general however, the SD of reduced graphene oxide (rGO) is considered widely underexplored[15].

Herein, the mechanism of SD of rGO, a material of interest owing to its high surface area and electronic conductivity[15,55], is examined. Aqueous electrolyte was chosen as it represents a less toxic and safer alternative to organic electrolytes[56] and is expected to reduce the effect of CR as a result of its smaller ion sizes[57]. However, aqueous solution introduces carbon oxidation as a possible cause for SD[36]. These findings highlight the need to study rGO SD in more depth and to determine a way to separate CR from activation-controlled oxidation as mechanisms of SD.

The work presented in Chapters 6 and 7 offers a detailed analysis of how carbon oxidation and CR impact the potential loss of rGO. Chapter 6 employs the float current (I_f) method, whereby a current is recorded as a function of time during a potentiostatic hold, and this I_f is considered equal to the SD current[39]. I_f studies primarily evaluate differences in potential loss as a consequence of how susceptible the rGO is to oxidation. Adjustments to the electrochemical cycling procedure used to induce carbon oxidation are briefly discussed.

Chapter 7 examines rGO SD in greater depth via repetitive open-circuit SD measurements. Performing multiple charge/SD cycles allows the effects of both the carbon becoming more oxidized[36] and the carbon becoming more fully charged (smaller potential gradient within its pores)[46] with cycling to be addressed. By performing multiple charge/SD cycles on oxidized rGO, the effect of the carbon becoming more fully charged with cycling can be evaluated without the carbon's degree of oxidation as a variable. However, in the case of unoxidized rGO, whether CR or oxidation is the primary contributor to potential loss cannot be determined by this method alone. Thus, a novel method to separate SD due to CR and due to oxidation is developed and employed.

A CR reset step, designed to keep the potential gradient within the carbon, and therefore the extent of CR, constant between all SD cycles is applied to the rGO. This allows the SD as a result of oxidation to be isolated.

Identifying multiple SD mechanisms taking place in a system and establishing which mechanism dominates potential loss is crucial to minimize SD and design more reliable devices, especially since two prevalent SD mechanisms, activation-controlled Faradaic SD and CR, present similar SD profiles[37–40]. The method of oxidation and CR resetting applied to rGO in Chapter 7 is likely applicable to other carbons in which both processes may cause SD. The deeper understanding of the role both carbon oxidation and CR play gained from this work can not only be drawn upon to reduce EC SD, but proves fundamental to the interpretation and current understanding of SD data.

Overall, the work incorporated into this thesis provides valuable insight into how to improve two different EC materials through investigating how manipulating their properties influences their performance. With respect to MnOx films, a systematic evaluation of how their degree of hydration affects their ability to store, retain, and deliver energy, their stability, their rate capability, and other figures of merit is presented. The knowledge gained regarding the relationship between degree of hydration and electrochemical performance is then applied in the development of an innovative synthesis combining heat-treated and hydrous MnOx. Concerning rGO, a method of separating SD due to CR and SD as a result of carbon oxidation through resetting the degree of CR between consecutive SD cycling is presented. The relationship between rGO's degree of oxidation and the extent of its SD is examined and how potential gradients within the carbon and the resulting CR impact its SD is discussed.

Chapter 2 Background

2.1 Energy Storage Devices and Electrochemical Capacitors

While many energy storage devices exist, including ECs, fuel cells, and batteries, in general the application decides which device is most appropriate to use. ECs, also called supercapacitors, posses high power densities and the ability to undergo rapid charging and discharging[2,5]. This results in their use in applications where considerable charge needs to be applied in a brief time frame[2,5]. As an example, batteries can take 1-5 hours to charge and 0.3-3 hours to discharge, while 0.3-30 seconds is adequate time for EC charging and discharging[11]. Thus, ECs are often used in camera flashes[13], power tools[10], or emergency exit doors on aircraft[12], due to their high power capabilities, or to reduce fuel consumption in buses, electric trains, or waste management vehicles because the brief time spent braking is sufficient to recharge the EC for use during acceleration[10,58].

In addition, ECs posses a high cycle life[10] and function over a broad temperature range, allowing them to be used in remote applications where replacing the energy storage device poses a challenge or when keeping the device at a specific temperature proves costly[58]. While batteries may have cycle lives of several thousands of cycles, EC cycle lives commonly reach between hundreds of thousands to millions of cycles[2,11]. ECs are often considered the device that fills the gap between batteries and traditional capacitors as they possess energy densities greater than those of parallel plate capacitors, and greater power densities than batteries, but are currently incapable of achieving the high energy densities available with batteries[16–19].

2.2 Types of Charge Storage in Electrochemical Capacitors

2.2.1 Double-Layer Charge Storage

ECs use two methods to store charge. The first is double-layer capacitance, where charge is stored between a layer of charge on the electrode surface and a layer of oppositely charged ions in solution[1–3], resembling a parallel plate capacitor. Electrical double-layer capacitors (EDLCs) store charge in this way. The current response as a function of potential during charging and discharging of an EDLC is thus similar to the response of a conventional capacitor (*i.e.* rectangular, and with a current that switches sign but not magnitude immediately upon switching from charging to discharging)[3]. A diagram of an electrochemical double layer formed at a positive electrode, modeled after Winter[5] is shown in Figure 2.1. Oppositely-charged ions (relative to the charge on the electrode) exist in excess nearest the electrode surfaces, but multiple layers of positively and negatively charged ions build up around the surface[59] and the extent of ion build up at the electrodes is related to the applied potential[17]. A pure EDLC will store charge exclusively in the double layer and have no charge transfer across the electrode-electrolyte interface during use[17].

In comparison to the Faradaic methods of charge storage (*e.g.* pseudocapacitance, Section 2.2.2), double-layer capacitance is a high-power process[2]. Since the formation and relaxation of the double layer only requires the movement of ions, rather than charge transfer or a chemical reaction, it occurs very rapidly ($\sim 10^{-8}$ s)[5]. However, the electrical double layer only stores approximately 0.2 electrons per surface atom[2], making this process much lower in energy in comparison to Faradaic charge storage. Typical

materials for double-layer capacitors include high-surface-area carbons[5]; a large accessible surface area will maximize the charge stored in the double layer.

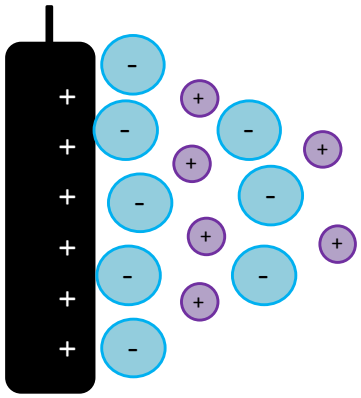

Figure 2.1. Simplified diagram of the electrochemical double layer formed at a positive EC electrode, modeled after Winter[5].

2.2.2 Pseudocapacitance

The second method of charge storage is pseudocapacitance, which stores charge in very fast redox reactions, adsorption reactions, or by intercalation[2–4]. The term 'pseudocapacitance' is derived from the highly reversible nature of the redox reactions, which provide electrochemical responses that are similar to a conventional capacitor's charge storage[4]. Since pseudocapacitance requires a reaction to take place (~10^{-4} to 10^{-2} s for the redox reactions to occur)[5], it is a slower, lower power method of charge storage compared to double-layer capacitance. In contrast, ten to one hundred times more energy can be stored via pseudocapacitance in comparison to within a double layer[1]. This is the result of one or more electrons stored per surface atom[2], with the number of electrons stored per atom equaling the number of electrons passed in the redox reaction responsible for pseudocapacitance. With pseudocapacitive systems, the potential of the electrode continuously influences the amount of oxidation or reduction occurring[2–4], rather than diffusion of electroactive species or an activation energy barrier. Thus, pseudocapacitive

systems follow Nernstian control; at a given potential the redox-active species will react rapidly to adjust the relative concentrations of the oxidized and reduced species to satisfy the Nersnt equation and the system is always at equilibrium[2,3].

Pseudocapacitive behaviour is generally characterized by mirror-image cyclic voltammetry responses where the anodic and cathodic currents reflect each other across the zero current axis[4,11,60]. In addition, relatively rectangular cyclic voltammograms (CVs), resembling CVs of traditional capacitors or double-layer ECs, are also indicative of pseudocapacitive behaviour[61,62]. Transition metal oxides of Ni, Co, Ru, and Mn, and electronically conductive polymers are common pseudocapacitive materials[9].

2.3 Manganese Oxide as a Pseudocapacitive Electrode Material

Recently, manganese oxide (MnOx, *e.g.* MnO_2, Mn_2O_3, *etc.*) has gained prominence as a pseudocapacitive electrode material due to its environmental compatibility, abundance, low toxicity, and low cost in comparison to other common transition metal oxides[9,13,20]. Additionally, MnOx electrodes display pseudocapacitive behaviour in Na_2SO_4, avoiding the use of the strongly acidic or basic electrolyte necessary for other materials such as ruthenium and nickel oxides[63].

Oxides and hydroxides of a variety of metals, including but not limited to Fe, Ni, Sn, Bi, Mo, Ti, and Co demonstrate pseudocapacitance, but possess disadvantages such as an impractical, low potential window in the case of Co and Ni, or large volume changes in the case of Co that limit their application in ECs[9]. Although iron oxides can provide a low-cost alternative to other metal oxides and pose no considerable environmental concern, poor electronic conductivity, low capacitance, and inadequate cycle life render their use in commercial applications currently unfeasible[9]. While certain

conducting polymers also exhibit pseudocapacitance, transition metal oxides are generally more stable as polymer expansion and shrinkage as a result of the ion intercalation required for pseudocapacitance results in device degradation[9]. While safety, availability, and cost considerations highlight MnOx as a promising candidate for electrode materials, much work still needs to be done to address common problems with MnOx, such as film dissolution, which is often observed upon long-term cycling[9,20–25].

2.4 Hydration and Capacitance in Transition Metal Oxide Films

MnOx demonstrates pseudocapacitance through Faradaic reactions involving changes in the Mn transition state with reversible insertion and removal of cations from solution to balance charge[64]. One example of a possible pseudocapacitive reaction of MnOx is shown below, where X^+ represents a proton or solution cation (*e.g.* Na^+)[19]:

$$MnO_2 + X^+ + e^- \leftrightarrow MnOOX.$$

Cation mobility within a transition metal oxide film is enhanced by hydrous areas in the film[2,34,65]. As a consequence, films possessing a greater degree of hydration (and therefore improved cation mobility) are expected to afford improved capacitance as the result of a greater contribution from pseudocapacitive charge storage[28]. Thus, it is evident drying and heat-treatment methods used in electrode preparation should significantly influence device properties and performance.

In the literature, an increased heat-treatment temperature often results in decreased capacitance for pseudocapacitive transition metal oxide films[26,28–30,66], consistent with the elimination of hydrous sites upon removal of water during heating limiting pseudocapacitance. However, some debate over the effect of heat treatment exists since different groups have found conflicting results. For example, Dolah and

coworkers found a 70 °C heat-treatment temperature results in the highest capacitance for MnOx films[32]. Zhu *et al.* observed improvements in capacitance with increasing heat-treatment temperatures up to 500 °C[67] and other groups found a 200 °C heat treatment to offer enhanced capacitance compared to electrodes dried at both higher and lower temperatures[68,69].

Of course, high capacitance is not the only desirable property in an EC. Stability is also a concern. Some groups have achieved enhanced electrochemical stability by applying an appropriate heat treatment[26,31]. This is observed as an enhanced retention of capacitance with long-term cycling, even if initial capacitance at the beginning of cycling is lower for the heat-treated sample[31].

While high-temperature drying removes hydrous sites in the film and therefore negatively impacts ionic diffusivity, water content in a film is known to elevate the electronic resistivity of the film[26,33]. Confirmation of this phenomenon has been provided in the literature, where annealed films demonstrate lower resistance[30,31]. Thus, it is evident conflict between ionic versus electronic mobility within the film as well as stability concerns highlight the need for a more thorough investigation of the effects of heat-treating pseudocapacitive materials and the development of a novel film treatment method to improve the properties of MnOx films to widen their range of applications. The work discussed in this thesis addresses the inconsistency in the literature regarding how heat treatment influences capacitance, resistance, and charge retention, while also providing a thorough analysis of how degree of film hydration impacts other electrochemical properties critical to EC performance, such as coulombic efficiency and power, that have yet to be related to degree of hydration.

2.5 Reduced Graphene Oxide as an Electrode Material

Electrochemical double-layer EC electrodes are often composed of high-surface-area carbons. This is because carbon is a low-cost, environmentally friendly, and abundant material, and a large surface area means a greater amount of energy can be stored in the double layer. In fact, over 80% of the total commercially available ECs are carbon-based double-layer ECs[15]. Many forms of carbon are available for use in ECs. Activated carbon (AC) is one of the most prevalent because it is readily available and offers a low price[15]. Yet, the extremely small pores of AC mean all the surface area of the AC is not necessarily accessible to electrolyte and is therefore not able to participate in charge storage[15,70]. Furthermore, heteroatoms present in AC hinder EC power capabilities through restricting conductivity[71]. Carbon nanotubes (CNTs) are also an attractive EC material, but their costly nature[71], low surface area[12], and tendency to clump together as a result of strong interactions between CNTs limits their use[15,17] . Templated carbon and onion-like carbons have also been investigated but demonstrate only modest capacitance and are relatively expensive[71].

Graphene, a two-dimensional, sp^2 carbon material, offers high electrical conductivity, flexibility, and mechanical strength in parallel with a large surface area, highlighting its potential use as a double-layer EC material[71,72]. Reduced graphene oxide (rGO), made by thermal, chemical, or electrochemical reduction, shows properties similar to that of pristine graphene[73], and is generally easier to synthesize. While the reduction of graphite oxide is deemed an affordable method of generating large quantities of graphene, rGO cannot be considered the same as graphene since residual oxygen-containing functionalities, lattice defects, and sheet aggregation alter the material's

properties[71,73–75]. The electrochemical behaviour of graphene varies considerably as a result of differences in production method, pore size, surface area, and surface heteroatom presence[15,71,72,76]. As the above listed properties are not unrelated, determining an exact relationship between capacitance and these parameters poses a significant challenge[15]. In addition, a detailed investigation of the self-discharge processes that arise in graphene-based ECs has not been widely explored[15]. Like many other carbons, rGO can be oxidized via cyclic voltammetry in acid (shown in results), thus allowing for an *in situ* method of determining the degree of oxidation[36] of the carbon. This feature, coupled with the current lack of knowledge on the self-discharge of graphene materials in acidic-aqueous electrolyte, inspired the rGO aspect of this research.

2.6 Self-Discharge

While features like high power capability and long cycle life make ECs attractive for many applications, a significant problem with ECs that limits their employment is a high degree of self-discharge (SD). SD is the spontaneous loss of potential that occurs upon opening of the circuit following charging[36]. The process occurs because a charged electrode is in a higher energy state relative to a discharged electrode[37]. Therefore, if a pathway to lose charge is available, the electrode will undergo SD to return to a lower energy state[37]. This potential loss is problematic as many ECs are used in devices that rest idle for the majority of their lifetimes but are heavily relied on to work when the need arises (*e.g.* back-up power supply[16] or emergency exit doors[12]). If too much charge is lost, the EC may no longer be able to do its job when it is required; thus it is evident SD greatly reduces the reliability of the device[37].

Conway and coworkers developed a model to analyze potential changes in open-circuit SD measurements vs. time, log(time), and time$^{1/2}$ to distinguish between three SD mechanisms: diffusion-controlled reactions, activation-controlled reactions, and ohmic leakage[37–39]. Diffusion-controlled SD arises when a redox active impurity present in electrolyte in low concentrations undergoes oxidation or reduction at the electrode surface[37–39]. One example includes iron contaminants present in electrolyte which can shuttle between both electrodes alternating between Fe^{2+} and Fe^{3+} and discharging both electrodes in the device[37–39]. In such a situation, the potential decay is described by deriving Fick's law of diffusion and results in a potential decay that is linear in square-root time by Equation 1[37–39];

$$V_t = \frac{V_i - 2zFAD^{1/2}\pi^{-1/2}c_0}{C} t^{1/2} \quad (1)$$

where C is the electrode capacitance, V_i and V_t are the initial voltage and the voltage at a particular time, t, respectively, z is the charge on the redox-active ion, F is Faraday's constant, D is the diffusion coefficient of the redox species in electrolyte, A is the electrode area, and c_0 is the concentration of the species responsible for SD[37–39].

The activation-controlled SD scenario arises when the reaction responsible for SD is not limited by waiting for the arrival of the reactive species at the electrode surface[77]; in this case, the species causing SD is either present in high concentrations (*e.g.* the electrolyte) or present on the electrode's surface (*e.g.* surface functional groups)[77]. The potential decay in this situation is derived from the Butler-Volmer equation, and is described by the following Equation 2, where R is the gas constant, T is the temperature,

i_o is the exchange current density, and α is the symmetry factor, and τ is the integration constant[37–39]:

$$V_t = -\frac{RT}{\alpha F} ln \frac{\alpha F i_0}{RTC} - \frac{RT}{\alpha F} ln \left[t + \frac{C\tau}{i_0} \right]. \quad (2)$$

This mechanism of SD thus results in a potential decay that is linear in log(t)[37–39].

A third mechanism of SD is ohmic leakage[37–39]. Such SD occurs only in full-cell ECs and is the result of a mistake in device design or construction causing the device to short circuit[77]. This mechanism is described by Equation 3[37–39],

$$ln\left(\frac{V}{V_i}\right) = -\frac{t}{RC} \quad (3)$$

describing a linear relationship between the natural logarithm of the voltage and time. Since the work reported herein was conducted using a three-electrode half-cell, ohmic leakage is not a concern and thus will not be discussed further.

2.6.1 Charge Redistribution

Charge redistribution (CR) is the spontaneous movement of charge within electrodes when a potential gradient exists between the surface of the electrode and deep within the electrode pores. This potential gradient arises because the surface of an electrode charges faster than the bulk, and the potential at the tips of pore mouths in porous electrodes changes faster than the potential at the bases of the pores[48–50]. This occurs because ions encounter increased resistance as they travel deeper down the length of a pore, both in the form of increasing solution resistance (increased *i*R-drop)[48,49] and if the size of the ion is very close to the size of the pore. As expected, ions experience greater resistance in narrow pores, rather than in larger pores[6].

Since ions are required both to balance the charge in the double layer as well as to insert/adsorb to balance charge in pseudocapacitive reactions, this hindered mobility of ions deeper within a pore results in slower potential changes at the pore base[48,49]. When there is a potential gradient along the length of a pore, and time is given for the charges to redistribute (*e.g.* when an electrode is allowed to rest in open circuit or when an electrode is held potentiostatically), the charges move along the length of the pore to achieve one uniform potential within the pore[49] (Fig. 2.2). As potentials are normally measured at the pore tips, CR is observed as a potential loss[40], although charge is not actually being lost to some parasitic reaction in this scenario, but is rather just lost to the depths of the electrode.

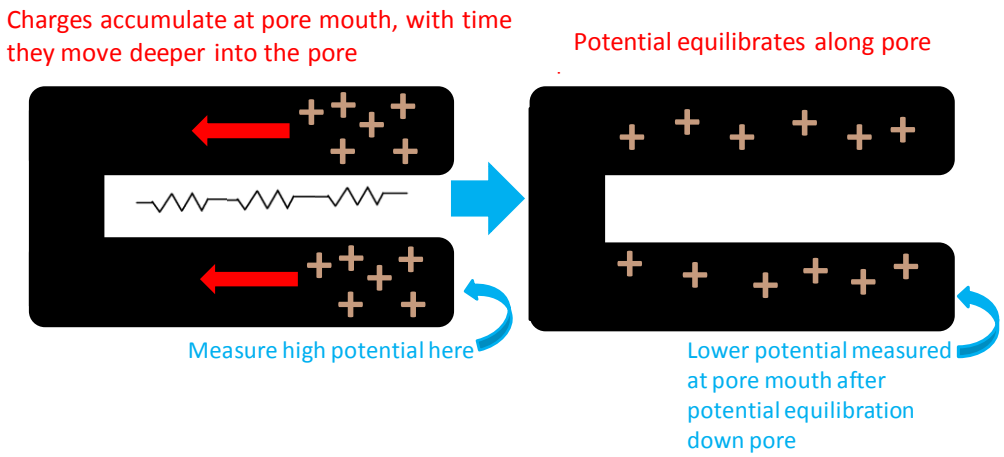

Figure 2.2. Diagram showing charge redistribution down an electrode pore as charges built up on the pore tips have time to distribute and equalize potential down the length of the pore.

CR effects can be minimized by increasing the duration of the charge, but results show that even after up to 75 hours of potentiostatic holding CR effects can still be observed if an electrode has a high abundance of thin, twisted pores[40]. In scenarios where CR plays a significant role, EC history (*i.e.* whether it has been charged and held positively or negatively for a considerable amount of time) prior to SD also becomes

important[44,49]. Potential loss due to CR alone results in the same SD profile as activation-controlled Faradaic SD[40], *i.e.* linear with log(t)[37–39], further complicating SD analysis, especially in systems like carbon where both processes can occur simultaneously.

2.6.2 Electrochemical Methods of Studying Self-Discharge

Two electrochemical tests are typically used to investigate SD in ECs[39,77]. One method involves open-circuit potential measurements, following electrode charging, where the potential decay can be monitored with time (Fig. 2.3a and b). The current drops to zero when the circuit is opened during the open-circuit SD measurement as electrons are unable to flow through the external circuit. Data from such an experiment can be analyzed by viewing the potential profile of the electrode as a function of $t^{1/2}$ and log(t) and applying Conway's model[37,38] and Black's charge redistribution considerations[40].

Alternatively, SD can be measured via potentiostatic holds known as float current measurements in which the electrode is charged to and then held at a desired potential while the current supplied to the electrode is measured as a function of time[39] (Fig. 2.3c and d). The current measured in such an experiment is considered to equal the SD current and is the current required to maintain the desired potential of the electrode through counteracting the SD current[39]. Currents recorded at the beginning of the potentiostatic hold are higher in magnitude than the current at steady state because with time the electrode becomes more fully charged as the surface area within the electrode pores has time to charge, resulting in a diminishing float current after extended holding[39]. Both methods are used in the work presented in this thesis.

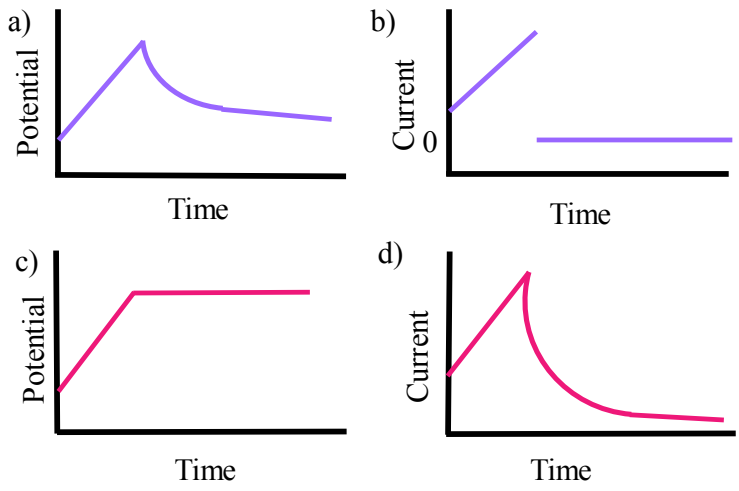

Figure 2.3. Potential and current vs. time curves for open-circuit SD measurements (a-b) and float current measurements (c-d).

2.6.3 Carbon Oxidation and Self-Discharge

It is well-known that the potentials carbon electrodes reach when serving as positive electrodes in ECs are sufficiently high to promote carbon oxidation, converting the carbon to CO and CO_2 as well as oxidizing various surface functionalities[36,38,78–80]. In general, literature data suggests carbon SD is more severe when a greater amount of surface functionalities are present on the carbon[7,51–54]. Zhang and coworkers showed oxidized single-walled carbon nanotubes (SWNT) experienced a greater degree of potential loss than SWNT used as-is, and that chemically reduced SWNT demonstrated even less SD than regular SWNT[53]. This outcome was explained by considering the double-layer interactions only. Zhang *et al.* suggest the presence of oxygen groups on the SWNT surface hinder the electrostatic interaction between ions in the double layer by increasing the interaction distance and decreasing the uniformity of the electrode surface, resulting in weaker electrostatic attraction and easier SD as a result of ions diffusing out of the double layer in nonaqueous electrolyte[53]. Another study found coating carbon

electrodes with a layer of Al_2O_3 could prevent SD by means of blocking parasitic SD reactions of the carbon surface functional groups with organic electrolyte[81].

More recently, carbon oxidation in acidic-aqueous electrolyte, like the electrolyte used in this work, has been identified as a cause of SD[36]. Oickle and coworkers showed Spectracarb-2225 carbon-cloth electrodes that were fully oxidized via cycling in acid displayed significantly decreased SD in comparison to electrodes with carbon cloth used as-received[36]. Additionally, consecutive charging and self-discharging of carbon-cloth electrodes showed a higher final potential following SD (less charge loss) with each charge/SD cycle, indicating the SD reaction was a surface-site-limited process[36]. Furthermore, CVs of unoxidized electrodes following multiple charge/SD cycles evidenced development of large, reversible quinone peaks, indicative of surface oxidation taking place during SD and resembling the final cycle of CVs (representing complete oxidation) for oxidized electrodes[36]. Thus, it is clear that the presence of surface functional groups on a carbon's surface impact its potential loss in a variety of ways. The work presented herein offers insight into how carbon oxidation and CR effects play a role in rGO SD by comparing and contrasting the SD of rGO electrodes with different degrees of oxidation and different potential gradients within their pores. In addition, a method of isolating potential loss due to CR and oxidation is developed, allowing the relative extent to which both mechanisms contribute to rGO SD to be determined.

2.7 Other Electrochemistry Techniques

2.7.1 Cyclic Voltammetry

Cyclic voltammetry is a common technique for investigating electrochemical systems. With this technique, an electrode's potential is increased linearly with respect to

time to a set maximum potential and then the potential is decreased linearly at the same rate to a set minimum (Fig. 2.4). This is repeated for numerous cycles and current is recorded as a function of potential. The resulting plot of collected data is called a cyclic voltammogram (CV). Cyclic voltammetry data can be used to obtain capacitance, energy, energy efficiency, coulombic efficiency (the ratio of charge stored on the electrode to charge delivered during use), and cycle life, as well as potentials where redox reactions occur. Additionally, in this work cyclic voltammetry is used to oxidize rGO.

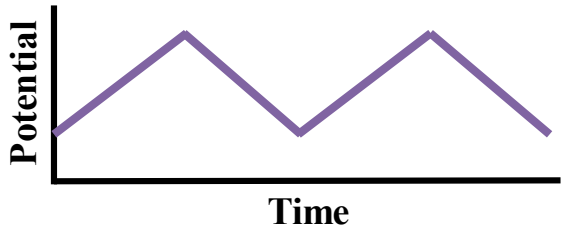

Figure 2.4. Potential profile of a cyclic voltammetry experiment.

Capacitance is defined as the amount of charge stored per volt. Typically, in the field of energy storage, capacitance is reported as specific capacitance, *i.e.* capacitance normalized to mass. Since small and lightweight devices are necessary to power portable or handheld electronics, a device that can store large amounts of energy, but is bulky or heavy, would not be practical in most applications. This makes device properties normalized to mass the standard. However, the masses of the MnOx thin films used in this work could not be accurately measured, thus capacitance values reported herein are normalized to deposition charge (Q_{dep}). Q_{dep}, determined by integrating the current vs. time plot for the deposition of MnOx, is not equivalent to mass, but is proportional to the amount of MnOx deposited and thus serves as an appropriate value to use in data normalization. Capacitance, normalized to Q_{dep} (C_{Qdep}, in F/C), is calculated at a specific potential V during CV cycling using Equation 4:

$$C_{Qdep} = \frac{I_V}{Q_{dep} \times v} \quad (4)$$

where I_V is the current recorded at the desired potential, v is the sweep rate used for the experiment in V s^{-1}, and Q_{dep} is the deposition charge in C.

As with capacitance values, energies (E) reported in this work are normalized to Q_{dep} and are obtained from CV data using Equation 5:

$$E = \frac{\sum Q_i V_i}{Q_{dep}} \quad (5)$$

where Q_i is the charge passed at each point i in the CV and V_i is the potential at that point. Q_i is obtained at each point by integrating the CV between points V_i and V_{i-1} and dividing by the sweep rate. The anodic and cathodic energy, E_a and E_c, respectively, are determined separately for the charging and discharging portion of the CV.

In general MnOx acts as the positive electrode in energy storage devices[13,23,82,83], owing to electrode fading attributed to Mn^{3+} disproportionation occurring at low potentials, which generates tetravalent Mn in MnO_2 and aqueous-electrolyte-soluble Mn^{2+} species[19,21,23,25,84–86]. Therefore, in the experiments discussed herein, MnOx is considered only as a positive electrode and energy efficiency (EE), the ratio of energy released during discharging (E_c) to the amount of energy stored during charging (E_a), can be calculated using Equation 6:

$$EE = \frac{E_c}{E_a} \times 100\%. \quad (6)$$

An EE near or at 100% is optimal in term of applications because it signifies the energy stored on the electrode is available to power a consumer device.

2.7.2 Galvanostatic Charge/Discharge

In galvanostatic charge/discharge (GCD) tests an electrode is charged with a constant positive current to a desired maximum potential and then discharged with a constant negative current of the same magnitude to a set minimum potential (Fig. 2.5). This can be repeated for multiple cycles to evaluate cycle life as well as repeated at various currents to generate Ragone plots[87], logarithmic plots of energy vs. power which are useful in identifying the operational current range of a device[88,89]. Herein, GCD is used to construct Ragone plots and evaluate cycle life, film usage, resistance, and coulombic efficiency.

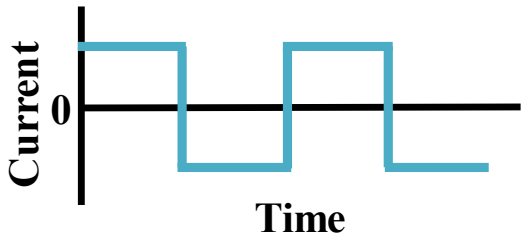

Figure 2.5. Current profile during a galvanostatic charge/discharge experiment.

Ragone plots are often used to compare various charge storage devices[89], and are therefore used to evaluate MnOx films made under various conditions in this work. Ragone plots of ECs typically display a hooked shape, where energy decreases at high power with rapid charging and discharging rates[2,88], as a result of a decrease in accessible surface area for charge storage that arises when ionic and electronic mobility limitations start influencing how much of the film can be accessed with fast-rate charging.

Energy is defined as the ability to do work. If a device has high energy, that means the device can operate for a longer time period before needing to be recharged than a device with lower energy. Power is defined as the rate at which work is done. A device that has high power can move charge more quickly, meaning that the device can

be charged and discharged in less time than a lower power device. Both high energy and high power are advantageous for different applications. As an example, high-energy batteries allow electric vehicles to travel practical distances before requiring recharge, but high-power ECs can complement the batteries by aiding in the acceleration, start up, and up-hill ascent of heavy electric vehicles, and also by allowing for regenerative braking[4,16,17,25,58]. Energy and power densities of MnOx films were determined from GCD curves using the parameters illustrated in Figure 2.6, modeled after Raut[87].

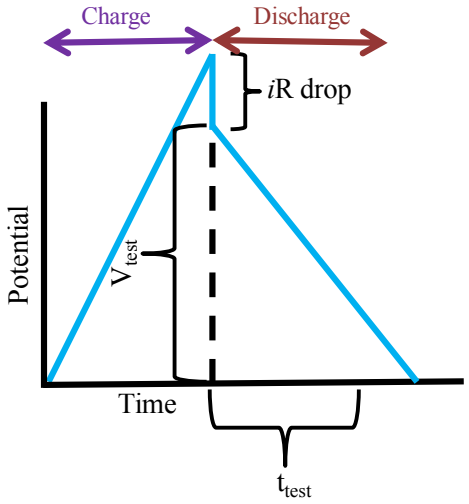

Figure 2.6. Parameters used for calculation of energy and power from GCD data, modeled after Raut[87].

The values were calculated using Raut's method[87], with adaptations to generate values normalized to Q_{dep} rather than mass. Energy (E), in Wh C^{-1}, was determined from the discharge portion of the GCD test using Equation 7[87]:

$$E = \frac{0.75 \times I_{test} \times V_{test} \times t_{test}}{3600 \times Q_{dep}} \quad (7)$$

where I_{test} represents the magnitude of the current applied in the experiment in A, V_{test} represents the potential window used for the discharge in V, with exclusion of the *i*R drop, and t_{test} is the time of the discharge in s, as illustrated in Figure 2.6. Q_{dep} is the

electrode deposition charge. The 3600 constant is included in the energy equation to convert discharge time from seconds to hours. The factor of 0.75 is incorporated into the energy calculation because typically ECs are only discharged to half their maximum potential (V_{max}); discharging an electrode half way means only 75% of the area under the discharge curve (shaded) contributes to the electrode energy, as illustrated in Figure 2.7.

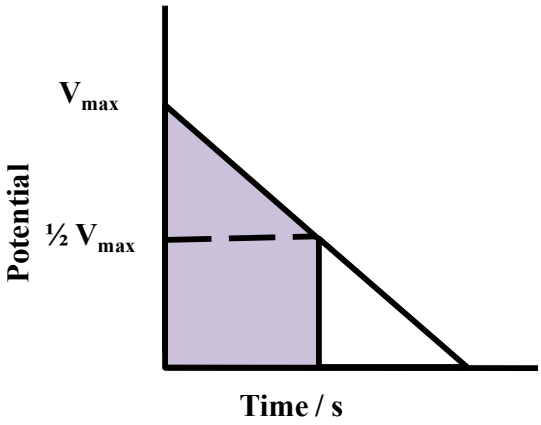

Figure 2.7. Diagram displaying 75% of the area under the discharge curve contributing to electrode energy when an electrode is discharged from its V_{max} to half of that value.

Power (P) is then calculated using the following Equation 8:

$$P = \frac{I_{test} \times V_{test}}{2Q_{dep}} \tag{8}$$

where the factor of two is included in the denominator because maximum power is delivered when the electrode undergoes discharging from the maximum potential to half of that value[2,87].

Coulombic efficiency (CE) is the ratio of charge stored on the electrode to charge removed during discharge. CE is an important parameter because an EC that can store copious amounts of charge is of no benefit if it can only deliver a small fraction of that charge. Integration of the current vs. time plots directly in EC Lab software allows for

determination of charging charge (Q_{ch}) and discharging charge (Q_{dch}). Then, the CE of electrodes can be calculated using Equation 9:

$$CE = \frac{Q_{dch}}{Q_{ch}} \times 100\%. \tag{9}$$

Resistance (R), in Ω, is also obtained from GCD data, by the following Equation 10:

$$R = \frac{V_{drop}}{2I_{test}} \tag{10}$$

where V_{drop} is the potential difference between the maximum potential of charging and the potential at the end of the *i*R drop (Fig. 2.6). The factor of 2 is included in Equation 10 because charge is being moved in two directions, towards and away from the electrode. The drop in potential that occurs immediately upon switching from charging to discharging is related to the ohmic resistance of the system, described by Ohm's law, shown in Equation 11, where *i* is current. This resistance encompasses all the equivalent series resistance in the system, including the resistance of the solution, wires, and instrument contacts, as well as the contact at the interface of the MnOx film and the current collector.

$$V = iR \tag{11}$$

Finally, cycle life can be evaluated via long-term GCD cycling at a constant current. Herein, cycle life and electrochemical stability from GCD data are determined through monitoring of the percent charge retention over the course of cycling, achieved by integrating the current vs. time plot for the discharge portion of various cycles using EC Lab software.

2.8 X-Ray Photoelectron Spectroscopy

X-Ray photoelectron spectroscopy (XPS) is a surface characterization technique used both to evaluate the degree of hydration in MnOx films[26,61,90] and as an *ex situ* evaluation of degree of carbon oxidation or relative amounts of oxygen-containing functional groups present on carbon surfaces[36,91]. XPS involves characterizing the composition of a material's surface through investigation of the binding energies of core electrons ejected from a sample as the sample is irradiated by an X-ray source[92]. The data recorded by the spectrometer is plotted as intensity or number of counts (times) a photoelectron of a specific energy was ejected versus the binding energy of the photoelectrons[92]. What is actually measured by the instrument is the kinetic energy (E_K) of the ejected photoelectron[92]. This value has some dependence on the energy of the X-ray beam used and thus is incapable of identifying the electron ejected, but conversion of this value into a binding energy (E_B) allows for identification[92]. The x-axis E_B values are then calculated using the following Equation (12)[92]:

$$E_B = h\nu - E_K - W \tag{12}$$

where $h\nu$ represents the energy of the photons, E_K signifies the kinetic energy of the electrons upon ejection, and W is the work function of the material, *i.e.* the energy required to remove an electron from that material and eject it into a vacuum. Analysis of the O_{1s} spectrum of MnOx films allows for determination of degree of hydration[26,61,90] whereas analysis of the C_{1s} spectrum of carbon samples as well as the XPS survey scan can provide information on the amount of oxygen-containing functional groups present on the surface[36,53,91].

Chapter 3 Experimental Methods

3.1 Chemicals and Instrumentation

0.2 M $MnSO_4$ (purity >99.0%, Sigma Aldrich) was used as the electrolyte for electrodeposition of manganese oxide (MnOx) thin films on 304-grade stainless steel (McMaster-Carr). Reduced graphene oxide (rGO) was purchased from Sigma Aldrich. 0.5 M Na_2SO_4 (>99.0% purity, Fisher Scientific) electrolyte was used for all electrochemical experiments performed on MnOx films. 1.0 M H_2SO_4 electrolyte was made from concentrated H_2SO_4 (Caledon, 95-98% by weight, reagent grade) and used for all experiments on rGO. 18 MΩ·cm deionized water was made from either an Arium Mini Plus or Millipore Direct Q-UV3 and was used to make all solutions. Nitrogen used to deaerate the MnOx deposition cell was purchased from Praxair (purity > 99.99%).

3.1.1 Electrochemical Instrumentation

All electrochemical experiments were performed using a Biologic VMP3 Multipotentiostat under EC Lab software control. Ag/AgCl reference electrodes (1.0 M KCl filling solution, ~0.222 V vs. the standard hydrogen electrode (SHE), CH Instruments) were used for all experiments, except the electrodeposition of MnOx, which used a homemade Ag/AgCl reference (saturated NaCl filling solution, ~0.19 V vs. SHE). Potentials in the results section of this thesis are reported vs. a saturated calomel electrode (SCE) for all experiments on MnOx electrodes and vs. SHE for all experiments on rGO since Ag/AgCl reference potentials varied between electrodes and from day to day.

3.2 Preparation of Manganese Oxide Electrodes

While many methods of synthesizing MnOx films are available such as sol-gel[25,93] and hydrothermal syntheses[67,90], electrodeposition provides a hydrous film[94] and eliminates the requirement for addition of a binder to achieve adequate adhesion of the film to the substrate[62]. Furthermore, electrodeposition offers reasonable control over the thickness of the films and can be used with both smooth and rough substrates. In this work, two deposition methods were used. The first involved a single deposition step, where five different electrode types were made by employing different film drying and storage methods. The second involved a double-deposition procedure in which four film conditions were prepared by altering the ratio of heat-treated to hydrous MnOx in the film.

3.2.1 Electrodeposition of Manganese Oxide

Stainless steel was thoroughly cleaned by rinsing with 18 MΩ·cm water, methanol, and again with 18 MΩ·cm water, wiping vigorously with a Kimwipe following each rinse. The stainless steel was then cut into strips approximately 10 cm x 1 cm. A 6 cm^2 (3 x 1 cm, both sides of the stainless steel) electrode surface area was obtained by covering the majority of the stainless steel strip with Parafilm; also, a section of stainless steel at the top of the electrode was left exposed for connection to the potentiostat. Prior to deposition, individual electrodes were again rinsed with methanol and wiped, and then rinsed with 18 MΩ·cm water. All MnOx films were fabricated using a potentiostatic deposition in a 0.2 M $MnSO_4$ deposition electrolyte. The deposition solution was maintained at 55-60 °C, deaerated with N_2, and stirred. Deposition was carried out at 1.0 V vs. SCE. A Ag/AgCl reference and 18 cm^2 geometric surface area Pt gauze counter

electrode completed the circuit. Following deposition, all electrodes were rinsed well with 18 MΩ·cm water.

For single-deposition films, the deposition was carried out for 60 seconds. 'Wet' films were stored in 0.5 M Na_2SO_4 until use. 'Humid' films were allowed to air-dry on the lab bench and 'desiccator' films were dried in a desiccator. 100 °C and 200 °C oven-dried films were dried at their respective temperatures for two hours in an oven. Deposition charges (in C) for single-deposition films were determined by integrating the current vs. time plot from each individual deposition using EC Lab software. Deposition charge values were used to normalize data when necessary for true comparison since accurate masses of the thin films could not be obtained.

The double-deposition procedure consisted of an initial deposition of MnOx and a 200 °C heat-treatment step followed by a second MnOx deposition and wet storage of the films in 0.5 M Na_2SO_4. Instead of limiting the deposition by time, as done with the single-deposition films, the double-deposition method was limited to a total cumulative charge passed (Q_{dep}) for both depositions of 1.6 C; this represented a rough average of the deposition charges obtained with single depositions. This 1.6 C was split between the two depositions, using $Q_{dep}1$:$Q_{dep}2$ ratios of 10:90 (160 mC:1440 mC), 25:75 (400 mC:1200 mC), 50:50 (800 mC:800 mC), and 75:25 (1200 mC:400 mC). The first layer of film was rinsed with 18 MΩ·cm water and then oven-dried at 200 °C for two hours. Then, the second layer of MnOx was deposited on the oven-dried portion, rinsed well again, and stored in 0.5 M Na_2SO_4 until use.

3.3 Preparation of rGO Electrodes

3.3.1 rGO Microcavity Electrodes

Microcavity electrodes were prepared by the scientific glassblower at Dalhousie University (Todd Carter) and previous Ph.D. student Justin Tom by sealing a thin Pt wire (250 μm diameter) in glass. A more detailed description of microcavity electrode fabrication can be found in Dr. Tom's thesis[95]. Briefly, the sealed end of the electrode was polished to a smooth, flat surface exposing the end of the Pt wire. Sonication was subsequently used to remove any polish left on the electrode and Ni wires were placed in the hollow end of the glass tube to provide electrical contact with the Pt wire.

Next, a cavity was created by etching the exposed Pt in aqua region (3:1 ratio concentrated HCl (37%, purity 99.99%, Sigma Aldrich):concentrated HNO_3 (70%, purity 99.999%, Sigma Aldrich)). The electrode was then rinsed well with 18 MΩ·cm water and sonicated before repeating the aqua-regia-etching procedure once more with a newly-prepared aqua regia solution. The resulting microcavities were 250 μm in diameter with a depth of 40-100% of the diameter. These dimensions are within the ideal range for a microcavity electrode to ensure the powder is securely held in the cavity without hindering the electrical connection between the rGO sample and the Pt wire at the cavity base as specified by Cachet-Viviera *et al.*[96]. rGO powder was loaded into freshly-cleaned microcavity electrodes by pressing the electrodes firmly into a pile of as-received rGO on a clean glass slide. Excess rGO was removed from the electrode using a Kimwipe.

3.3.1.1 Cleaning the Microcavity

Prior to each new experiment, rGO remaining in the cavity from the previous experiment was removed by sonicating the electrode in distilled water for three to ten

minutes. The electrode was then rinsed well with 18 MΩ·cm water and a three-step CV cleaning procedure was employed. First, the bare Pt electrode was cycled at 1000 mV s^{-1} for 100 cycles in a potential window of approximately -0.10 to 1.45 V vs. SHE in 1 M H_2SO_4. At negative potentials, hydrogen evolution occurs on the Pt surface and the evolved gas can remove contaminants from the surface. Then, the Pt electrode was cycled in a truncated 0.0 to 1.45 V window for 100 cycles again at 1000 mV s^{-1}. This step allows the Pt oxide film to reform several times to ensure a clean surface without interference from H_2 evolution. A final three to five cycles to evaluate the cleanliness of the Pt were run at 100 mV s^{-1}. Cleanliness was determined by identifying three unique hydrogen underpotential deposition (H_{upd}) peaks (see Fig. 3.1), a flat double-layer capacitance region, and a Pt oxide oxidation plateau and reduction peak. If these features were not visible or were corrupted with contaminant peaks, the cleaning procedure was repeated until a clean Pt CV was recorded. If a clean Pt CV was still not evidenced after repetition of the above described procedure, the microcavity electrode was soaked in concentrated H_2SO_4 for at least 20 minutes before repeating the above described cleaning procedure.

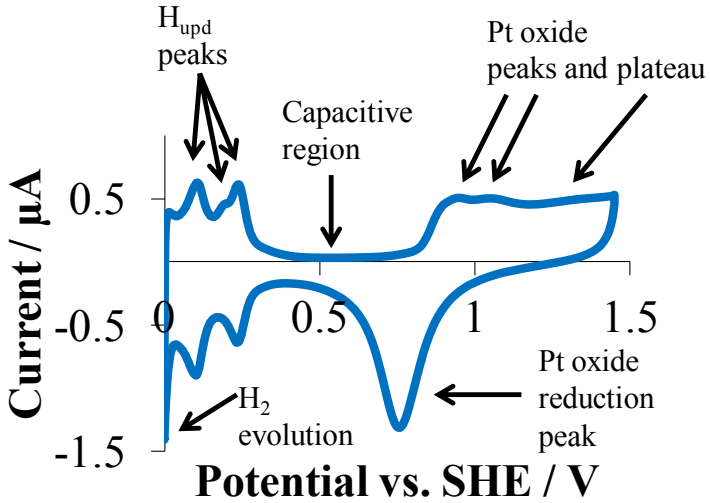

Figure 3.1. CV (100 mV s^{-1}) of a clean Pt microcavity electrode displaying the H_{upd} peaks and other features that indicate the Pt is clean.

3.3.2 rGO Glassy Carbon Electrodes

rGO suspensions were made by sonicating ~ 1 mg of rGO in 1.0 mL of ethanol three times in 5 minute intervals (Branson 1510 Sonicator). Occasionally, rGO would come out of suspension, but shaking the suspension well before drop-coating was sufficient to resuspend the material. 10 µL of rGO-ethanol (rGO-EtOH) suspension was drop-coated onto 3 mm diameter glassy carbon (GC) electrodes (BASi-MF2012, mirror-like finish) and allowed to dry. Typically, a GC coverage of 65-90% was achieved.

Prior to each use, the GC was cleaned by wiping with a Kimwipe and rinsed well with 18 MΩ·cm water. The GC was then polished on a nylon polishing pad with 1 µm diamond polish (BASi PK-4 MF-2060 Polishing Kit). Following polishing, three CV cycles were performed on the bare GC electrodes in 1.0 M H_2SO_4 to confirm the electrode surfaces were clean. If a clean GC CV was observed (low currents, as shown in Figure 3.2), the electrodes were rinsed well with 18 MΩ·cm water and allowed to dry before addition of the rGO-EtOH suspension.

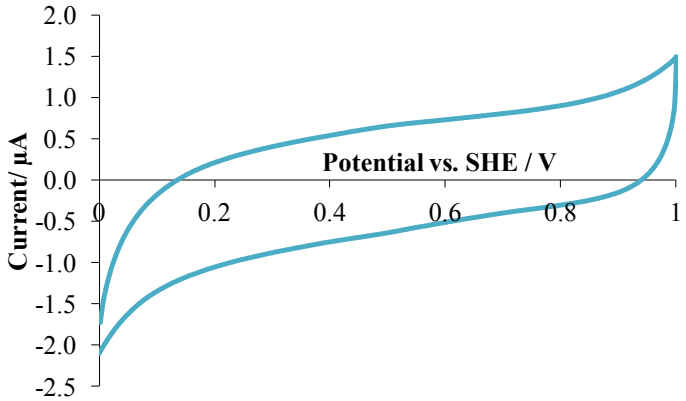

Figure 3.2. CV of a clean, bare GC electrode in 1 M H_2SO_4 at 100 mV s^{-1}.

3.4 Electrochemical Experiments on Manganese Oxide Electrodes

All CV experiments on MnOx electrodes were performed with a sweep rate of

10 mV s^{-1}. A potential window of either 0.4-0.8 V or 0.0-1.0 V vs. SCE was used. To determine capacitance, energy, coulombic efficiency (CE) and energy efficiency (EE) of all electrode types, 30 cycles in the truncated (0.4-0.8 V) window was used. To further test films showing optimal performance and evaluate cycle life, 2000 cycles in the extended (0.0-1.0 V) window were performed.

Galvanostatic charge/discharge (GCD) tests were performed by running three charge/discharge cycles at various applied currents between 0.1 mA and 30 mA. All film conditions were evaluated by GCD in a 0.4-0.8 V window. Tests were conducted on all film conditions in this potential window with currents applied in the following order: 1, 5, 2, 10, 0.5, 0.1, and 0.05 mA. 10:90 and 200 °C oven-dried films were further evaluated with a 0.0-1.0 V window by applying currents in one of the following orders: 1, 5, 2, 10, 7.5, 3, 0.75, 0.5, 0.3, 0.1 mA or 1, 5, 2, 10, 11, 13, 15, 17.5, 20, 25, 30 mA. The data collected during the two tests in the expanded potential window were combined to construct Ragone plots.

Self-discharge (SD) experiments were performed on wet, 200 °C oven-dried, and 10:90 films by charging the electrode at 10 mV s^{-1} to 1.0 V, followed by opening the circuit and monitoring the potential with time for 20 hours. Films were either cycled to steady state in the 0.0-1.0 V window (10 mV s^{-1}) prior to starting the SD experiment (200 °C heat-treated and 10:90 films) or charged from their open-circuit potential to 1.0 V (wet films).

3.5 Electrochemical Experiments on rGO Electrodes

3.5.1 Oxidation of rGO via Cyclic Voltammetry

Many carbons can be oxidized through application of positive potentials in acid[36,38,78–80]. Thus, rGO electrodes were oxidized by cycling in 1.0 M H_2SO_4 for 5500 cycles between 0.0 to 1.0 V vs. SHE at a sweep rate of 100 mV s^{-1}. After 5500 cycles, peak growth ceases and the electrodes reach steady-state after which no further changes in the CV are seen.

3.5.2 Float Current Experiments on rGO

Float current experiments were conducted on oxidized and unoxidized rGO powders in microcavity electrodes in 1.0 M H_2SO_4 electrolyte. Electrodes were charged from 0.5 V at 100 mV s^{-1} to a final potential of 0.55, 0.6, 0.7, 0.8, 0.9, or 1.0 V. The potential was held for 30 minutes while the float current was recorded as a function of time. The potential of the unoxidized rGO (used as-received) was stepped down to 0.5 V to initiate charging. This rapid initial discharge serves to stimulate CR effects in the material, if they exist[45]. Following charging, unoxidized carbons were subjected to 100 CV cycles with the same sweep rate and window used to generate oxidized rGO.

Two different methods were used to bring oxidized carbons to 0.5 V following the 5500 CV cycles (Fig. 3.3). A reverse scan from 0.0 V to 0.5 V vs. SHE at 100 mV s^{-1} was implemented following the final (5500^{th}) CV cycle for oxidized positive sweep (Ox-PS) rGO. Oxidized negative sweep (Ox-NS) rGO initially underwent identical CV cycling as Ox-PS rGO for 5500 cycles. However, instead of ending the CV with a reverse scan to 0.5 V, Ox-NS carbons were cycled for another three quarters of a cycle, sweeping back up to 1.0 V and then down to 0.5 V. Figure 3.3 displays the final CV cycle

followed by the potential profile applied to terminate CV cycling at 0.5 V for the two electrode conditions. Immediately following cycling, Ox-PS and Ox-NS carbons underwent the same charging and holding procedure as unoxidized rGO.

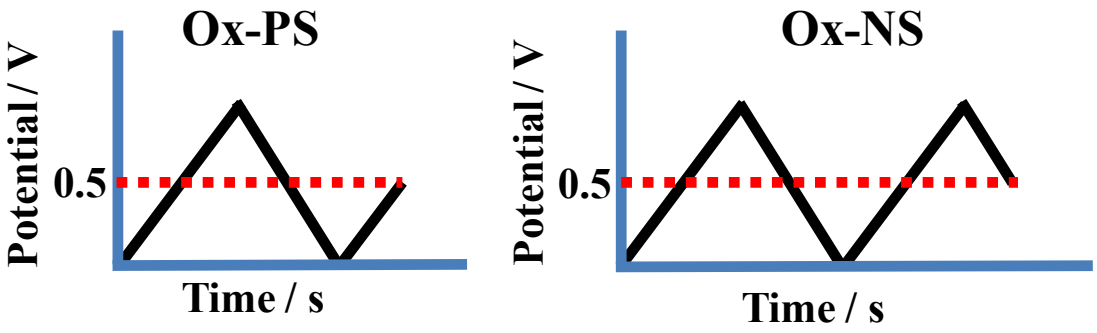

Figure 3.3. Potential profiles from the final CV cycle to the end of the oxidation process for Ox-PS electrodes and Ox-NS electrodes, highlighting the difference in how a final potential of 0.5 V was reached.

To account for variation in rGO loading in the microcavity, float currents are reported normalized to the anodic current at 0.3 V ($I_{a,\,0.3\ V}$) in either the final CV cycle prior to the potentiostatic hold (oxidized rGO) or the final cycle post-holding (unoxidized rGO). The current at this potential was chosen as the CV remained relatively constant at this potential during cycling. If a potential where current varies substantially with cycling was chosen, it would result in inconsistent normalization between oxidized and unoxidized rGO.

3.5.3 Modeling Charge Redistribution in Pores by Use of a Hardware Circuit

A transmission line hardware circuit provided a model pore to simulate how rGO electrodes would respond to charging and potentiostatic holds if redistribution of charge was the sole phenomenon responsible for any currents produced. The transmission line circuit used in this work is based on de Levie's model[50] and is comprised of eight sections in total, with each section containing a resistor and capacitor in series.

Capacitors serve as a model of the electrical double layer formed at the electrode-electrolyte interface down the pore while the resistors simulate the resistance ions encounter as they move to greater pore depths[41]. An in-depth description of the circuit is described elsewhere[40,41,46]. Briefly, each individual capacitor in the transmission line consists of ten 10 µF/6.3 V multilayer ceramic chip capacitors in parallel. Excluding the first resistor, which was set to 0 Ω and represented the opening of the pore, all resistors were set to 1 kΩ. A diagram of the transmission line is provided in Figure 3.4. In this diagram, WE, CE, and RE refer to working electrode, counter electrode, and reference electrode, respectively.

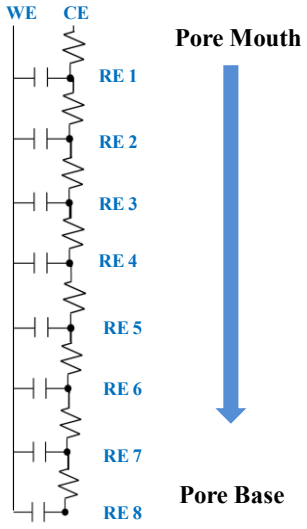

Figure 3.4. Diagram of the transmission line used to model CR within a pore.

To simulate unoxidized rGO electrode experiments, the master channel (capacitor 1, representing the pore mouth) of the hardware circuit was held at 0.8 V for 1 minute. This allowed sufficient time for the charge on all capacitors to reach 0.8 V (a uniform charge down the entire length of the model pore). The master channel was then stepped to 0.5 V and charged at 100 mV s^{-1} to the desired voltage, the identical procedure used to charge rGO electrodes. The master channel was then held at that voltage for 30 seconds

while the float current and the voltage of the remaining capacitors in the circuit were monitored. Secondary channels (corresponding to capacitors 2-8) were left in open-circuit configuration with no voltage applied; changes in secondary channel voltages are the result of CR within the circuit. This model is also used to support theories regarding MnOx GCD results using data collected by Felicia Licht (Andreas Lab).

3.5.4 Open-Circuit Self-Discharge Evaluation of rGO on Glassy Carbon

SD experiments were conducted on rGO electrodes (GC substrate) in 1.0 M H_2SO_4 with and without implementing potential holds between each charge/SD cycle, referred to as CR-reset SD and SD, respectively. The holds served to reset the state of charge, and therefore CR, within the carbon, described further in Chapter 6 and 7. Four consecutive charge/SD cycles were run in both experiments, each consisting of charging to 1.0 V at 100 mV s^{-1} and then opening the circuit to monitor the potential decay with time. The rGO was oxidized using the positive sweep method implemented with Ox-PS rGO microcavity electrodes. For the CR-reset SD experiments, the potential reached with the reverse scan was modified to match the hold potential. Unoxidized electrodes were cycled once from 0.0 to 1.0 V and then reverse scanned to 0.5 V prior to starting the first cycle in the SD experiment, or simply stepped to the hold potential and charged to 1.0 V following the hold in the CR-reset SD experiments. For cycles 2 to 4 in the SD experiment, electrodes were charged from OCP (reached at the end of the previous SD).

For the CR-reset SD experiments, electrodes were stepped down to and held at 0.6 V for either 20 hours or 40 hours prior to starting each charge/SD cycle. This potential was chosen as it is too low to oxidize rGO, and therefore eliminates degree of oxidation as a variable between unoxidized rGO with and without reset CR. For clarity, a

potential profile of the CR-reset SD experiment is provided in Figure 3.5. The time required for cycling is not drawn to scale. A green star locates where the experiment would start for unoxidized CR-reset rGO and numbers in parentheses indicate the number of times the adjacent step (in curly brackets) was repeated. For experiments without the CR-reset steps the potential decay during each charge/SD cycle was monitored for 20 hours. For experiments with the CR-reset step, the potential decay was monitored for 10 hours.

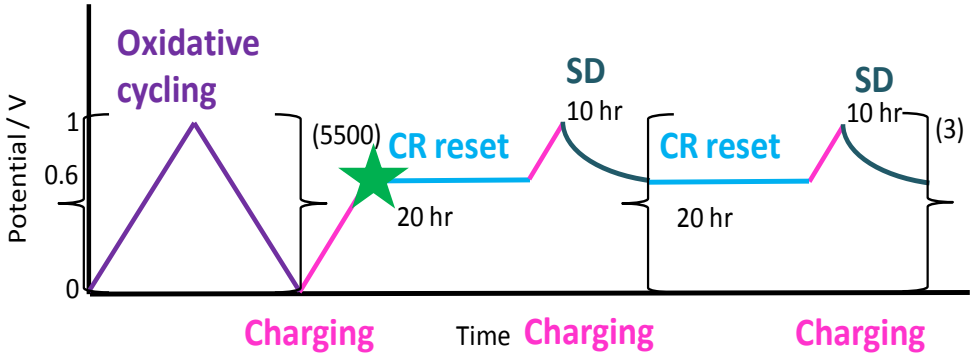

Figure 3.5. Potential profile for the CR-reset SD experiment designed to control changes in CR through applying potential holds prior to each charge/SD for oxidized rGO. Numbers in parentheses indicate the number of times that section of the experiment was repeated. The green star indicates where the experiment started for unoxidized rGO.

3.6 Physical Characterization of Materials

3.6.1 Thermogravimetric Analysis

Thermogravimetric analysis (TGA) of MnOx powders was conducted using a SDT-Q600 simulatenous thermogravimetric analyzer and differential scanning calorimeter (TA Instruments) with the help of Dr. Robbie Sanderson (Dalhousie University, Department of Physics and Atmospheric Science). Films from 10-15 wet electrodes (Section 3.2.1) were scraped from their substrates to acquire enough sample for each TGA run. Wet electrodes were rinsed thoroughly with 18 MΩ·cm water and

gently dabbed with a Kimwipe prior to scraping. The dabbing step was to ensure rinse water was removed and would not alter the mass of the sample. First, samples were subjected to a five minute isothermal hold at 30 ºC to permit mass equilibration. Samples were then heated to 500 ºC under a 100 mL min^{-1} flow of compressed air with a 10 ºC min^{-1} ramp rate to monitor the water lost from each sample.

3.6.2 Scanning Electron Microscopy

Scanning electron microscope (SEM) images of MnOx films were obtained either with the assistance of Dr. Ping Li (Dalhousie University, Department of Biology) using a LEO 1455VP SEM with a 20 kV accelerating voltage at various magnifications or with the assistance of Dr. Patricia Scallion (Dalhousie University, Department of Mechanical Engineering) using a Hitachi S-4700 cold field emission SEM with a 3 kV accelerating voltage at 50000x magnification. Samples were cut from MnOx-coated electrodes and mounted onto the SEM sample stage on stainless steel buttons. Conductive carbon tape ensured electrical connection to the buttons.

3.6.3 X-Ray Photoelectron Spectroscopy

X-Ray photoelectron spectroscopy (XPS) spectra of rGO powders and MnOx films were collected using a Thermo VG Scientific Multilab ESCA 2000 spectrometer with a CLAM4 MCD electron energy analyzer by Andrew George (Technician, Dalhousie University, Department of Physics and Atmospheric Science). The pass energy was 30 eV and Al Kα rays (1486.6 eV, spot size 0.6 mm in diameter) and Mg Kα ray (1253.6 eV, spot size 0.6 mm in diameter) provided the X-ray source for the MnOx and rGO samples, respectively. XPS experiments were performed at room temperature at a

pressure ranging between $9.5x10^{-10}$ to $7.0x10^{-9}$ torr. XPS was conducted on films of MnOx on stainless steel cut from an electrode prior to electrochemical experiments.

CasaXPS software was used to fit and analyze all spectra using a Shirley background and Gaussian-Lorentzian functions. Three peaks were used to fit the MnOx O_{1s} XPS spectra based on the literature range for the oxide (Mn-O-Mn, 529.3-530.3 eV), hydroxide (Mn-OH, 530.5-531.5 eV), and water (H-O-H, 531.8-532.8)[61] peak. To evaluate the degree of hydration of the films the area under the water peak relative to the total peak area was evaluated for each sample.

Three rGO samples were evaluated by XPS to investigate how the rGO is impacted by the sonication step(s) employed in creating rGO suspensions. The as-received rGO sample was examined without any treatment. The two sonicated samples were each prepared by creating a suspension of approximately 10 mg of rGO in 10 mL of 100% EtOH. The samples were then sonicated in five minute intervals either three or seven times. The EtOH was subsequently evaporated and the dry powders were used for XPS. rGO C_{1s} spectra were fitted using five peaks from the literature. Literature values indicate the graphitic (C=C) peak is located at 284.3 eV[97–100], the C-O peak presents at 285.5-285.6 eV[97,99–103], and the C=O peak ranges between 286.8 to 287.1 eV[98,99,102,104–106]. The COOR peak presents at 288.6 to 288.9 eV[97–99,102,104–106] and the π-π^* shakeup peaks lies between 290.3 to 290.4 eV[97,106–108]. For the fitted rGO XPS peaks, error estimates (one standard deviation) for the percent surface concentration were calculated in the CasaXPS program using Monte Carlo simulations.

3.6.4 Inductively-Coupled Plasma Optical Emission Spectroscopy

To investigate MnOx film dissolution during experiments, inductively-coupled plasma optical emission spectroscopy (ICP-OES) was performed on electrolyte samples following their use in experiments with MnOx electrodes. After cycling MnOx films at 10 mV s^{-1} in a potential range of 0.0-1.0 V for 2000 cycles, electrolyte samples were taken from the cells and acidified to 2% HNO_3 by volume (70%, Sigma Aldrich). The acidified samples were then run on a PerkinElmer Optima 8000 with the help of Dr. Alicia Oickle (Dalhousie University, Department of Applied Oral Health Sciences).

Chapter 4 Effects of Heat Treatment on the Electrochemical Performance of Manganese Oxide Thin-Film Electrodes

4.1 Introduction

This chapter describes the impact of degree of film hydration on the electrochemical performance of MnOx in various experiments. Currently, some debate exists in the literature regarding the effect of heat treatment; both a decline in capacitance with increasing heat-treatment temperature[26–30] and an increase in capacitance if an appropriate temperature is applied[32,67–69,109], have been reported. In general, water removal from MnOx films is expected to result in a diminished capacitance as a consequence of decreased pseudocapacitive charge storage; this is because cation movement within these films is enhanced by hydrous regions in the film[2,28,34], and cation diffusion is a key component in the charge storage mechanism of MnOx[64]. In contrast, electronic conductivity is impeded by water content[26,33], and heat treatment of MnOx can result in decreased resistance[30–32], critical for the high-power applications in which ECs are typically used. Heat treatment has also offered enhanced cycling stability[26,31].

Interestingly, 70 °C[32], 200 °C[68,69], 300 °C[109], and 500 °C[67] have all been found to be optimal drying temperatures for MnOx electrodes. For the most part, the literature focuses on capacitance, cycle life, and resistance of films dried at various temperatures, leaving other properties such as efficiency, film usage, and power, which critically impact device performance, widely neglected. Thus, the goal of the work presented in this chapter is to provide analysis of how hydration alters the electrochemical response of MnOx through investigation of a wide range of electrode properties. This work fills the gap in the literature where such an in-depth study of electrochemical performance across

a variety of tests to evaluate hydration effects in one unique system has yet to be conducted.

Appropriate drying temperatures were chosen based on thermogravimetric analysis (TGA) results and the degree of hydration of the MnOx films was investigated using X-ray photoelectron spectroscopy (XPS). Cyclic voltammetry (CV) data and galvanostatic charge/discharge (GCD) experiments provided measures of capacitance, coulombic efficiency (CE), film usage, energy, energy efficiency (EE), power, resistance, and cycle life. Scanning electron microscopy (SEM) provided images of film macrostructure and evidence of cracking which likely impacts physical stability. Visual observation of physical stability, including film chipping, delamination, and dissolution are also reported herein. A transmission-line-hardware circuit is used to compare the system under study to a system without Faradaic reactions, using data collected by Andreas Lab honours student Felicia Licht. The findings discussed in this chapter inspired the design and development of double-deposition MnOx films, discussed in Chapter 5, in attempts to combine the benefits of hydrous and anhydrous MnOx.

4.2 Tracking the Degree of Hydration of Manganese Oxide Films

TGA was used to track water loss from the MnOx as a function of drying temperature. Wet-stored films were rinsed well with 18 MΩ·cm water to remove residual Na_2SO_4 from the storing solution, then scraped from their substrates to provide a powder for TGA. Powder from wet electrodes was chosen as these films best represent the as-deposited films (*i.e.* no drying to remove water). In Figure 4.1, the weight loss below ~220 °C can be attributed mainly to physically-adsorbed water loss[28,90] and some loss of oxygen[110]; it is clear that there is significant water loss at temperatures near

100 °C. The continued, more gradual weight loss above 220 °C is likely the result of loss of residual crystalline water[90] and continued loss of residual O_2[111]. Since the steepest weight loss occurs before 100 °C, and the decline becomes more gradual after 200 °C, these two temperatures were chosen to evaluate as drying temperatures. The TGA results also confirm that drying at 200 °C removes more structural water than drying at 100 °C.

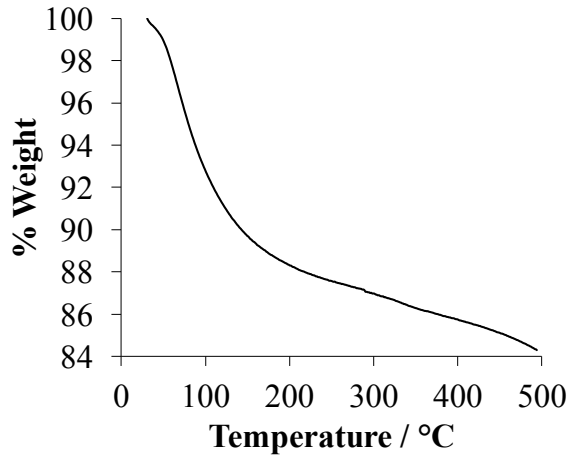

Figure 4.1. TGA data for MnOx powder scraped from wet electrodes.

The relative degrees of hydration of MnOx films prepared with various drying and storage conditions were determined through analysis of deconvoluted O_{1s} XPS spectra (Fig. 4.2). Peaks located at 531.8-532.8 eV, 529.3-530.3 eV, and 530.5-531.5 eV indicate oxygen in water (H-O-H), oxide (Mn-O-Mn), and hydroxide (Mn-OH) environments, respectively[61]. Wet electrodes were not tested by XPS because the XPS vacuum would remove the excess hydration achieved through continuous soaking of the wet electrodes and the data would not accurately reflect the degree of hydration of the wet films. Relative percentages of the fitted peaks are presented in Table 1. As expected, a lower degree of hydration is found in films treated with more extensive drying procedures.

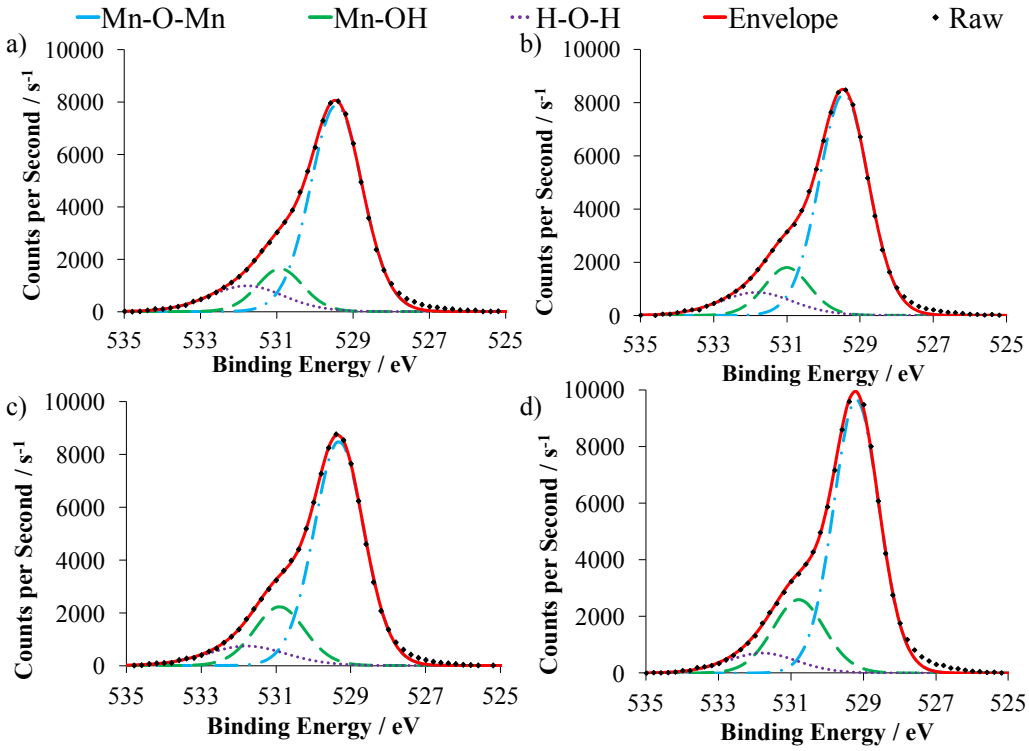

Figure 4.2. Background-subtracted fitted XPS spectra for MnOx films stored under a) humid conditions, b) in a desiccator, or oven-dried at c) 100 °C and d) 200 °C.

Table 1. O_{1s} XPS peak percentages for MnOx films determined through fitting spectra in Fig. 4.2.

Drying Condition	Mn-O-Mn %	Mn-O-H %	H-O-H %
Humid	73.5	13.4	13.1
Desiccator	74.1	14.7	11.2
100 °C Oven-Dry	71.2	19.0	9.8
200 °C Oven-Dry	70.6	21.4	8.0

SEM micrographs of MnOx films are presented in Figure 4.3. At 5000x (Fig. 4.3a-d) magnification, a non-uniform surface with varying thickness is evident in all films. Cracks were observed in all film types, with the extent of cracking generally increasing with decreased hydration. The inset in Figure 4.3a shows a crack observed in the wet film at 2000x magnification (circled in red). Micrographs captured at 50000x magnification show no significant changes to the 200 °C oven-dried films after 2000 CV

cycles between 0.0-1.0 V at 10 mV s^{-1} (Fig. 4.3e and f). In contrast, wet-stored films show a slight growth in platelet size following 1000 cycles in a 0.4-0.8 V window (Fig. 4.3g and h). The truncated window was used for the wet-stored films due to stability issues in the extended window (Chapter 5). The change in platelet size will be discussed further in Sections 4.4 and 4.5.

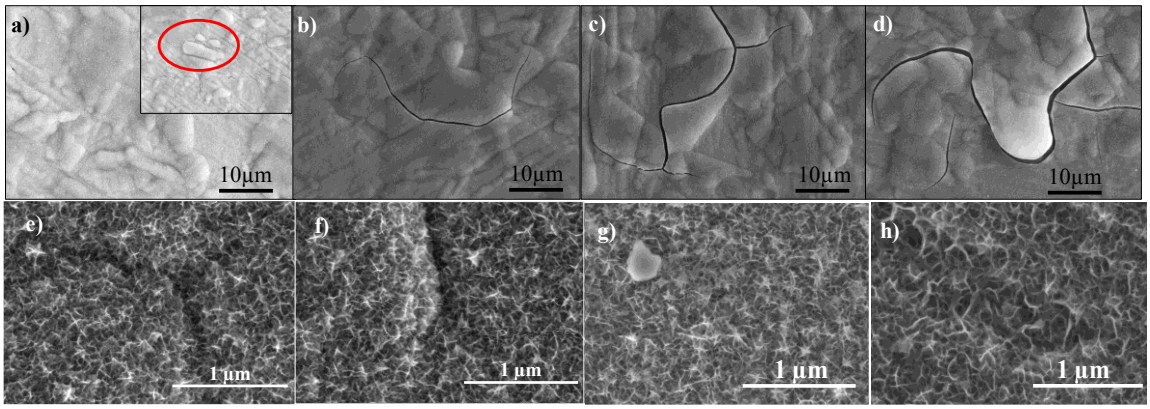

Figure 4.3. SEM images at 5000x magnification of a) wet, b) humid, c) 100 °C oven-dried, and d) 200 °C oven-dried films. The inset in panel a) shows a crack observed at 2000x magnification with a wet film. Panels e) and f) show a 200 °C oven-dried film at 50000x magnification before and after CV cycling, respectively. Panels g) and h) show a wet film at 50000x magnification before and after CV cycling, respectively.

4.3 Effect of Hydration on Electrochemical Figures of Merit during Cyclic Voltammetry

Representative CVs of MnOx films prepared with various storage or drying procedures are presented in Figure 4.4. To address differences in the amount of film deposited using the electrodeposition, currents were normalized to deposition charge (Q_{dep}). Similar to literature results, removal of water content by high-temperature drying results in smaller CVs (Fig. 4.4) and diminished capacitances[27–30,66] (Table 2). Nonetheless, all electrodes display rectangular CVs indicative of pseudocapacitive films. Capacitance loss as a consequence of heat treatment is often explained by the loss of structural water in the electrodes limiting cation diffusion, thereby limiting the portion of

the film that can participate in pseudocapacitance[28–30]. Slow-rate cycling of oven-dried films - 100 cycles at 1 mV s^{-1} between 0.4-0.8 V, requiring ca. 22 hours (not shown) - evidenced no current increase over time, indicating rehydration of heat-treated films due to electrolyte exposure during electrochemistry is not a concern.

MnOx films that were not exposed to high temperatures (wet, humid, desiccator) show a slower current recovery upon switching the potential sweep direction (indicated by the arrows in Fig. 4.4), characteristic of higher resistances. In contrast, heat-treated films demonstrate very vertical current switches at the potential extremes. Similar results have already been observed[30] and indicate improved MnOx electronic conductivity as a result of decreased water content in the film[26,30,31,33]. Resistances calculated from the *i*R drop in GCD experiments (Section 4.4) confirm these resistance trends.

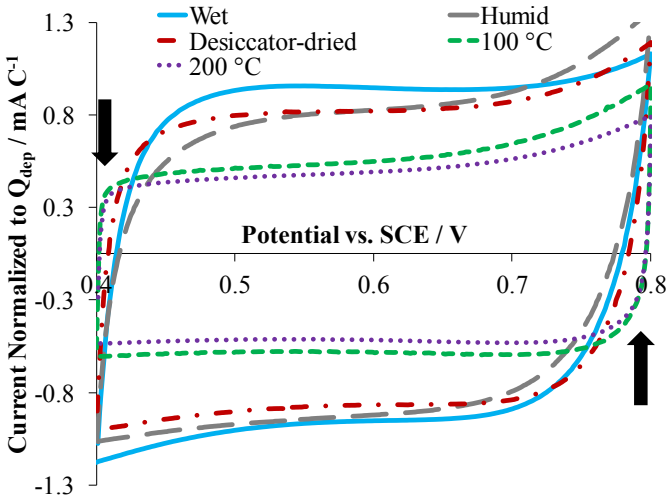

Figure 4.4. Representative CVs of MnOx films dried/stored under different conditions. CVs were recorded in 0.5 M Na_2SO_4 with a 10 mV s^{-1} sweep rate.

Table 2. Average capacitances calculated from CV data for MnOx films with varying drying/storage conditions.

Drying Condition	Capacitance mF C^{-1}
Wet	89 ± 4
Humid	81 ± 6
Desiccator	71 ± 7
100 °C	50 ± 2
200 °C	44 ± 3

An irreversible oxidation wave initiating near 0.7 V that decreases with cycling is seen in CVs of all film types (Fig. 4.4). Currently, the reaction responsible for the oxidation remains unclear, but film dissolution, oxidation of residual Mn^{2+} trapped in pores from electrodeposition, irreversible oxidation of the film, or CR effects are all possibilities. MnOx film dissolution is likely contributing somewhat to the oxidation wave since film dissolution is a common outcome of long-term cycling in the literature[9,20–25]. However, potential windows extending past the 0.4-0.8 V employed in this work on either the positive extreme, negative extreme, or both were used in literature reports[9,20–25].

Electrolyte samples taken from cells following 2000 CV cycles between 0-1.0 V vs. SCE at 10 mV s^{-1} on 200 °C oven-dried electrodes were analyzed via inductively-coupled plasma optical emission spectroscopy (ICP-OES). The increased potential window and number of cycles were employed to maximize dissolution. The concentration of Mn ions in electrolyte following electrochemistry was determined to be ~0.2 to 1.5 ppm. Although electrolyte samples from tests performed in the 0.4-0.8 V window were not examined by ICP-OES, and dissolution in this truncated window has not been reported previously, visual evidence of film dissolution confirms dissolution is occurring in the potential window under investigation. Mn deposition on the Pt counter

electrodes and electrolyte discolouration, indicative of film dissolution, is shown in Figure 4.5.

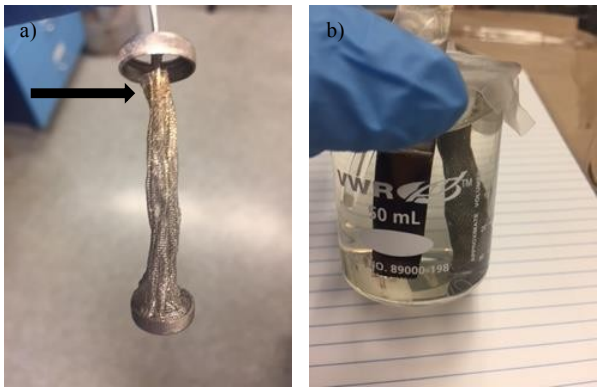

Figure 4.5. Visual evidence of MnOx dissolution (200 ºC oven-dried film) during multicurrent GCD experiments observed as a) brown Mn deposit on the Pt counter electrode and b) slightly discoloured electrolyte.

In the initial cycles, substantially larger oxidation waves are observed for oven-dried MnOx compared to its hydrous analogues (Fig. 4.6a-e), suggesting whatever the reaction (dissolution, irreversible oxidation, etc.) or process is, it is enhanced by film changes during heat treatment. The large irreversible oxidation is responsible for the considerably lower CEs for the heat-treated films (Fig. 4.6f), particularly in early cycles. Peak oxidation currents at 0.8 V in the CV (I_p) were normalized to the capacitive current at 0.58 V ($I_{0.58\ V}$) to compare the relative amount of oxidation to the amount of active film (Table 3). The larger normalized I_p values for heat-treated films confirm the larger oxidation wave evidenced by these electrodes is not simply an optical illusion. These findings indicate that high-temperature drying generates films that are more susceptible to film changes during use in an EC.

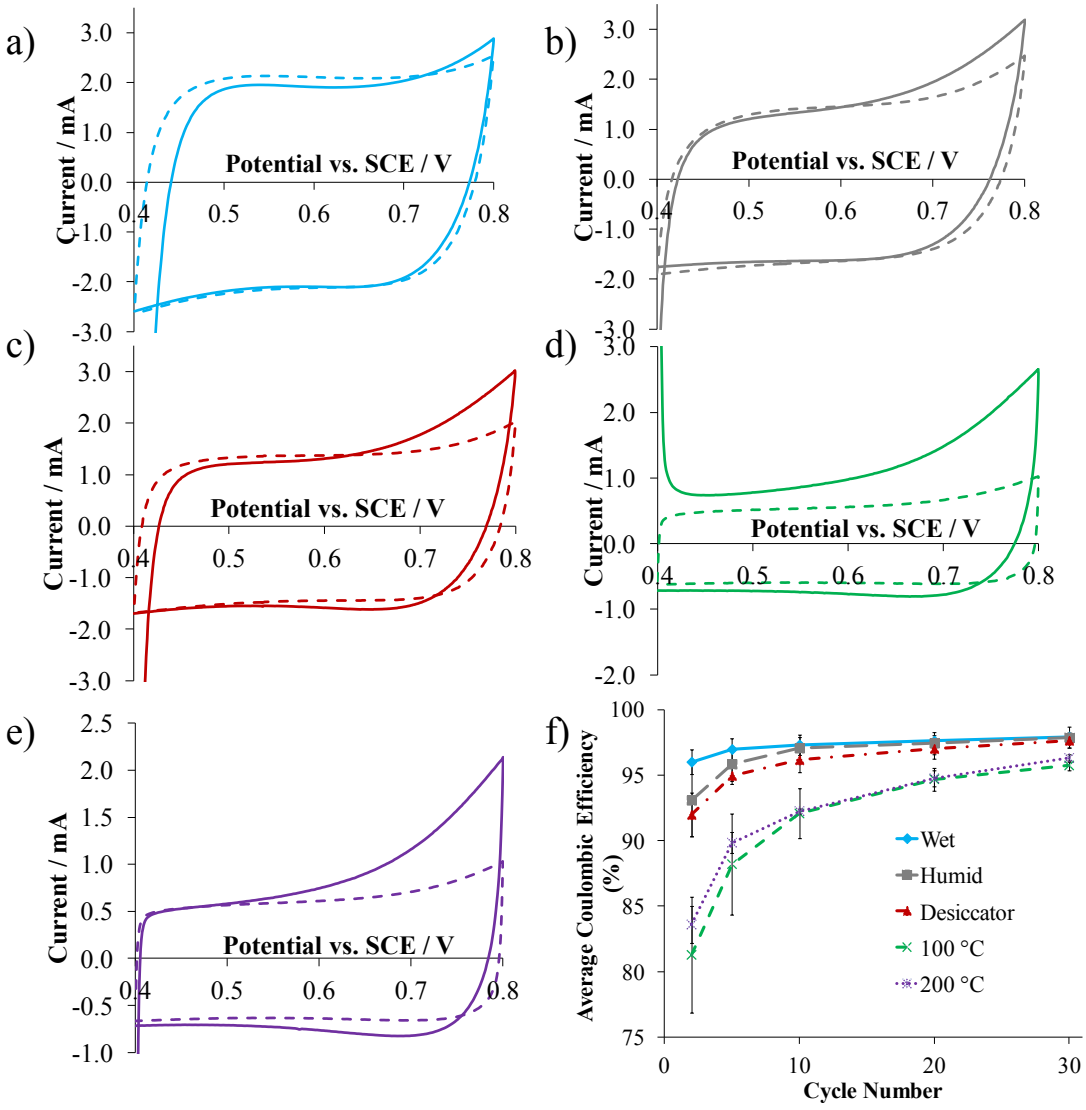

Figure 4.6. Cycles 1 (solid line) and 30 (dashed line) of a representative a) wet, b) humid, c) desiccator-dried, d)100 °C, and e) 200 °C oven-dried film showing a decreasing oxidation wave and f) average CEs as a function of cycle number for all film types.

Table 3. Average ratio of I_p to $I_{0.58\ V}$ for electrodes made with different drying/storage methods.

Drying Condition	I_p to $I_{0.58\ V}$ ratio
Wet	1.4 ± 0.1
Humid	1.8 ± 0.4
Desiccator	2.0 ± 0.4
100 °C	3.0 ± 0.2
200 °C	2.97 ± 0.04

Nevertheless, all films show improvements in CE with increasing cycle number as the oxidation wave disappears with cycling (Fig. 4.6f). This is important in terms of commercial applications as it is desirable to have electrodes at steady state before they are used in a device to ensure that device performance is consistent with use. The CEs obtained during the final CV cycle are more indicative of the CE of the device since at this point the MnOx CEs have stabilized. A more in-depth discussion of CE and the causes of the oxidation will be undertaken with GCD data in Section 4.4.

When evaluating the performance of an energy storage device, both the energy that can be stored on the device as well as the ability of the device to deliver that energy need to be considered. Average anodic (E_a) and cathodic (E_c) energies of the various films determined from the final (30^{th}) cycle of CV data are listed in Table 4. Average energy efficiencies (EE) are also listed in Table 4. While more hydrous (wet, humid, desiccator) MnOx shows similar energies, a significant decrease in energy is observed following heat treatment. As a consequence, devices relying on oven-dried MnOx would require recharge more frequently than devices using wet, humid, or desiccator-dried MnOx. On the other hand, heat treatment generates films that deliver the energy more efficiently, as indicated by the higher EE of oven-dried films compared to their more

hydrous analogues. These findings imply heat treatment makes energy stored in films more accessible, but at the cost of a reduction in the amount of energy that can be stored.

The increased EE of oven-dried films is likely due to the decreased film resistance achieved through heat treatment[30–32]. This decrease in resistance means films can be more responsive to changes in potential sweep direction, resulting in currents that immediately change sign when the sweep direction is flipped. This provides a more reversible CV, and therefore more similar E_a and E_c values. The slightly poorer energy efficiencies from the more hydrous MnOx films are likely the result of the resistance associated with changing the potential sweep direction, seen as a non-vertical current decay (Fig. 4.4), causing the CVs to be less symmetric. Interestingly, films dried at room temperature (desiccator-dried and humid) show much greater variation in EE, suggesting some MnOx films dried in this fashion can provide an efficient device, but others result in a device with a relatively low EE compared to their heat-treated or wet-stored counterparts. Manufacturers and companies that produce and sell ECs rely on their devices being consistent; the fact humid and desiccator-dried films can only sometimes generate ECs with high EEs is of no benefit if there is no way to distinguish which of these films will result in efficient devices and which ones will not.

These data highlight a key conflict in choosing a drying/storage protocol for MnOx films: room temperature stored/dried MnOx (wet, humid, desiccator-dried) provides higher energies and capacitances, but employing high drying temperatures (100 and 200 °C) provides films that output a greater portion of the energy stored on them when the device is in use. If more energy could be released from an oven-dried film than a wet film owing to the higher EEs of oven-dried films, it would be preferable to use the

oven-dried film. The extra energy stored on the wet film would be of no benefit if it were unavailable to power a device. In the case of this system, however, the enhanced EEs of the heat-treated films is not enough to compensate for their limited energy storage, and the hydrous MnOx still releases more energy than its oven-dried analogues, even though wet films release a smaller fraction of their stored energy. Thus, the hydrated films show more favourable performance in terms of the amount of energy they can output even with their reduced EEs.

Table 4. Average anodic and cathodic energies derived from CV data for MnOx films treated with different storage/drying conditions.

Drying Condition	E_a mJ C^{-1}	E_c mJ C^{-1}	EE (%)
Wet	21.0 ± 0.9	18 ± 1	88 ± 2
Humid	20 ± 2	18 ± 2	80 ± 7
Desiccator	18 ± 2	16 ± 2	76 ± 6
100 °C	14 ± 1	12.4 ± 0.8	90.0 ± 0.7
200 °C	12 ± 1	10.9 ± 0.9	91.1 ± 0.9

4.4 The Effect of Film Hydration on Electrochemical Performance During Galvanostatic Charge/Discharge Tests

Typical, triangular potential vs. time plots are observed at high charging currents for all films (Fig. 4.7a). As expected based on CV data, larger charges, evidenced by longer charging and discharging times, are recorded for the more hydrous films. This is consistent with the enhanced ionic mobility of the hydrous films[26,33] and the larger fraction of the hydrous films that can participate in pseudocapacitance. At low currents the charging curves evidence plateaus at high potentials (Fig. 4.7b). This curvature can be indicative of a reaction happening on the electrode or charges redistributing within the electrode, since the constant current applied is not going into raising the electrode's potential at a constant rate. Instead, the current is going into some secondary process.

Likely, the curvature is a result of the same process(es) responsible for the large oxidation wave in the CV data.

One possible Faradaic reaction is dissolution, which is known to occur with cycling[9,20–25], and has been identified in this system through visual evidence of Mn deposits on the counter electrode and electrolyte discolouration (Fig. 4.5), as well as via ICP-OES. Due to the increased time the films spend at the potential extremes where the dissolution is most likely to occur with low current GCD, these currents are expected to induce the most dissolution. For this reason, low currents were performed at the end of the experiment to allow data at high currents to be collected before dissolution complicated the system under study.

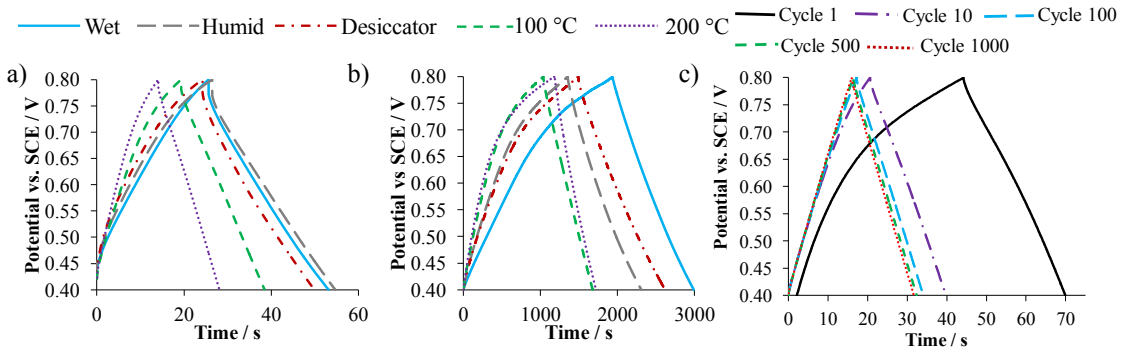

Figure 4.7. Representative GCD curves for each condition at a) 2 mA and b) 0.05 mA. Panel c) displays GCD curves of various cycles for a representative 200 °C oven-dried electrode at 1 mA.

The charging/discharging process requires less time with repetitive cycling (Fig. 4.7c). This could be explained by film dissolution only if the film dissolved such that the active layer of the film (film near the surface) became less rough; a smoother surface results in less surface area available to store charge (Fig. 4.8) and a shorter charge/discharge cycle. Otherwise, as dissolution occurred, the active portion of film would remain the same size and simply extend deeper into the material as the surface

film dissolves away, resulting in the same charge storage and GCD cycle time, contrary to what is observed. It should be noted that while in Fig. 4.8b the bulk film is decreasing in size, this is simply because the active film is extending into the bulk as surface layers are dissolved. The bulk itself is not dissolving.

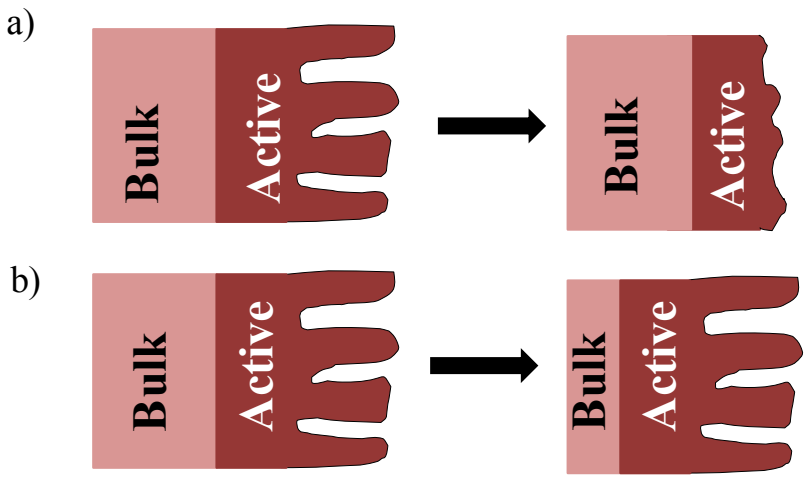

Figure 4.8. Illustration of dissolution processes causing a decrease in film roughness and surface area (a) versus maintaining film roughness and surface area (b).

Moreover, since SEM images (Fig. 4.3e and f) show no visible changes in film structure following electrochemistry in a 0.0-1.0 V window for 200 °C oven-dried films, it is unlikely the decrease in charging/discharging time for heat-treated films in this truncated window is a result of material loss or structural changes from dissolution alone. However, the increase in platelet size of the wet-stored films (Fig. 4.3g and h) decreases the surface area available to store charge, consistent with a decrease in cycle time for wet-stored films. Changes in MnOx morphology before and after electrochemistry have been reported in the literature, but with CV cycling in larger potential windows[24,61,85,109] than the 0.4-0.8 V GCD window discussed herein for wet films. Typically, this phenomenon is attributed to a dissolution-redeposition/precipitation mechanism[24,85], which is consistent with the structural changes observed for wet films post-cycling.

However, since no visible changes in structure occur for heat-treated films, another phenomenon must play a role in the decrease in cycle time with continuous cycling.

For example, other redox reactions that do not result in film dissolution could generate curvature and a decrease in cycle time as the experiment continues. Since GCD plateaus are still observed with wet films, which spent considerable time soaking in Mn^{2+}-free solution, it is unlikely the oxidation of undeposited Mn^{2+} remaining from the deposition solution explains the presence of these plateaus. More likely, certain manganese oxides are oxidizing to another form. It should be noted that this oxidation of MnOx is different than the oxidation that results in pseudocapacitance (*i.e.* Mn_2O_3 converting to MnO_2 for example[112], rather than MnOOH oxidizing to MnO_2[19]). As the sites available for oxidation are consumed, more of the applied current goes into charging the film instead of into conversion of the film. Thus, the film is able to charge more rapidly, consistent with the decreased cycle time observed with repetitive cycling (Fig. 4.7c).

Finally, CR within the electrode can equally result in GCD plateaus and a decrease in charge/discharge time with continuous cycling as illustrated with model pore data collected by Felicia Licht using a transmission line circuit (Fig. 4.9). Capacitor 1 represents the pore mouth while Capacitor 8 represents the pore base (Experimental). Since no Faradaic oxidation can take place in a hardware circuit, the plateau in the first charging curve can only be explained by charges redistributing deeper down the model pore, making it more difficult to raise the voltage at the pore mouth (Capacitor 1). During charging, charges added to the film surface can redistribute into the bulk material with time. This is evidenced in Figure 4.9 where capacitors later in the circuit (Capacitor 7 and

8), representative of regions near or at the pore base, show a slow but continual voltage rise throughout the entire experiment.

In contrast, the capacitors representing regions near the pore mouth (*e.g.* Capacitor 1 and 2) show voltages that fluctuate up and down as a result of cycling between a voltage minimum and maximum, resembling data collected from MnOx films. The curvature is absent in the discharging portion of the GCD curves (Fig. 4.7b), suggesting not all the positive charge that enters the bulk is removed during discharge, matching model pore data where the voltage deep within the pore continues to rise with cycling (Fig. 4.9, Capacitors 6, 7, and 8). With time, less of a voltage gradient exists between the pore base and the pore mouth and less voltage is lost to CR. Thus, less anodic current and less charging time is needed to raise the electrode surface to 0.8 V, resulting in a shorter charge/discharge cycle with repetitive cycling consistent with experimental data (Fig. 4.7c). These data highlight the complexity of the system under study; neither Faradaic reactions (dissolution, film conversion) nor CR can be ruled out as the cause of the plateaus, and likely a combination of these processes give rise to the observed MnOx GCD curves.

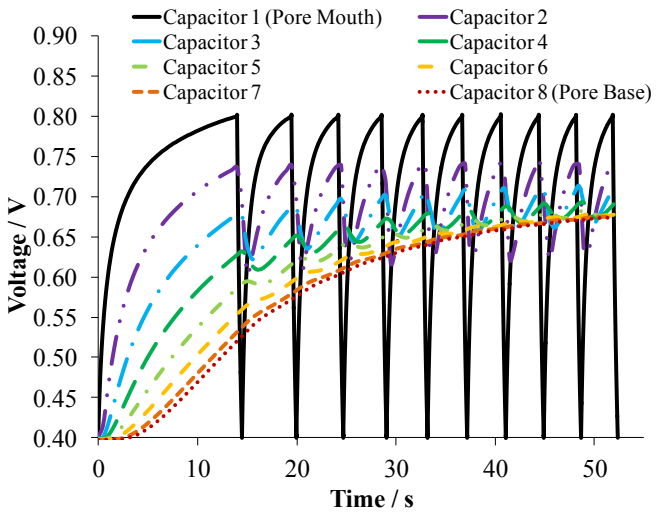

Figure 4.9. GCD data from a model pore charged at 50 µA showing plateaus in GCD can arise from CR effects. Data collected by Felicia Licht (Andreas Lab).

CE data calculated from the first GCD cycle at various currents are displayed in Figure 4.10. A log scale is used to clarify points at low currents. It should be noted that the first current tested, 1 mA, started cycle 1 at OCP, rather than 0.4 V as with the other currents, thus 1 mA data (discussed below) is omitted from this plot. As expected, the plateaus exhibited at very low currents (<0.5 mA, Fig. 4.6b) negatively impact the CE; at these rates films spend longer times at high potentials that promote oxidation and this oxidation raises the anodic but not cathodic charge, lowering CE. Even though 0.05 mA is a slower rate, the CE increases at 0.05 mA because most oxidation sites have been depleted during the preceding higher current experiments, so less oxidation can occur at 0.05 mA. At moderately low currents (0.5 – 2 mA), hydrous films show higher CEs than their heat-treated analogues, consistent with the observed CV data; this is likely the result of the greater extent of irreversible oxidation of the oven-dried films evidenced as plateaus in GCD curves and oxidation waves by CV. The irreversible nature of the reaction means that charge passed is not available for removal upon discharge, resulting in a decreased CE.

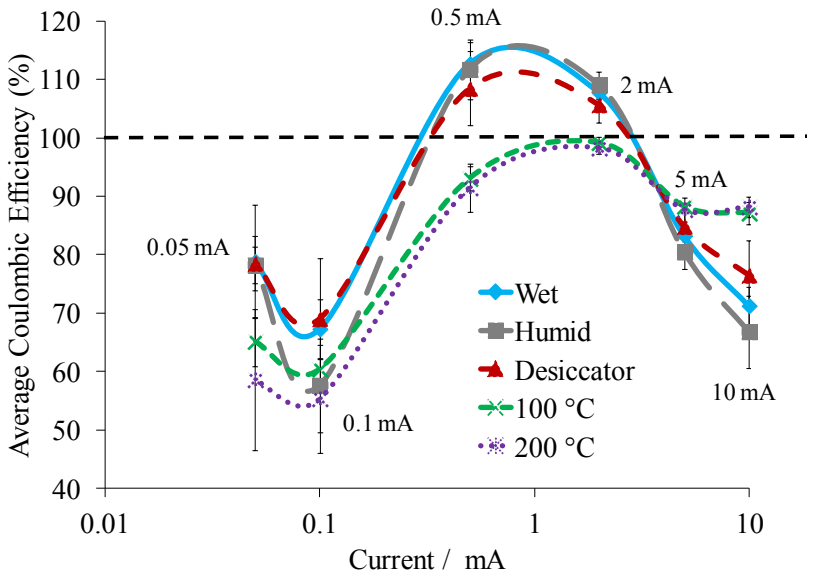

Figure 4.10. Average CEs calculated from GCD data at multiple currents. The black dashed line indicates 100% CE.

Interestingly, at the higher currents of 5 mA and 10 mA, the trend is flipped and higher currents lead to lower CEs, especially for hydrous films, indicative of a process other than oxidation dominating the CE at these rates. During charging, the surface and pore tips charge faster than the bulk film[48,50]. With time, charges redistribute to achieve a uniform potential within the film. Due to the increased charge time resulting from the plateaus at low rates, positive charges have time to move deep within the films. However, at high currents, the poor electronic conductivity of the hydrous films and the much shorter discharge time compared to charge time means not all the charge placed on the film during charging can be removed with the corresponding discharge, resulting in a low CE. Although some oxidation is likely still occurring for all films, the effect of oxidation is effectively swamped by this redistribution of charge effect at high currents where insufficient time is spent at elevated potentials to allow for significant oxidation to occur. Charge remaining on the film following rapid discharge also explains the CEs surpassing 100% for hydrous films at currents of 2 and 0.5 mA: more charge is coming off the film

than was stored during the preceding charge. This further confirms CR is happening because any charge lost to dissolution or irreversible oxidation of the film would not become accessible again upon slow discharge; only charge remaining within the electrode could be removed at a slower rate.

These data draw attention to the importance of considering experimental history in unison with ionic/electronic conductivity effects when comparing CE values and analyzing GCD curves. Many literature reports do not specify the order their GCD currents were tested and whether or not all the currents were performed on one electrode or if separate electrodes were tested at separate currents. These findings prove fundamental as they draw attention to the importance of considering CR and experimental history prior to designing GCD experiments and interpreting their results. Performing GCD tests at multiple currents consecutively on an electrode creates CR effects that influence the calculated CE on all subsequent currents. Thus, if comparisons of CEs at a variety of currents are desired, each electrode should be tested at a single current, rather than at multiple currents.

In this work, 1 mA was the first current used in GCD cycling, and thus offers a facile comparison of CEs between film types without requiring consideration of how CR effects resulting from charging with other currents influences the different types of films. At 1 mA, heat-treated MnOx shows decreased CEs (Table 5). The increased oxidation of these films amplifies the anodic but not cathodic charge, presenting as a wave in CV, a plateau in GCD, and ultimately lowering CE. It should be noted that the discharge from cycle 1 and charge from cycle 2 were used to avoid the issue of the first charge starting at OCP rather than 0.4 V.

Table 5. Average CE at 1 mA calculated from GCD data.

Drying Condition	CE at 1 mA (%)
Wet	92 ± 2
Humid	91 ± 2
Desiccator	91 ± 2
100 °C	82 ± 3
200 °C	79 ± 6

4.4.1 Impact of Ionic and Electronic Conductivity as a Result of Drying/Storage on Electrode Resistance

Considering ECs are typically used for high-power applications and often require rapid recharging (*e.g.* regenerative breaking[10,25]), it is imperative that EC materials have low resistance. As highlighted with CV data (Fig. 4.4), significant water content in MnOx films is necessary to facilitate pseudocapacitive charge storage and to achieve high capacitances[28]. Yet, the presence of too much structural water inhibits electron conductivity[26,33] and inflates device resistance. Average resistances calculated using the *i*R-drop at 1 mA are listed in Table 6. As expected, the loss of structural water during oven-drying results in decreased resistance[26,33]. These data, taken together with capacitance and energy data from CV, emphasize the importance of finding an appropriate balance between ionic and electronic conductivity to design EC materials with both minimized resistance and maximized energy storage to expand their range of applications.

Table 6. Average resistances calculated from the *i*R-drop in 1 mA GCD data.

Drying Condition	Resistance / Ω
Wet	14 ± 8
Humid	14 ± 7
Desiccator	8 ± 2
100 °C	5 ± 1
200 °C	3.5 ± 0.9

It is noteworthy that the hydrous films demonstrate poor reproducibility in terms of resistance, indicated by their large errors compared to heat-treated films. This inconsistency in resistance means it would be impractical to use hydrous MnOx in high-power applications since the large range of resistances offered by these films renders them unreliable for use in such applications. For example, while certain electrodes made with hydrous films might afford a resistance low enough to meet the high-power demands necessary to operate an emergency exit door, another electrode made in an identical fashion could be too resistive to respond with adequate speed. Given the importance of an emergency exit when needed, the large variability in resistance of hydrous MnOx would make its use in such a device not worth the risk.

4.4.2 Impact of Degree of Hydration on Power, Energy, Ragone Plots, and Film Usage

Ragone plots constructed from average Q_{dep}-normalized-energy and -power values for various electrode conditions are displayed in Figure 4.11. Oven-dried films afford high powers at high currents, while wet films show enhanced energies at low currents. The superior energy performance of the hydrous films can be attributed to the ease of cation movement through hydrous transition metal oxides, allowing for increased pseudocapacitive energy storage[2,28,34]. In contrast, the poor power performance of wet films at high rates likely arises somewhat from the poor electronic conductivity of the

films[26,33], and from a poor substrate-MnOx connection (discussed in Chapter 5). Since power is related to the rate of charge movement through the film, high powers can only be achieved with highly electrically conductive films, and this can be achieved through high-temperature drying[26].

At high rates, the energy of the hydrous films (wet, humid, desiccator) drops faster than that for heat-treated materials, indicating a smaller effective current range for the hydrous films. This implies heat treatment can offer electrodes that show higher rate capability across a wider current range at the cost of reduced energy. Heat treatment also imparts electrodes with improved power densities at high currents. Once more, these results accentuate the necessity of considering the desired application of a device when choosing a drying or storage method, as well as which properties (*e.g.* high energy or high power) would be most advantageous for that application.

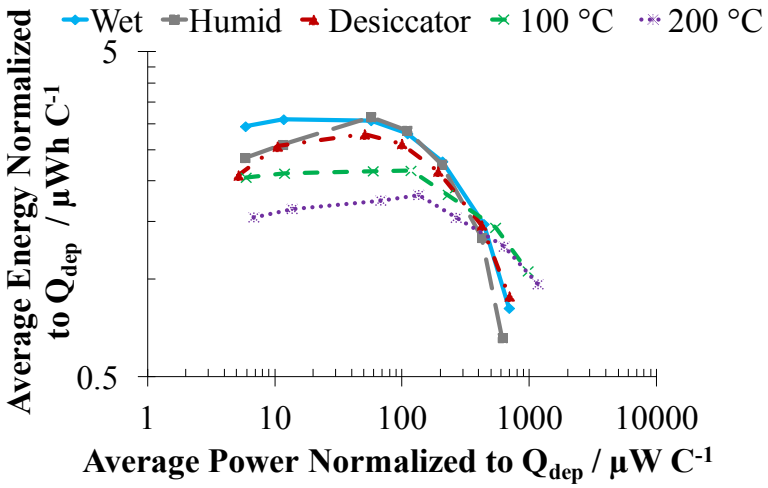

Figure 4.11. Ragone plots constructed from average energy and power values of electrodes with various drying/storage conditions.

In terms of applications, a higher film usage, the fraction of the MnOx film that contributes to energy storage, means energy density can be maintained or raised while decreasing device cost, size, or weight. In a world where hand-held and portable

electronics are the standard, it is obvious that small, lightweight devices that store large amounts of charge are desirable. Film usage is determined by evaluating the amount of charge stored on or released from an electrode (Q_{ch} or Q_{dch}, respectively) in comparison to the amount of material available to store charge (Equation 13, using Q_{ch} as an example). In this work, the amount of material available for charge storage is related to the amount of film deposited (Q_{dep}).

$$Film\ usage = \frac{Q_{ch}}{Q_{dep}} \times 100\% \qquad (13)$$

Q_{dep} is proportional to the amount of deposited oxide. However, since the deposition of these films was carried out under constant potential, it is recognized that reactions other than deposition reactions can occur, such as the O_2 evolution reaction[112]. These reactions can contribute to a portion of the current recorded during deposition. Nonetheless, the film uniformity and absence of visible bubble formation during the deposition suggests Q_{dep} is an adequate approximation for the amount of MnOx on the electrode in this work. Table 7 lists film usages for all MnOx conditions.

Table 7. Average anodic and cathodic MnOx film usage (%) for electrodes made with various drying/storage conditions.

Drying Condition	Film Usage Anodic %	Film Usage Cathodic %
Wet	7.9 ± 0.1	7.3 ± 0.1
Humid	8.2 ± 0.6	7.4 ± 0.6
Desiccator	7.3 ± 0.4	6.7 ± 0.4
100 °C	6.5 ± 0.4	5.5 ± 0.4
200 °C	6.0 ± 0.8	4.8 ± 0.4

The electrodes yield film usage ratios ranging from approximately 5 to 8%, suggestive of only a small fraction of the film actually being used. Ratios of 10%[113] and 15%[46] have been reported in the literature, which are not dramatically greater. A small

cation diffusion depth relative to the thickness of MnOx layers has been identified, implying insertion and deinsertion of cations is limited to areas near the electrode surface rather than throughout the entirety of the bulk material[29,64,114,115], consistent with low film usage ratios.

One additional factor likely contributing to the modest film usage ratios in this study is the inaccurate representation of the amount of film deposited provided by Q_{dep}. As discussed above, reactions other than deposition reactions are likely occurring at the deposition potential, thereby slightly inflating the charge recorded during deposition. If deposition alone was happening, Q_{dep} would be smaller and film usage ratios would improve.

Given the variation in electronic and ionic mobilities produced by different drying and storage methods, film usage ratios are not consistent among different electrode types. As expected, film usage decreases with decreased hydration; fewer sites available for cation diffusion as a result of heating[2,28,34] would mean a decreased electroactive volume that can participate in pseudocapacitive charge storage and limit the amount of film used. Similar film usage trends were observed with CV data (not shown). Additionally, pore sealing during heating has been proposed[28], which would decrease accessible surface area for charge storage and lower film usage. Unfortunately, the SEM used in this work did not have adequate resolution to identify such microstructural differences. In the future, SEM analysis under stronger magnification should be conducted to identify if microstructural changes that could impact film usage occur during heat treatment.

4.5 Hydration Affects Electrochemical Stability with Long-Term Cycling

As previously mentioned, ICP-OES results confirm stability issues by detecting Mn in electrolyte post-cycling. However, the Mn deposits on the counter electrode could not be included in the ICP-OES measurement, but would represent a significant fraction of the Mn dissolved. Therefore, the percentage of charge retained, another measure of how much the film is changing with cycling, was used as a figure of merit for stability. Percent charge retention was monitored for all films during 1000 cycles of 1 mA cycling in a potential window of 0.4-0.8 V (Fig. 4.12).

Similar to literature reports, drying MnOx electrodes at elevated temperatures offers enhanced cycling stability as opposed to room-temperature drying (humid, desiccator-dried)[26,31]. Nonetheless, wet films demonstrate even greater charge retention, suggesting retaining film hydration by keeping electrodes wet is more effective in creating stable films than employing heat treatments. This is likely the result of the less severe oxidation experienced by hydrous MnOx compared to its heat-treated counterparts, resulting in a film less susceptible to changes during cycling. Wet storage also reduces cracking within the films compared to hydrous room-temperature-dried films, as evidenced by SEM imaging (Fig. 4.3). If cracking generates sites more susceptible to oxidation or dissolution, this could also explain why wet electrodes show improved stability compared to their heat-treated counterparts. The charge loss observed with wet films is likely at least in part the consequence of the decrease in surface area of the wet films that occurs during cycling as the MnOx platelets increase in size (Fig. 4.3g and h).

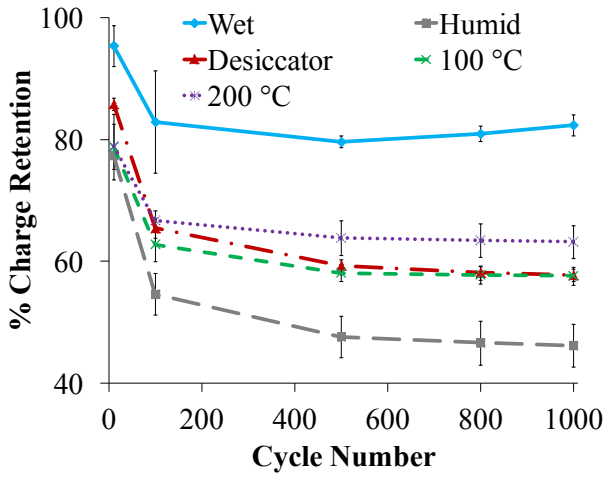

Figure 4.12. Percent charge retention as a function of cycle number during 1 mA galvanostatic cycling for MnOx films made with various drying and storage conditions.

4.5.1 Hydration Influences Physical Stability and Electrode Aging

Visual evidence of enhanced physical stability of wet films was also observed as film chipping and peeling at the current collector edges and corners during drying was common with both room- and oven-dried films (Fig. 4.13a and b), but was rare with films stored in electrolyte. Film shrinkage producing cracks is common for MnOx films on stainless steel[116], and SEM images validate film cracking as a cause for inferior physical stability in this work since cracks were more prominent in high-temperature-dried films (Section 4.1). Although SEM images indicate worse cracking for oven-dried films, the improved connection between the MnOx and the stainless steel substrate achieved through heat-treatment (discussed in Chapter 5) likely improves the stability of the heat-treated films over those that were dried at room temperature (humid) (Fig. 4.12).

While film peeling around electrode edges was prevented by employing a wet storage method in comparison to drying films in any fashion, films kept in electrolyte for more than a month immediately crinkled and detached from their stainless steel substrates upon application of a potential (Fig. 4.13c), resulting in little to no electrical connection.

Rinsing these electrodes resulted in instantaneous film delamination. In contrast, similarly-aged 200 °C oven-dried films showed no evidence of aging influencing their stability. These results indicate that the superior stability of wet films might not withstand the period in which many devices rest idle in a factory or store before use. Yet, heat-treated films can lose a portion of their active material before even being used in experiments, which is both wasteful and undesirable. Ultimately, these findings illustrate the necessity of evaluating how age affects device performance.

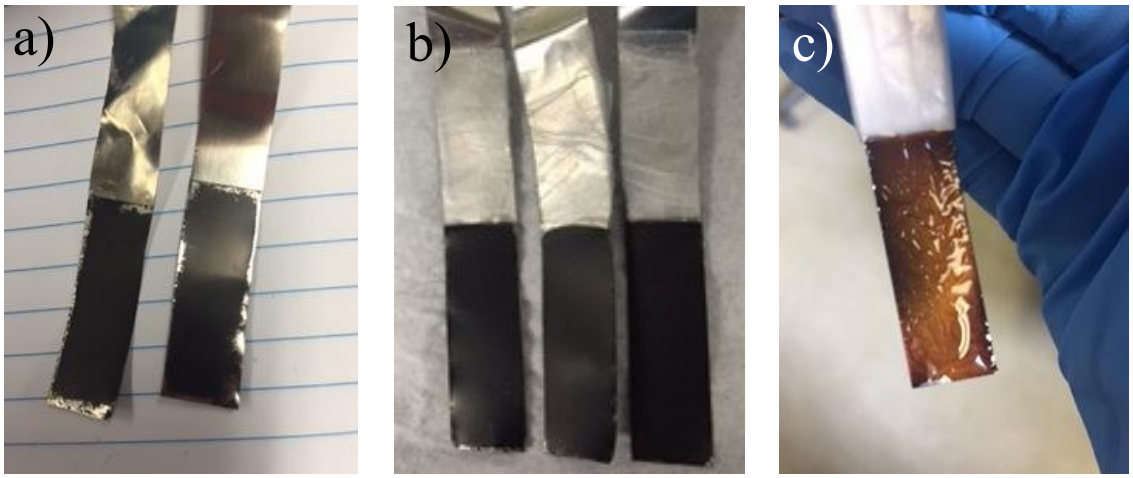

Figure 4.13. Photograph of a) 200 ºC oven-dried films and b) humid films peeling along the edges post-drying and c) a wet film crinkling and detaching from its stainless steel substrate following electrochemistry, prior to rinsing.

4.6 Conclusions

Of the various storage and drying methods investigated, no one method proves optimal across all the electrochemical properties that influence EC performance. Both maximizing hydration through wet storage and eliminating water content through high-temperature drying offer unique advantages and disadvantages. Hydrous films, particularly those stored in electrolyte, impart elevated capacitances and energies as a result of increased pseudocapacitive charge storage[28]. These features, as well as the

improved CE, enhanced cycling stability, and film crack prevention offered by wet films, are necessary to minimize device size and cost, reduce cell failure, and develop ECs that require recharge less often.

However, the high power required for typical EC applications is better provided through the good electronic conductivity (and substrate connectivity, Chapter 5) achieved with heat treatment[26,33]. Oven-dried films also present improved EEs, meaning a greater portion of stored energy can be accessed, and demonstrate better aging (*i.e.* less delamination post-storage). Conversely, heat treatment results in more severe film cracking and peeling, causing a decreased amount of active material on oven-dried electrodes.

Oven-dried films provide enhanced rate capability, evidenced by a less severe decrease in energy with an increase in charging/discharging rate. However, the energy of hydrous films surpasses the energy of heat-treated films at most currents, even at currents where wet electrodes struggle to keep up. Although hydrous MnOx experiences a greater energy loss at high rates, its energies never fall significantly below those of the heat-treated MnOx, indicating maximizing hydration optimizes energy density.

These results draw attention to the importance of designing and developing films that combine the benefits of both hydrous and anhydrous MnOx in order to optimize the performance of EC electrodes. The findings reported in this chapter inspired the development of the double-deposition films described in the next chapter to afford electrodes with high energy and capacitance without sacrificing high power and rate capability.

Chapter 5 Electrochemical Performance of Novel Double-Deposition MnOx Films

5.1 Introduction

Upon evaluation of the data discussed in Chapter 4 and consideration of the benefits of both electronic and ionic conductivity, achieved with decreased and increased degrees of hydration, respectively[26,33], a novel MnOx deposition method was developed. This double-deposition method involves a 200 °C heat treatment step in combination with a second deposition followed by wet storage. This procedure was designed to improve the overall performance of MnOx electrodes for EC applications by providing films with the high energies, capacitances, CEs, and film usage ratios evidenced with wet films while maintaining the low resistances, high powers, and high EEs achieved with heat treatment. Ideally, this method will also provide films resistant to cracking and chipping by maintaining hydration while preventing delamination with age through formation of a stronger substrate-film connection. Different heat-treated-layer thicknesses were examined to identify the appropriate ratio of anhydrous and hydrous material to optimize electrode performance.

Since EC energy is proportional to the square of the device's operating window[9,15,113], commonly the potential window is widened in order to improve the energy density. For this reason, tests in a more commercially desirable expanded potential window of 0.0-1.0 V vs. SCE were conducted on certain electrodes that showed promising properties such as high capacitance or high power.

5.2 Ratio of Ionically to Electronically Conductive Film Affects Cyclic Voltammetry Performance

A representative CV of a MnOx film from each double-deposition condition is shown in Figure 5.1. Representative CVs of single-deposition films evidencing the highest (wet) and lowest (200 °C oven-dried) capacitances (from Fig. 4.4) are plotted on the same graph to facilitate comparison. Recall the double-deposition films are named according to their ratio of $Q_{dep}1$:$Q_{dep}2$ (heat-treated film: not heat-treated film, Experimental). For example, a 10:90 film is made with the first 10% of its MnOx film heat-treated, and the remaining 90% deposited onto the heat-treated layer before storing the entire electrode wet. All double-deposition films present CV currents that immediately switch signs when the direction of the potential sweep is changed, indicative of the low resistance observed with oven-dried single-deposition films. An inverse relationship is found between capacitance (and CV size) and the thickness of the heat-treated layer. 10:90 electrodes, those with the thinnest heat-treated layer of film of all films tested, afford capacitances that do not differ significantly from the hydrous wet or humid single-deposition films. This is significant when taken into consideration with the less resistive CVs of the 10:90 films; this double-deposition method can decrease electrode resistance without negatively affecting the device's ability to store energy.

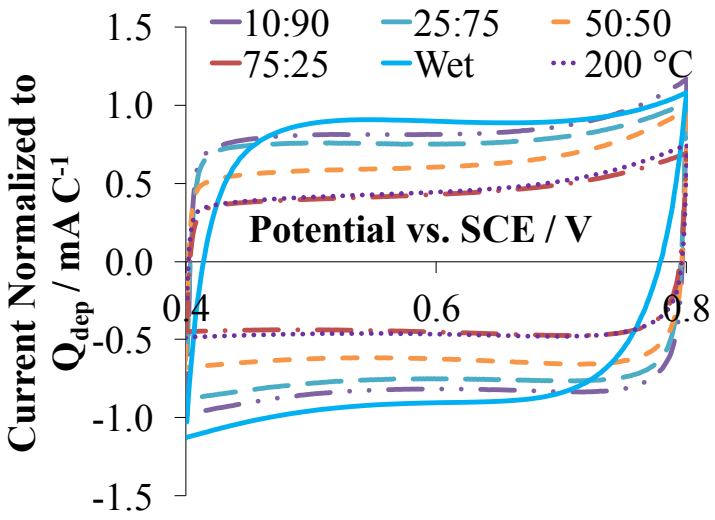

Figure 5.1. Representative CVs of double-deposition films recorded at a 10 mV s^{-1} sweep rate in a 0.4-0.8 V window. The representative wet and 200 °C single-deposition electrode CV are added for comparison.

Average capacitances, E_a, E_c, and EE of double-deposition MnOx films, along with those of wet (high energy, low EE) and 200 °C oven-dried films (low energy, high EE) for comparison, are tabulated in Table 8. In agreement with the capacitance trend, energies decline as the portion of heat-treated film increases. As a consequence of their decreased resistance, improved EEs are observed for double-deposition films compared to wet MnOx (Table 8). In fact, double-deposition films generally show higher EEs than all single-deposition film types. The decreased resistance is likely from heat treatment creating a better connection between the oxide and the stainless steel current collector. This is evidenced by the 100 °C (Fig. 4.4) and 200 °C oven-dried films, and all double-deposition films, showing vertical current switches with changing of the potential sweep direction, even though these films possess different heat-treated-layer thicknesses.

Table 8. Average capacitances, E_as and E_cs, and energy efficiencies for double-deposition electrodes determined by CV. Wet and 200 °C single-deposition electrode values are also listed for comparison.

Electrode Type	C_{Qdep} mF C^{-1}	E_a mJ C^{-1}	E_c mJ C^{-1}	EE (%)
10:90	83 ± 3	21.0 ± 0.7	19.6 ± 0.6	93.3 ± 0.5
25:75	74 ± 3	19.0 ± 0.7	18 ± 2	96 ± 6
50:50	61 ± 3	16 ± 1	15 ± 1	93.4 ± 0.9
75:25	44 ± 2	11.1 ± 0.6	10.4 ± 0.5	94 ± 1
Wet	89 ± 4	21.0 ± 0.9	18 ± 1	88 ± 2
200 °C	44 ± 3	12 ± 1	10.9 ± 0.9	91.1 ± 0.9

These results demonstrate that the benefits of both wet storage (high capacitance and energy) and heat treatment (low resistance, high EE) are accessible through the double-deposition method, as long as the heat-treated layer of film is kept thin. Keeping the heat-treated layer thin allows the hydrous nature of the majority of the film to maintain high energy and capacitance, while the decreased resistance obtained via fusing the film to its substrate allows for a more efficient delivery of the stored energy. Application-wise, this means that electronics powered with 10:90 films could run longer before requiring recharge than a device powered by non-wet single-deposition films. In addition, a device powered by 10:90 films would waste less energy, owing to their enhanced EEs, than a device powered by wet MnOx.

5.3 Balance of Anhydrous and Hydrous Film Influences Electrode Performance during Galvanostatic Cycling

Double-deposition MnOx films display typical triangular charging curves at high currents (2 mA, Fig. 5.2a), with slightly more distorted triangular shapes at low currents (0.5 mA, Fig. 5.2b), where plateaus start to develop as the potential approaches 0.8 V. Similar to single-deposition films, the time required to complete one charge/discharge cycle increases with increasing degree of hydration (*i.e.* larger $Q_{dep}2$). This draws

attention to the improved charge-storing ability of hydrous MnOx. Since the poor electronic conductivity of electrodes made with wet films can be effectively eliminated through heat-treating a base layer of film, independent of the thickness of the heat-treated layer, a thin oven-dried layer proves optimal. All films with a heat-treated base layer offer low resistance, evidenced by the vertical current response upon changing sweep direction in the CV, but capacitance increases with increasing hydration. Thus, using a thin heat-treated layer allows for charge storage to be maximized by maximizing the fraction of hydrous film, without raising the resistance of the electrode.

Again consistent with single-deposition data, a decrease in the charge/discharge time is observed with continuous cycling at 1 mA (Fig. 5.2c). This indicates that although double-deposition films correct for the high resistance of hydrous films and the poor charge storage performance of heat-treated MnOx, these films are not immune to the same changes with cycling (*e.g.* oxidation, dissolution, CR effects) experienced by single-deposition films. The change in cycle time for double-deposition films will be discussed further in Section 5.3.2.

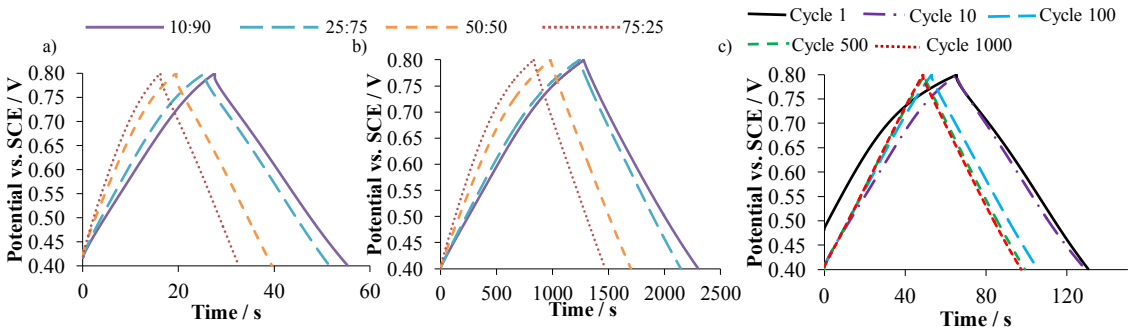

Figure 5.2. Representative GCD curves for double-deposition films at a) 2 mA and b) 0.5 mA, and c) GCD curves recorded at 1 mA showing decreased cycling time with consecutive cycling for a representative 10:90 film.

Average CEs, film usage percentages, and resistances of double-deposition films calculated from 1 mA GCD data are listed in Table 9. Double-deposition films display

CEs comparable to hydrous single-deposition films at 1 mA, surpassing the CEs of fully oven-dried films.

Table 9. Average CEs, film usage, and resistances for double-deposition films calculated from 1 mA GCD data. Wet and 200 °C oven-dried single-deposition film data are shown for comparison.

Electrode Type	Average CE at 1 mA (%)	Film Usage Anodic (%)	Film Usage Cathodic (%)	Average Resistance Ω
10:90	90 ± 3	8.4 ± 0.3	7.69 ± 0.09	2.6 ± 0.5
25:75	92 ± 1	7.8 ± 0.1	7.2 ± 0.2	2.8 ± 0.4
50:50	92.2 ± 0.7	6.00 ± 0.09	5.6 ± 0.1	3.3 ± 0.2
75:25	90 ± 1	5.2 ± 0.2	4.8 ± 0.2	2.4 ± 0.5
Wet	92 ± 2	7.9 ± 0.1	7.3 ± 0.1	14 ± 8
200 °C	79 ± 6	6.0 ± 0.8	4.8 ± 0.4	3.5 ± 0.9

Figure 5.3 depicts average CEs calculated for the first GCD cycle as a function of charging current. A logarithmic x-axis is used to separate data points collected at low currents. As with the single-deposition data, 1 mA data is omitted from this plot since cycle 1 at 1 mA started at the electrode's OCP instead of at 0.4 V, the potential at which charging with all other currents initiated. Wet and 200 °C CE data from Chapter 4 is included to facilitate comparison. In contrast with the CE pattern observed with single-deposition films, where the drying/storage condition that results in the highest CE depends on the current used (CEs greater for hydrous films at low currents, CEs greater for anhydrous films at high currents), CEs of double-deposition films are closely matched at all currents, independent of the $Q_{dep}1$:$Q_{dep}2$ ratio. This is not surprising since the active fractions of these films (primarily volume near the surface) have nearly identical degrees of hydration and it is this region near the surface of the film where charge storage takes place[64,114,115]. Thus, ionic and electronic mobility should be relatively consistent across the active portion of film of all double-deposition electrodes.

Recall that CEs of single-deposition films are influenced differently by experimental history due to the differences in the electronic and ionic mobility, and thus overall resistance, of anhydrous vs. hydrous MnOx. Electronic conductivity is promoted in anhydrous MnOx, while ionic diffusivity is improved with increased hydration[26,33]. In addition, CV data (Fig. 5.1) suggests low resistance is achieved as long as some base layer of the film is heat treated, whether it is the whole film (200 °C) or a fraction of the film (double-deposition films), implying heat treatment imparts good substrate-film contact. With hydrous single-deposition films (wet, humid, desiccator), the poor electronic conductivity of the oxide and poor connection between the film and substrate means stored charge cannot be completely removed during discharge at fast discharging rates. This results in poor CEs at high rates, and CEs exceeding 100% during the subsequent low currents for hydrous MnOx because the charge that remains on these films after rapid discharge can be removed when the discharge rate is slowed (Section 4.4). The low CEs observed at high currents (5 and 10 mA) relative to the heightened CEs achieved in the subsequent low current tests for double-deposition films is consistent with this theory.

However, the improved electronic conductivity of the double-deposition films allows them to maintain higher CEs than wet films at high currents and means that their CEs are not as high at subsequent low currents. This is because the enhanced substrate-film connection of the double-deposition films allows them to have the low resistance and high rate capability of the fully heat-treated single deposition films, resulting in less charge being trapped within the double-deposition films during rapid discharge. These

results suggest modifying the interface between the current collector and the MnOx film significantly improves CR.

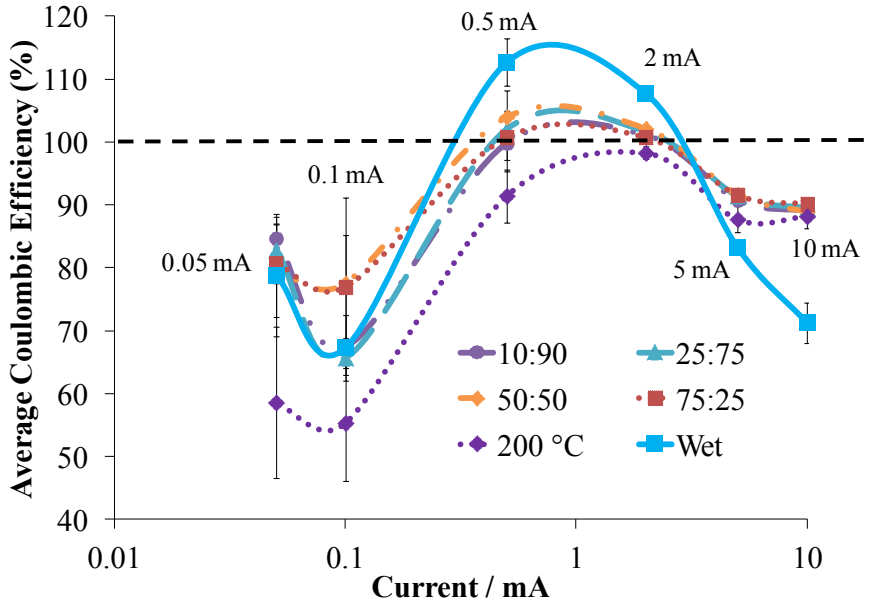

Figure 5.3. Average CEs calculated at various GCD currents for double-deposition films with wet and 200 °C single-deposition films included for comparison. The dashed black line indicates a CE of 100%.

An inverse relationship is seen between film usage and the portion of film dried (Table 9), consistent with the trend evidenced by the single-deposition MnOx films; this is likely the result of less film available for pseudocapacitive charge storage when a greater fraction of the film is dried at 200 °C. These results highlight implementing a double-deposition method that maximizes film hydration maximizes the amount of charge that can be stored on the electrode. A film made of predominantly hydrous MnOx (*e.g.* a 10:90 film) can store more charge, and thus operate for longer before requiring recharge, than a film of primarily anhydrous MnOx of the same dimensions.

Resistance of double-deposition electrodes proves independent of the ratio of $Q_{dep}1$:$Q_{dep}2$ (Table 9), and is similar to that for the 100 and 200 °C oven-dried single-

deposition electrodes. It is clear that an improved connection between the film and the current collector is realized with high-temperature drying. It is this connection, rather than the relative water content among films, that dominates the electrode's electronic resistivity. Otherwise, 10:90 electrodes would be expected to have greater resistance than the electrodes with a greater portion of heat-treated film (*e.g.* 75:25 films), which is not the case. As long as the heat-treated portion of the film is limited to a thin base layer, the low resistance and elevated EEs of oven-dried films are attainable without losing the benefits of a more hydrous film. On the other hand, a thick fraction of heat-treated film results in decreased capacitance and energy with no significant improvement in conductivity, highlighting the 10:90 films as the superior double-deposition condition.

5.3.1 Ragone Plots of Double-Deposition Electrodes

Ragone plots (Fig. 5.4) produced by 10:90 and 25:75 films display less severe energy drops at high power compared to hydrous single-deposition films. This suggests the large energy drop experienced by hydrous MnOx at high rates due to electronic limitations of the electrode is eliminated by oven-drying a base layer of film. In addition, the heat-treated base layer also allows all double-deposition conditions to achieve equally high powers as the fully-heat-treated single-deposition films, without sacrificing energy density, if the majority of the film is hydrous. At high currents, the 10:90 films present the highest energy of all film compositions, again highlighting the 10:90 method as the optimal synthesis.

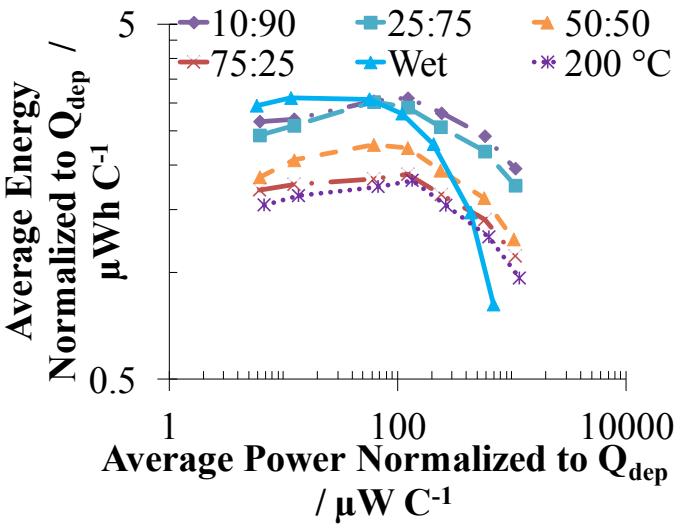

Figure 5.4. Ragone plot constructed from average energy and power values for double-deposition films. Ragone plots for wet and 200 °C oven-dried single-deposition films are shown for comparison.

Likely, as both the top and bottom layer of film are comprised of the same material, these layers adhere well to each other. Similarly, heating imparts a good connection between the MnOx and the substrate, allowing the electrode to have sufficiently low resistance to keep up when high currents are applied, while still having adequate hydrous regions to store energy pseudocapacitively. Clearly, combining both heat treatment and wet storage offers a balance of hydrous material and electrical conductivity that can afford the high powers evidenced by oven-dried films without abandoning the high energies available with hydrated films.

5.3.2 Electrochemical and Physical Stability of Double-Deposition Electrodes

Improved cycling stability is witnessed with double-deposition films in comparison to all dried single-deposition MnOx conditions, illustrated by the greater percent charge retention (Figure 5.5). The percent charge retention of the double-deposition films proved independent of the ratio of $Q_{dep}1$ to $Q_{dep}2$.

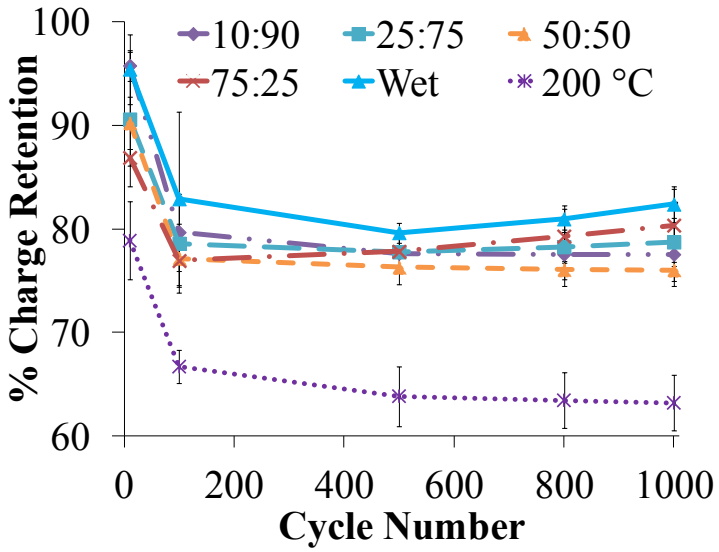

Figure 5.5. Average percent charge retention as a function of cycle number during 1 mA galvanostatic cycling for double-deposition films with wet and 200 °C oven-dried films shown for comparison.

This enhanced stability can likely be attributed to the smooth, crack-free surface achieved via the double-deposition method, visible in the SEM micrograph of a 10:90 film (Figure 5.6a). The micrograph of a 200 °C oven-dried film from Fig. 4.3 is shown in panel b for comparison. The uniformity of the 10:90 MnOx films likely contributes to the improved stability of these films since cracks in the single-deposition films typically developed near thick agglomerations of MnOx (SEM, Fig. 4.3), which are absent from the 10:90 film. In addition, implementing a double-deposition method that keeps a thin oven-dried layer avoids the problem of chipping and peeling during drying because thinner films synthesized in-lab were better able to resist cracking, consistent with literature reports[116]. These thin dried layers then likely give stability to the whole film, possibly from the enhanced substrate-film connection achieved with oven drying.

Figure 5.6c and d show SEM images at 50000x magnification that indicate that the platelets of 10:90 films increase in size following electrochemistry (2000 CV cycles, 10 mV s^{-1}, 0.0-1.0 V window), matching what was observed with wet-stored single-

deposition films in the truncated window. This change in surface area likely contributes to the decrease in charge time with continuous cycling observed for double-deposition films (Fig. 5.2c) and could also explain why the wet and double-deposition films show similar charge loss with repetitive cycling (Fig. 5.5); both films show a similar decrease in surface area following electrochemistry.

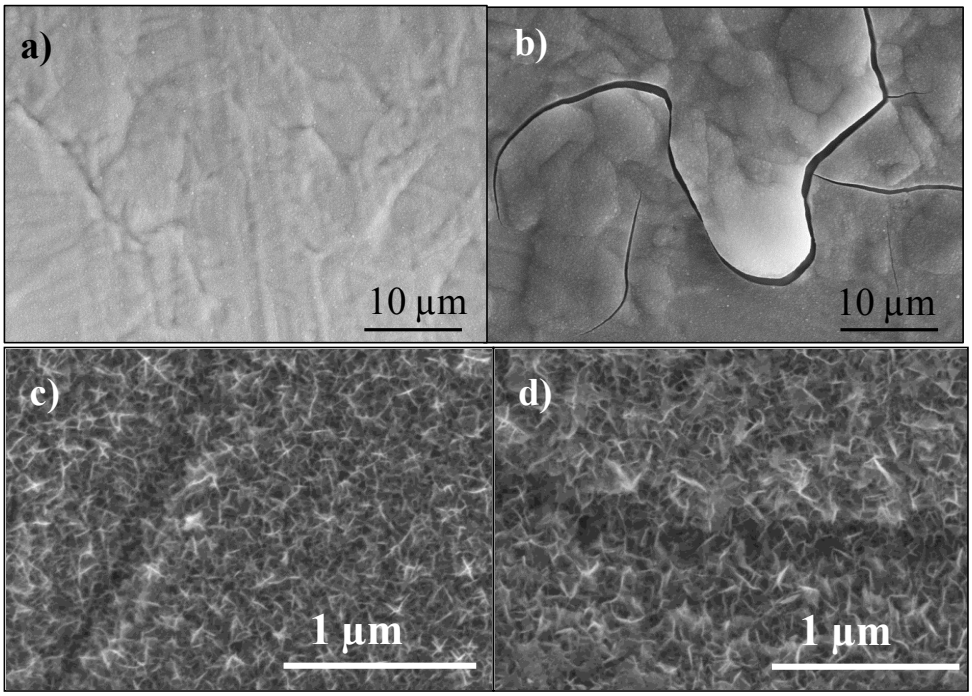

Figure 5.6. SEM micrographs at 5000x of a) a 10:90 electrode and b) and 200 °C oven-dried electrode prior to electrochemistry. Panels c) and d) show a 10:90 electrode before and after 2000 cycles CV in a 0.0-1.0 V window, respectively, at 50000x magnification.

Unlike wet single-deposition films, double-deposition films show no evidence that electrode aging is detrimental to their performance. Double-deposition films did not delaminate during electrochemistry even if they were made several weeks prior to their use in experiments. However, double-deposition electrodes were not fully immune to peeling as film loss along edges of double-deposition electrodes was occasionally observed with extensive cycling. Interestingly, peeling of these films resulted in a smoother region of exposed stainless steel along the electrode edge compared to the

uneven jagged region along the edge observed with single-deposition films, as shown in Figure 5.7. This is perhaps explained by the smooth surface of the double-deposition films (Fig. 5.6), as opposed to the uneven agglomeration of MnOx observed with the single-deposition films that could promote uneven peeling. Nonetheless, the double-deposition method ensures no active material is lost until extensive experiments have been conducted on the electrode, as it eliminates the chipping and peeling that occurs during drying when the entire film is dried.

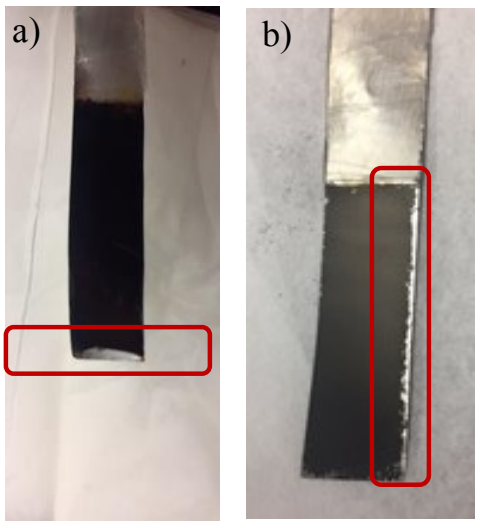

Figure 5.7. a) 10:90 film showing smooth peeling along the bottom edge following a multicurrent GCD experiment and b) a 200 °C oven-dried film showing rougher edges around the peeled film prior to electrochemistry.

5.4 Tests in an Expanded 0.0-1.0 V Window

As the energy and power densities of ECs are proportional to the square of the potential range over which the device operates[15,113], increasing the operational window can improve these properties[9]. Therefore, the three MnOx film preparation conditions displaying superior electrochemical properties were evaluated in an expanded potential window of 0.0 – 1.0 V. Wet films, owing to their high energy and capacitance, 200 °C oven-dried films, as a result of their increased power and decreased resistivity, and 10:90

films, owing to their combination of the benefits observed with the two previously listed film conditions, were chosen.

5.4.1 Effect of Hydration on Electrochemical Performance in an Expanded Potential Window

As previously mentioned, increasing the operating window of a device serves as one method to enhance device energy density[9]. Unfortunately, rapid delamination of wet-stored films, even when freshly made, occurred in the expanded 0.0-1.0 V window, preventing the collection of useful data for these films and resulting in omission of their data in CV and GCD discussions in this chapter. This is likely the result of the poor connection between the MnOx and the current collector when heat treatment is not employed.

Although hydrous films offer increased energy density, they are clearly limited by the potential window within which they can operate. This emphasizes the significance of including the heat-treated base layer in the double-deposition method. Without a good connection to the current collector, fully hydrous MnOx films are impractical for use in consumer devices since the voltage window in which these devices operate causes the films to detach from their substrates, resulting in immediate device failure. In contrast, the improved connection imparted by their thin heat-treated base layer of MnOx means 10:90 films can withstand an expanded potential window, while their significantly larger hydrous fraction of film allows them to have energy densities comparable to wet single-deposition films. Therefore, the coupling of these two features allows for maximized device energy.

Following 2000 CV cycles in a 0.0-1.0 V window (Fig. 5.8), both 200 °C oven-dried and 10:90 film conditions result in similar CV shapes. As expected, the increased

water content of the 10:90 films offers increased capacitance compared to their fully-dried analogues, evidenced by a higher current (larger CV) in the flat, mirror-image capacitive region (~0.2 V to 0.7 V).

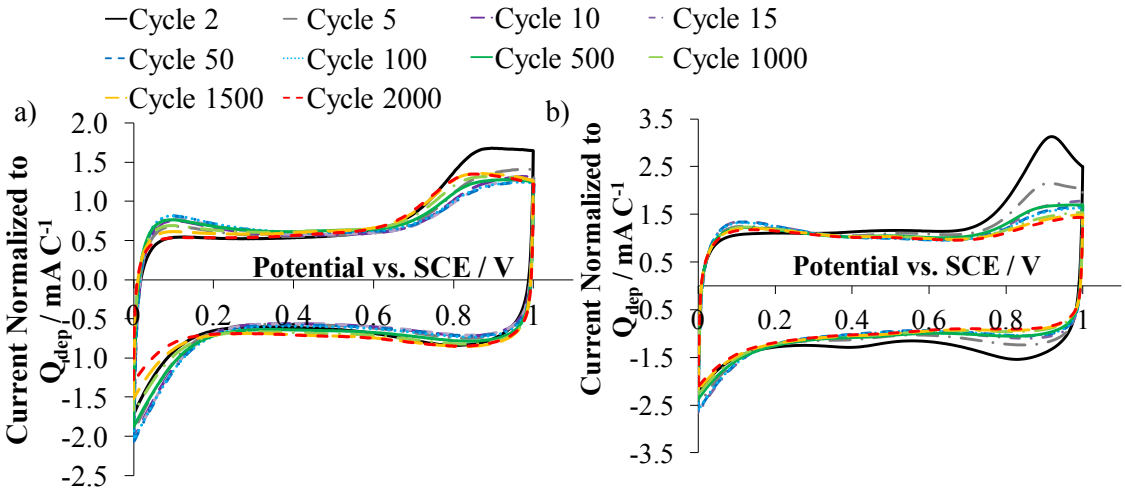

Figure 5.8. Representative CVs of a) 200 °C oven-dried film and b) 10:90 film recorded in a 0.0-1.0 V potential window at a sweep rate of 10 mV s^{-1}.

Both electrode conditions exhibit reduction waves initiating around 0.2 V that increase in the initial few cycles and then gradually decrease with cycling. This is likely the formation of solution-soluble Mn^{2+} ions[21,23,112] from the disproportionation of Mn(III) in Mn_2O_3 or MnOOH to MnO_2 (Mn(IV)) and aqueous Mn(II)[19,21,23,25,84–86]. As this dissolution occurs, sites in the film susceptible to this reaction are consumed. It is possible Mn^{2+} from less stable regions of film, such as at the surface of thick agglomerates or near the electrode edges where peeling occurs, dissolves and then redeposits on a different region of the film or in a different form making it less susceptible to dissolution during the following cycle. This could explain the overall decrease in reduction wave with repetitive cycling. Dissolution/redeposition during cycling has been previously reported[24,85], and pale yellow-brown thin layers of MnOx

occasionally form with cycling on exposed stainless steel where the original film peeled off, serving as visual evidence for this occurrence.

A small, broad cathodic wave is observed above 0.8 V, especially in the CV of the 10:90 films. Interestingly, this feature nearly disappears after only a few cycles. A similar broad wave has been observed in the literature for λ-MnO_2[117] and heat-treated amorphous MnOx where the size of the reduction bump decreased with increasing heat-treatment temperature[29], perhaps explaining why this feature is much less obvious in the 200 °C oven-dried films' CVs, where the entire film is dried at high temperature. In addition, different crystal structures of MnO_2 have been reported to present slightly different CVs[117], so it is possible that different structures form preferentially in heat-treated MnOx compared to as-deposited (hydrous) films. Since SEM images confirm the single- and double-deposition methods generate films with surfaces that appear different, it is possible the hydrous layer in the 10:90 films contains more of the MnOx form responsible for the broad reduction peak at 0.8 V than the 200 °C oven-dried layer. However, this broad reduction peak is eliminated rapidly with cycling, suggesting some film conversion is taking place in this window.

As with the 0.4-0.8 V window, an oxidation wave is present at the upper potential extreme. Again, this oxidation wave initiates at a lower potential (~0.6 V) for the 200 °C oven-dried MnOx compared to the more hydrous films (~0.7 V). The reaction or process is irreversible, since a corresponding reduction wave of equal magnitude is absent; thus, the anodic and cathodic portions of the CV are not mirror images, confirming the reaction responsible for the wave is not pseudocapacitive.

One possible explanation for the oxidation wave is redeposition of the dissolved Mn^{2+}. As discussed above, cycling in this window can cause a dissolution/redeposition process to take place[24,85]. Dissolution would slow down if MnOx dissolves and then redeposits in a more stable location where it is less susceptible to dissolve again, as discussed above. Therefore, the decrease in oxidation is possibly the result of less MnOx redepositing as a consequence of less MnOx dissolving after the initial cycles; with less dissolution, less Mn^{2+} ions are present in solution to be oxidized back onto the electrode.

In evaluating film dissolution it is noteworthy that electrolyte discolouration to a very pale creamy-yellowish colour with an orange-brown precipitate occurs often with cycling in this window for 2000 cycles (Fig. 5.9a-b). Although formation of $Mn(OH)_2$ or MnOOH from Mn^{2+} in basic conditions[23] could result in a white ($Mn(OH)_2$) and reddish-brown (MnOOH) species[118,119], the pH of the Na_2SO_4 solution is approximately 6.2, which is slightly acidic. Nonetheless, local pH changes from the reversible insertion/deinsertion of protons during charging and discharging could result in alternating basic and acidic conditions near the film surface, with acidity enhancing dissolution and the basic environment promoting formation of $Mn(OH)_2$ [23]. Although dissolution to Mn^{2+} is likely occurring, the low concentrations of Mn ions in solution from ICP-OES analysis suggest dissolved Mn does not explain the brown precipitate. It is more probable that the entire film is simply disintegrating and flaking off in its deposited form (brownish-red in colour), rather than just Mn ions dissolving out from the film, that explains the precipitate at this pH.

Since the concentration of Mn ions present in electrolyte following cycling in the expanded window for 200 °C oven-dried and 10:90 films is not statistically different

based on ICP-OES results (0.2 to 1.5 ppm range vs. 0.5 to 2.5 ppm range, respectively), no conclusions can be made as to whether one film type dissolves more readily than another. In addition, certain 200 °C oven-dried films and 10:90 films showed extensive film degradation during this experiment, while other identically-made films showed very little degradation (Fig. 5.9c-d). Occasionally after cycling discoloured regions appear on the film, which easily peel off during post-experiment rinsing. Other times, films remain intact, even if discoloured regions had formed. Thus, visual observations could also not be used to identify if a certain electrode condition offered enhanced stability in this window. While this experiment was designed to push the electrodes to their limit, it is clear both heat-treated and 10:90 films, like many other MnOx films in the literature[9,20–25], still require significant improvement in terms of stability before they can be used in a commercial device. Hundreds of thousands to millions of cycles in such a potential window would be standard for a practical commercial EC.

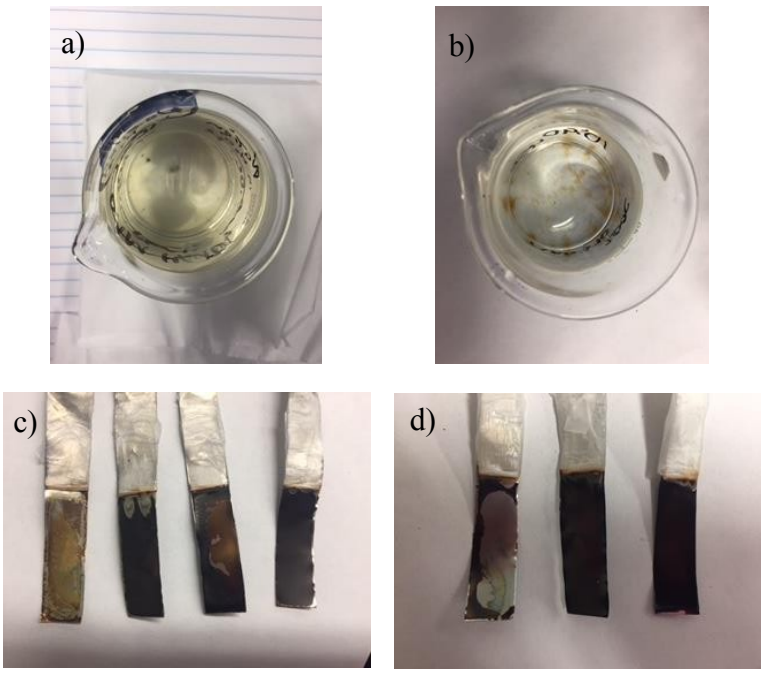

Figure 5.9. a) Discoloured electrolyte following 2000 CV cycles of a 200 °C oven-dried film in a 0.0-1.0 V window, b) discoloured electrolyte showing brown precipitate following 2000 CV cycles of a 10:90 film in a 0.0-1.0 V window. Panels c) and d) show 10:90 and 200 °C electrodes, respectively, following 2000 CV cycles in a 0.0-1.0 V window with varying degrees of film degradation post-rinsing.

Secondly, site-limited irreversible oxidation of the film could also generate an oxidation wave in the CV. Slight changes in Mn oxidation state have been reported with heating[69], indicating the average oxidation state of MnOx post-heat-treatment may differ from the average oxidation state of the 10:90 films. Additionally, the slightly darker, more brown-black colour of the oven-dried films could be indicative of a greater portion of Mn_2O_3, compared to the reddish-brown hue visible in the 10:90 films indicating higher MnO_2 content[112]. This could explain the variation in the oxidation-wave shape observed between 200 °C oven-dried films and 10:90 films; varying ratios of the forms of MnOx present could exist depending on whether the active layer of film was heat-treated or not. This would result in different amounts of oxidation taking place for the two electrode types. Once readily-oxidizable MnOx is converted into a more oxidized form, it is

unavailable to be oxidized during the cycles that follow, resulting in an oxidation current that subsides rapidly at first as active sites are consumed and then approaches steady-state with cycling. It is currently difficult to distinguish between redeposition of dissolved Mn^{2+} or some other oxidation causing dissolution or irreversible film conversion, and likely some combination of these processes is happening in this system, coupled of course with CR effects. In the future, XPS analysis to determine the Mn oxidation state before and after electrochemical cycling in this window should be performed to evaluate any changes in film oxidation state.

Nonetheless, at the end of the 2000 cycles, the two MnOx conditions exhibit similar CV shapes, but with higher currents recorded for the 10:90 films attributed to their increased capacitance (Fig. 5.10a). Ultimately, this highlights that while the heat-treatment step employed in both methods ensures a film that can better withstand a more commercially desirable potential window; the double-deposition method offers greater capacitance and is thus more suited for a commercial device. Fig. 5.10b shows average CE as a function of cycle number for both film conditions. Both film types show excellent CEs, but require a few cycles to reach their maximum CE. Clearly, these films would need to be cycled to steady state prior to use in a commercial device to ensure their best performance.

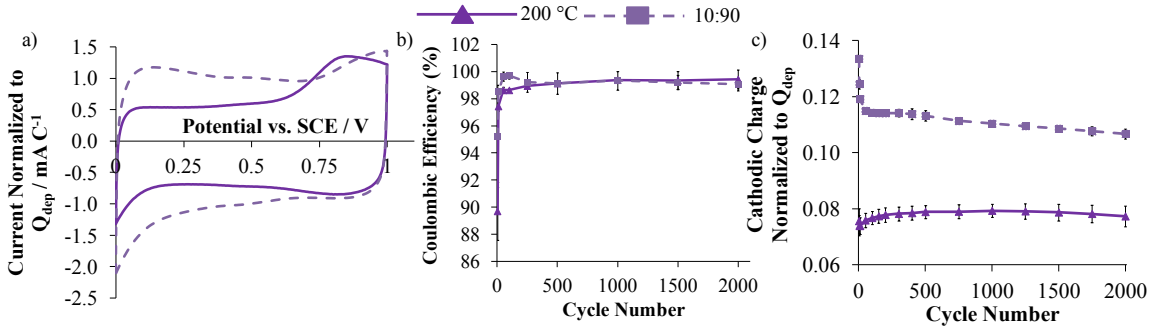

Figure 5.10. a) Representative final CV cycle, b) average CE with cycle number, and c) cathodic CV charge as a function of cycle number for 10:90 films (dashed line) and 200 °C oven-dried films (solid line) in the 0.0-1.0 V window.

Cycle life during CV was assessed in the extended potential window by integrating the cathodic charge during repetitive cycling (Fig. 5.10c). Cathodic charge was chosen because the reduction portion of the CV does not show as significant shape changes as the oxidation portion. As expected, the charge is much larger for the 10:90 films, consistent with their heightened charge storage capability due to their increased water content. Interestingly, the 10:90 films show a significant drop in charge with initial cycling, attributed to the decrease in reduction waves at 0.2 and 0.8 V. While charge loss is often attributed to electrode failure, considering the wave at 0.2 V is likely film dissolution, in this case charge loss is possibly just indicative of the film approaching steady state as the dissolution/redeposition mechanism slows. Likewise, the broad cathodic wave at 0.8 V is possibly decreasing as a result of the elimination of one form of the oxide as the film equilibrates. So, while these reactions diminish with cycling, it is hard to say whether the resulting decrease in charge is indicative of electrode failure. With cycling, even with the decrease in charge, it is clear 10:90 films still store significantly more energy than their anhydrous counterparts. However, the gradual charge decline observed as cycling continues suggests while electrodes made with 10:90 MnOx films show promising electrochemical properties, work still needs to be done to improve

the stability of this material in large potential windows before it can be applied to commercial ECs.

Remarkably, 200 °C oven-dried films show a slight increase in charge (Fig. 5.10c). Increases in charge/capacitance during initial cycling have been reported in the literature[21,22,25,109,114], though are not discussed in detail. Possibly, an oxidation is converting the film to a more capacitive form. Although fully heat-treated films show no considerable charge loss, the capacitance maintained by 10:90 films at steady state, even after a significant capacitance loss in the first 1000 cycles, still surpasses the capacitance of heat-treated films. Yet, if more cycles were run, as would be typically in a commercial EC, it is possible the charge stored on 10:90 films would eventually drop to below that of the 200 °C oven-dried films.

These findings suggest that cycling any device with MnOx-based electrodes to steady state before putting it on the market is critical to ensure consistent performance and also draw attention to the importance of evaluating long-term cycling performance. Since one of the key benefits that current commercially-available ECs offer is cycle lives that exceed those of other energy storage devices, and they are often expected to survive hundreds of thousands of cycles[2,5,10,11], it is important that any newly synthesized material offering enhanced capacitance is subjected to rigorous cycle-life tests. It is evident that while the double-deposition method offers a unique balance of hydration-assisted pseudocapacitive charge storage and heat-treatment-induced decreased resistance, like many other MnOx electrodes long-term cyclability issues are still a concern[20], as they are with anhydrous films as well (Fig. 5.9).

Figure 5.11a displays representative 2 mA GCD curves for a 10:90 and 200 °C oven-dried electrode. Matching what was observed with 0.4-0.8 V cycling, the 10:90 films exhibit larger charges, indicated by an increased charge time, highlighting their better ability to store charge pseudocapacitively and greater fraction of active film.

The Ragone plot (Fig. 5.11b) in the 0.0-1.0 V window mirrors the observations from the truncated potential window, but in this window 10:90 films in fact show significantly higher energies at all currents tested while still offering equally high powers as films fully dried at 200 °C. Interestingly, the 200 °C oven-dried films show a greater energy decline than their more hydrous counterparts as the current is increased past 7.5 mA. Fully heat-treated films exhibit an average energy loss nearing 48% upon increasing the current from 10 to 30 mA. In contrast, 10:90 films do not start to experience a considerable energy decline until the discharging current exceeds 11 mA, and display an average energy drop of approximately 35% when the current is increased from 10 to 30 mA. These results highlight that even in the more strenuous potential window of 0.0-1.0 V, 10:90 films display improved rate capability and energy density compared to their totally dehydrated analogues. Additionally, conservation of high powers at fast charging rates is possible as a result of the decreased resistance from an improved film-substrate contact accomplished through use of the double-deposition method.

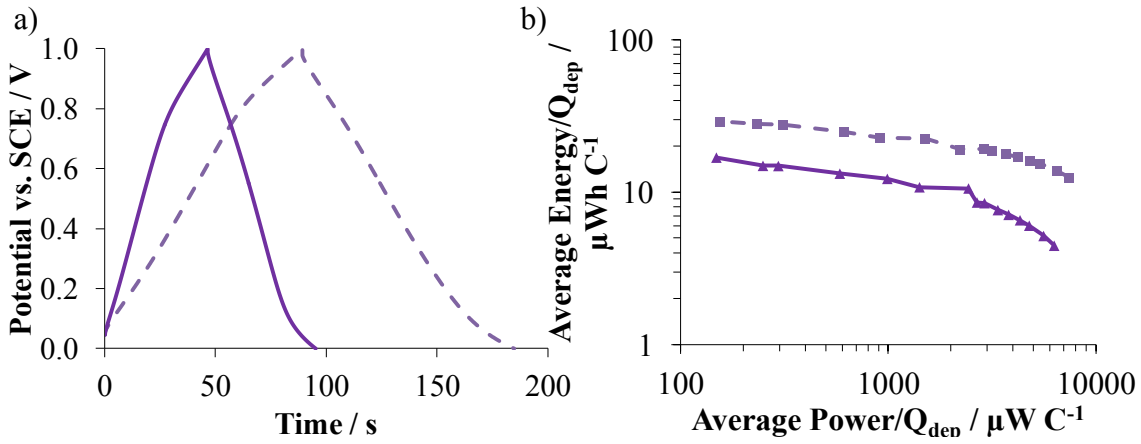

Figure 5.11. a) Representative 2 mA GCD curves in a 0.0-1.0 V window and b) Ragone plot constructed from average energies and powers for a 10:90 film (dashed line, squares) and 200 °C oven-dried film (solid line, triangles) collected at multiple currents in a 0.0-1.0 V window.

5.4.2 Self-Discharge on Manganese Oxide Electrodes

Conway and coworkers developed a method to identify mechanisms of self-discharge (SD) by plotting an electrode's open-circuit potential decay in various ways[37–39]. A diffusion-controlled process, resulting from a redox-active contaminant present at low concentrations in the electrolyte, presents as a linear potential loss when plotted vs. $t^{1/2}$ [37–39]. An activation-controlled Faradaic SD, such as SD arising from electrolyte decomposition or reaction of a species attached to the electrode surface, results in a potential that declines linearly with log(t)[37–39]. However, SD resulting from CR also results in a potential decay that is linear in log(t)[40]. Figure 5.12 displays a representative SD profile for a 10:90, 200 °C oven-dried, and wet MnOx film plotted vs. time, $t^{1/2}$, and log(t). The SD mechanism of MnOx has been previously proposed to be governed by the combination of an activation-controlled Faradaic reaction and CR[46]. The clearly non-linear response of potential vs. $t^{1/2}$ in all cases rules out a diffusion-controlled mechanism for all electrode types presented herein (Fig. 5.12b).

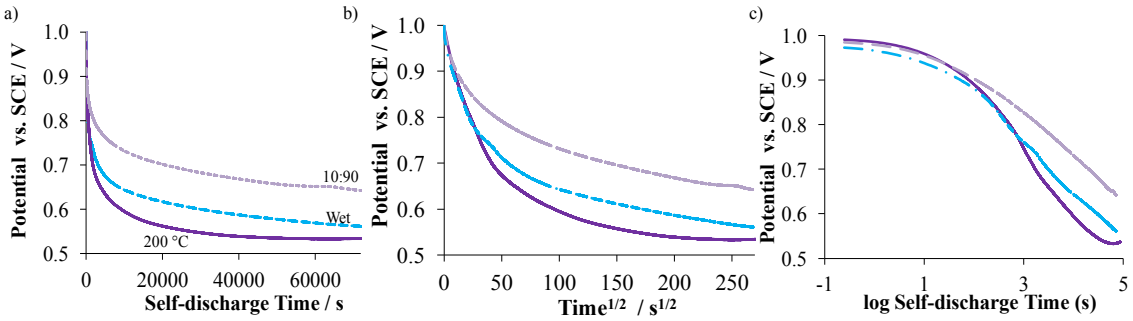

Figure 5.12. Representative potential vs. a) time, b) time$^{1/2}$ and c) log(time) for the SD of wet, 200 °C, and 10:90 films following charging to 1.0 V vs. SCE.

It is noteworthy that the 200 °C oven-dried films experience more severe potential loss than both their 10:90 and wet counterparts. Activation-controlled oxidation or CR due to ionic or electronic mobility limitations could explain this result; currently neither of these phenomena can be ruled out. Considering the first possibility, the rapid potential decline of 200 °C oven-dried films upon switching to open-circuit configuration can be explained by the activation-controlled SD reaction, an oxidation in this case, being facilitated on the dehydrated MnOx surface. The accelerated potential drop seen with the 200 °C oven-dried films is consistent with the greater oxidation evidenced by these electrodes at high potentials in both CV and GCD data.

Alternately, if CR is dominated by electronic conductivity, which is enhanced in heat-treated films[26,30,33], the accelerated potential drop experienced by 200 °C oven-dried films can be explained primarily by CR. Following charging, a potential gradient exists in the film with a region of positive charge near the surface, and a lower potential within the bulk (given the charge to 1.0 V used in this experiment). Charge can move within the film to eliminate this gradient more efficiently in fully-heat-treated MnOx as a result of its improved electronic conductivity[34,40], generating a faster potential decline. In this case, the positive charges added to the film are not consumed by a parasitic reaction, but rather

relocated to the depths of the film as the potential equilibrates. Likewise, the lower electronic conductivity of the hydrous films could result in decreased SD as a consequence of CR since the movement of charge is hindered in these films[26,33]. This means charges added to the electrode surface would take longer to redistribute towards the bulk in hydrous films, causing their potential decline due to CR to happen at a slower rate.

Likely, a combination of oxidation and CR is happening for all MnOx conditions under study. The difference in potential loss observed between 10:90 and wet films is currently unclear, but is likely related to the balance of ionic and electronic mobility within the 10:90 films. Ultimately, these results suggest electrodes made with 10:90 films would be more commercially desirable as their decreased degree of SD provides longer shelf lives for devices.

5.5 Conclusions

Implementing the double-deposition method, in which a base layer of MnOx film is deposited and heat-treated, and then a second layer of film is deposited prior to the entire electrode being stored wet, can generate films with the benefits of both anhydrous and hydrous MnOx. As long as the oven-dried portion of film is kept thin, this deposition method drastically decreases electrode resistance through improving electronic conductivity and offering a better connection between the MnOx film and the current collector, without sacrificing the high energies and capacitances achieved by maximizing film hydration. In addition, aging of double-deposition electrodes does not negatively affect film stability, and the smooth film surface achieved through depositing MnOx onto itself generates films that are less susceptible to cracking than their uneven singly-

deposited counterparts. These findings indicate that a combination of the advantages provided by heat-treated and hydrous films necessary to optimize EC electrode performance can be achieved through use of the double-deposition method.

Chapter 6 Carbon Oxidation and Charge Redistribution as Causes for rGO Self-Discharge Monitored by Float Current

6.1 Introduction

This chapter evaluates how redistribution of charge coupled with the degree of carbon oxidation influences the SD of reduced graphene oxide (rGO) electrodes by means of float current measurements. Float currents (I_f) are the currents required to keep an electrode at a desired potential; they are often considered equal to the SD current[39]. For instance, if at a certain hold potential a Faradaic reaction causes electrons to enter the carbon, positive current is needed to cancel these electrons in order to maintain the desired potential. Herein, how CR effects resulting from the cycling method used to oxidize rGO impact the recorded I_fs is also discussed. Comparison of I_fs collected with oxidized negative-sweep (Ox-NS) rGO and oxidized positive-sweep (Ox-PS) rGO offer evidence that the cycling method employed is not only oxidizing the carbon, but is also creating differing potential gradients within the rGO that alter the CR. This draws attention to the importance of giving consideration to CR effects for anyone comparing SD of materials in the literature where slight differences in charging procedures might significantly impact the observed SD.

A variety of holding potentials is investigated to offer insight into what potentials result in positive I_fs to counter SD and to evaluate the effect of charging time, which impacts CR. This is because a longer charging time allows charges to move deeper into the carbon's pores. Finally, a transmission line circuit based on de Levie's model[50] is used as a model pore to simulate the I_f if CR was the only process responsible for SD.

These results are subsequently compared to what is evidenced by unoxidized carbon, where both CR and some oxidation are expected to take place.

In addition, unoxidized rGO is stepped to below its OCP prior to charging to bring out CR effects in the material. Conway[38,39] shows a positive step to a positive polarization potential essentially always generates a positive I_f, making it difficult to distinguish if the initial positive I_f is the outcome of CR into the bulk material or carbon oxidation for unoxidized rGO. However, a rapid initial discharge (or negative polarization) is capable of bringing out CR effects if they exist, but would have no influence on I_f in a system where CR does not occur; Graydon and coworkers have implemented this method to elucidate CR in open-circuit SD measurements[45].

6.2 Oxidation of rGO via Cyclic Voltammetry

Figure 6.1 displays representative CVs of rGO, drawing attention to the changes in the CV shape that arise with cycling. To address discrepancies in current magnitudes arising from inconsistent packing within the microcavity electrode, all CV currents are reported normalized to the anodic current recorded at 0.3 V ($I_{a,\ 0.3\ V}$) in the final CV cycle. Broad quinone-hydroquinone[38,78,79,120–125] peaks develop in the region of 0.4-0.65 V and grow with cycling. Quinone signal growth happens rapidly at first, but the growth rate diminishes considerably after approximately 2000 cycles, consistent with the elimination of available surface sites for quinone formation[36]. 5500 cycles are required for quinone peaks to reach steady state whereupon the carbon is considered to be fully oxidized to the extent achievable through 100 mV s^{-1} CV cycling, although it is recognized that regions deep within the pores of the rGO may not experience significant potential changes with this sweep rate to be oxidized with this method.

As these features develop, a dramatic decrease in the oxidation wave at 0.6 V is evident with each consecutive cycle, indicative of some limitation to the rate of the reaction responsible for the wave. In general, the concentration of active oxidation sites on the carbon controls the rate of oxidation (*e.g.* formation of surface oxides like quinones or gaseous products such as CO_2), thus the diminishing oxidation wave is the consequence of active sites being consumed[36,80,122,126]. As these sites are depleted, less oxidation can occur and the oxidation wave subsides.

An isopotential[127,128], evidenced as a potential at which the same current is recorded, independent of cycle number, is present at 0.75-0.8 V for rGO (Fig. 6.1). An isopotential is suggestive of two reactions happening in unison, one of which results in an adsorbed or deposited species[127,128]. This feature has been observed with other carbons cycled in a similar fashion[36]. Based on previous data collected in this lab as well as data from literature reports, the formation of CO_2 and oxygen-containing surface functionalities during carbon oxidation are responsible for this isopotential[36,38,79,80,122,126,129,130]. The diminishing oxidation wave coupled with the development of quinone peaks and evidence for the generation of some surface species confirm the CV cycling is effectively oxidizing rGO.

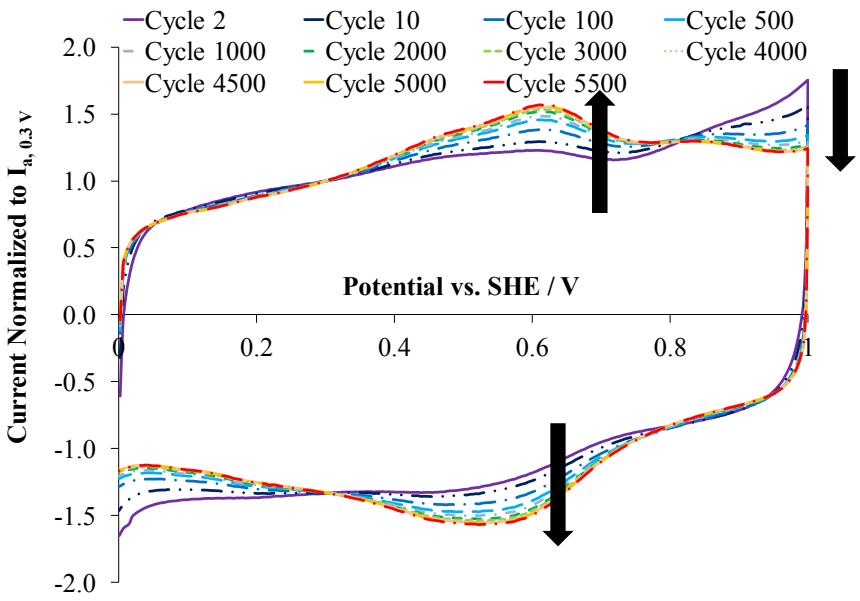

Figure 6.1. Representative CV cycles of rGO showing growth of the quinone-hydroquinone functionality and a decrease in oxidation wave with continuous cycling.

6.3 Influence of Degree of Oxidation and Cycling Method on the Float Current Response of rGO

As confirmed by the CV oxidation wave (Fig. 6.1), potentials of 0.7 V are sufficient to promote rGO oxidation. Representative I_fs recorded at various potentials are displayed in Figure 6.2, with insets showing the I_fs at short times. When comparing unoxidized (UnOx) to oxidized (Ox-PS) rGO, UnOx rGO consistently shows greater positive I_fs for the duration of the hold at 1.0 V (Fig. 6.2a) and a slower current decay compared to its Ox-PS counterparts. A positive I_f offsets the electrons released during carbon oxidation and/or maintains the desired potential at the pore mouths as charges accumulated near the pore orifices redistribute towards the pore bases.

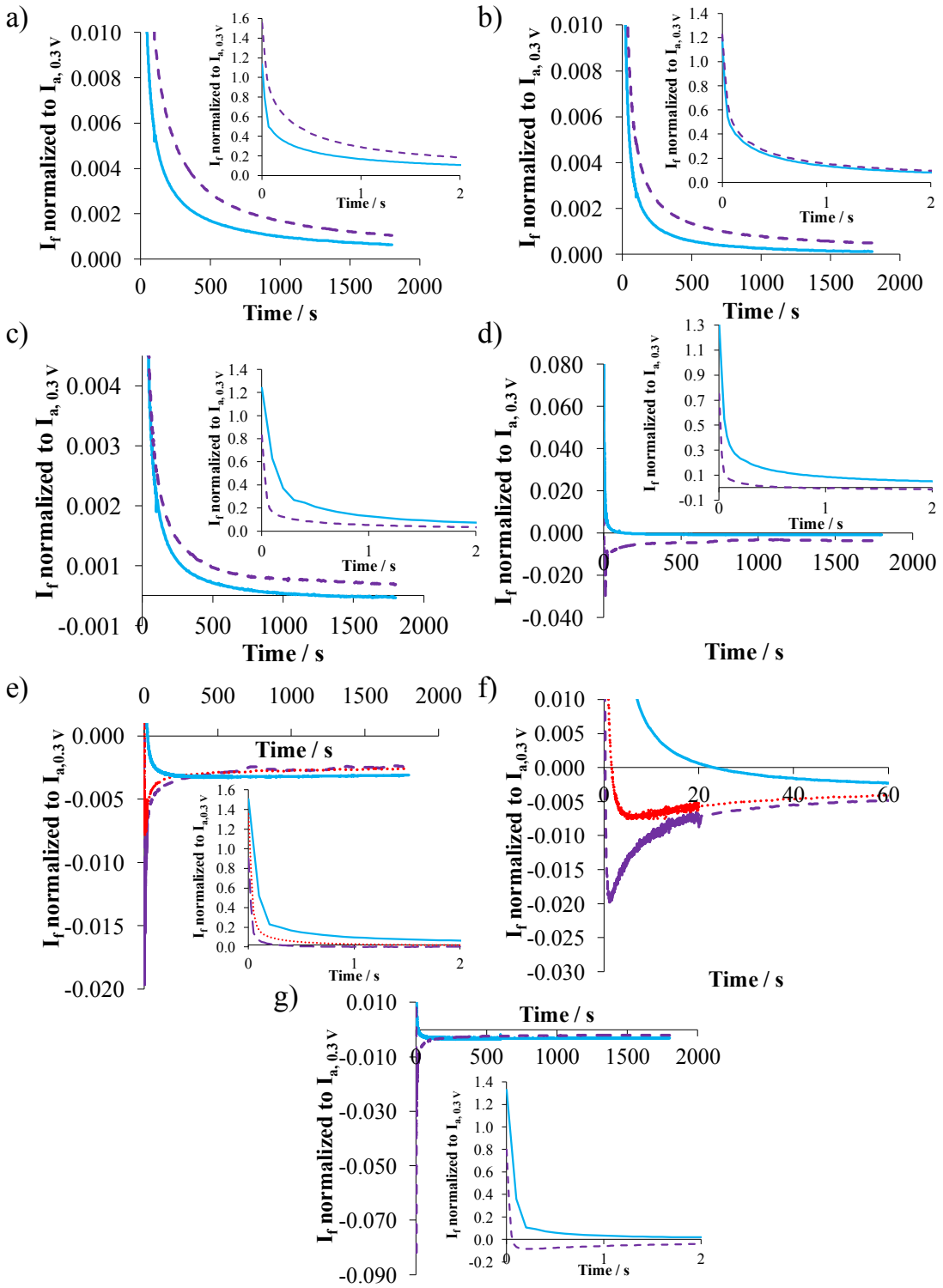

Figure 6.2. I_fs for representative UnOx and oxidized rGO at 1.0 V (a), 0.9 V (b), 0.8 V (c), 0.7 V (d), 0.6 V (e-f), and 0.55 V (g). Insets show initial I_fs at short times. UnOx rGO is shown in purple dashed lines, Ox-PS rGO is shown in blue solid lines, and Ox-NS rGO is shown in red dotted lines.

Although an initial high I_f that decays gradually with time is expected for charging of the double layer, normalization of the data should make up for any differences in double-layer charge storage as a result of packing or wettability variance between the carbon types; any current brought on by double-layer charging should be similar between the carbons. Thus, the elevated I_fs and slower I_f decay rate of UnOx rGO at 1.0 V (Fig. 6.2a) can be explained by the abundance of possible oxidation sites present on this material initially, allowing significant oxidation to occur at the onset of the hold and adding to the I_f resulting from charging the double layer. As the active sites are consumed, the oxidation slows down, and the I_f decreases. It is unlikely oxidation contributes significantly to the I_f of Ox-PS carbon. While it is possible oxidation deep within the pores of rGO at sites inaccessible with CV cycling could induce a positive I_f, this is not likely the case here. It would take some time for charges to move deep enough to access remaining active sites in the carbon. Since the I_f of Ox-PS rGO continues to decrease until it reaches steady state, and open-circuit SD data (discussed in Chapter 7) indicate ~10000 seconds is required for charges to move to depths greater than what was accessible with CV cycling, it is unlikely the 30 minute hold at 1.0 V is causing significant oxidation at locations inaccessible with CV cycling.

At 0.9 V, Ox-PS and UnOx carbons show preliminary I_fs that are identical in magnitude (inset Fig. 6.2b). This is unexpected since UnOx carbon should be undergoing significantly more oxidation, and should therefore require more positive current than its Ox-PS analogue to offset this reaction. As previously mentioned, since the I_fs are normalized, any variation in double layer size can be ignored. If carbon oxidation was the only other source for I_f, UnOx rGO should exhibit I_fs that surpass those of Ox-PS carbon,

especially at the onset of the hold when UnOx rGO has the highest concentration of active sites. This implies CR effects also contribute to I_f, likely more so for the initial I_f of Ox-PS rGO as a result of the potential gradient in its pores post-cycling. Immediately prior to the I_f charging step, Ox-PS rGO experiences a CV sweep down to 0.0 V, during which much of the charge near the surface of the Ox-PS carbon is removed. This charge needs to be replaced to maintain a potential of 1.0 V, meaning some of the I_f recorded for Ox-PS carbon is likely to restore the charge removed during the sweep to 0 V. Nevertheless, the I_f of Ox-PS carbon quickly drops below that of UnOx rGO, consistent with no significant oxidation taking place on Ox-PS carbon and charges removed during cycling being replaced rapidly.

CR's contribution to the I_f profile of Ox-PS rGO becomes more clear when considering the I_fs recorded at 0.8 V (Fig. 6.2c). CV data confirms 0.8 V is sufficient to promote oxidation. Yet, Ox-PS carbons, which have essentially no active sites on their surface, exhibit initial I_fs that surpass those of their UnOx counterparts, which are susceptible to oxidation (Fig. 6.2c inset). Thus, the only plausible cause for this trend is CR. When the potential is first applied to Ox-PS rGO, similar to the hold at 0.9 V, CR effects cause high initial I_fs for the Ox-PS rGO, which were previously cycled to 0.0 V. However, at 0.8 V, unlike at the higher potentials, less energy is supplied to drive the oxidation, so less oxidation occurs for UnOx rGO. This allows the initial current required to replace the charge removed from Ox-PS carbon during cycling to overcome the current countering UnOx rGO oxidizing.

I_fs collected at 0.7 V mirror what was observed at 0.8 V (Fig. 6.2d), with the I_f of Ox-PS carbon surpassing that of UnOx carbon. Interestingly, UnOx rGO displays a dip in

its current vs. time profile at this potential; the I_f starts positive, rapidly switches to a negative value, and then remains negative while decreasing in magnitude for the duration of the hold. This feature also suggests CR plays a role in the I_f response of rGO. Before charging, the rGO has an OCP greater than 0.7 V. During charging, the UnOx rGO is first stepped down to and charged from 0.5 V, which removes some charge from its pores (Fig. 6.3a). Then, the positive I_f at the beginning of the experiment likely serves to replace charge removed from UnOx rGO during the step down and charging (Fig. 6.3b). The following spike of negative current flows to maintain the 0.7 V potential, likely by cancelling positive charge that moves from the base of the pores (which would be at OCP, > 0.7 V) to the surface, as illustrated in Fig. 6.3c. Gradually, the potential gradient through the material decreases, and the overall potential within the pore lowers, necessitating the smaller I_f to keep the potential at 0.7 V. Additionally, the time-delay before the dip is observed points towards CR as its cause; time is required for charge to move through a material.

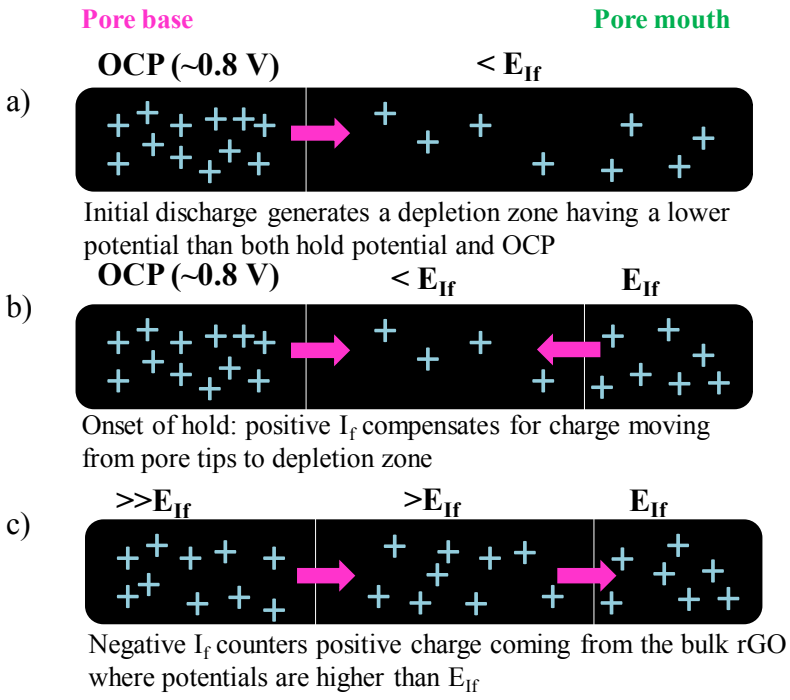

Figure 6.3. Illustration of movement of charge throughout the I_f experiment. CR during the step down and charge, the onset of the hold, and during the middle and end of the hold are shown in panels a), b), and c), respectively. E_{If} represents the holding potential.

No I_f dip is observed for Ox-PS carbon. This is likely because these carbons spent considerable time cycling through lower potentials (down to 0 V) compared to their UnOx analogues. Consequently, they have a larger zone where the potential is below 0.7 V, so more positive charge needs to be replaced to maintain a potential of 0.7 V. Positive charges approaching the surface of Ox-PS come from greater pore depths and therefore have more time to spread out and take longer to reach the surface.

Undoubtedly, CR effects influence the I_fs recorded for the material under study. To test if the sweep down to 0.0 V truly impacts the I_f observed for Ox-PS rGO, it was compared to Ox-NS rGO, which was swept from 1.0 to 0.5 V (Experimental) prior to a 0.6 V hold. This means substantially more positive charge is present near the surface of Ox-NS rGO than Ox-PS rGO. Nonetheless, the sweep down to 0.5 V will still deplete

more positive charge from Ox-NS rGO than the rapid step to 0.5 V employed with UnOx carbon.

With 0.6 V holds (Fig. 6.2e), the initial I_f magnitudes are in agreement with the amount of charge at/near the surface that would need to be replaced. Ox-PS rGO shows the highest initial I_f (Fig. 6.2e inset), consistent with this carbon having the least amount of positive charge near its surface at the onset of the hold. Ox-NS carbon presents the next highest initial I_f, and UnOx rGO shows the smallest I_f magnitude as a consequence of having the most charge remaining near its surface since it was only subjected to a rapid step down to 0.5 V before charging. Furthermore, Ox-NS carbon shows a dip in its I_f profile (Fig. 6.2f), albeit less severe than that of its UnOx analogues. Again, this feature likely corresponds to the cancellation of positive charge coming to the surface; Ox-NS rGO has some charge near its surface from being exposed to 1 V prior to charging, although less positive charge than UnOx rGO. Thus, less negative I_f is expected for Ox-NS rGO than its UnOx analogue. This trend strongly suggests CR has a significant contribution to I_fs recorded at the beginning of the hold, independent of the degree of carbon oxidation.

The likelihood of CR being responsible for the dip becomes even more apparent when comparing the dips observed at different potentials. For UnOx carbon, dips appear earlier during the hold at lower holding potentials (Fig. 6.4). Throughout the charging, positive charges are removed from the surface (when charging to below OCP), and with an identical ramp rate and initial potential, charging to a higher potential takes more time than charging to a lower potential. This means that when carbon is charged from 0.5 V to 0.7 V, rather than to 0.6 V, positive charges are removed from greater pore depths,

meaning the remaining positive charges travel a longer distance to reach the pore tips and the influx of negative current required to cancel them is seen later in the experiment, as depicted in Figure 6.5. Data collected at 0.55 V (Fig. 6.2g) and with a model pore (discussed below) are in agreement with this trend.

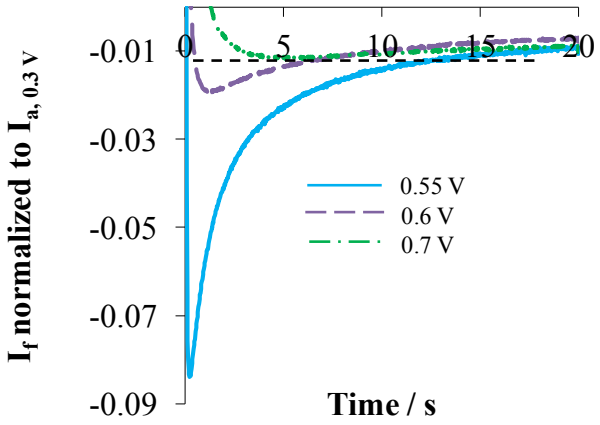

Figure 6.4. Representative I_f dips for UnOx rGO held at various potentials showing dips occurring later in the hold at higher potentials. The black dashed line serves to guide the eye in locating the shallow dip recorded at 0.7 V.

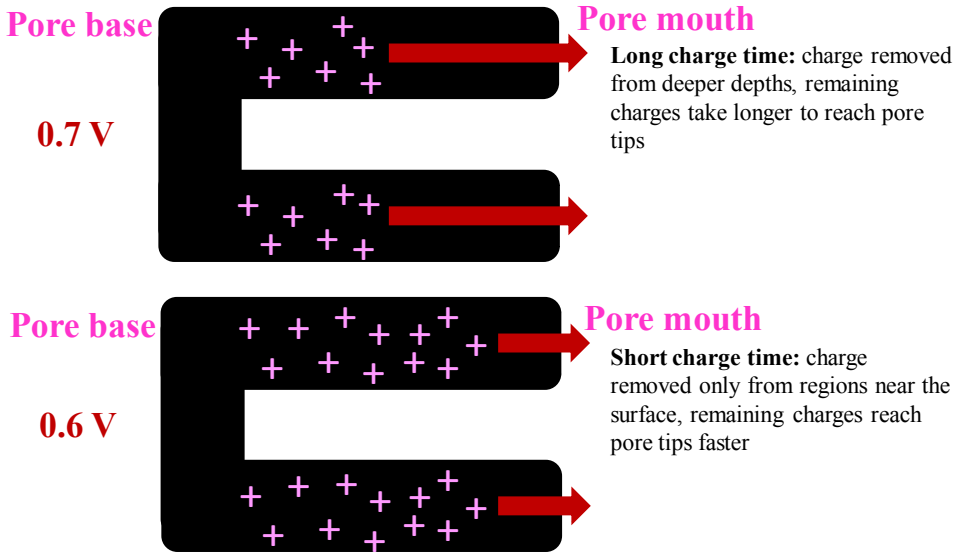

Figure 6.5. Illustration depicting why a dip in I_f as a result of cancelling CR up from the pore base when an electrode is charged to a potential below its OCP would take less time to appear when the electrode is charged to a lower potential following stepping down to 0.5 V.

At potentials of 0.6 V and 0.55 V, all carbons reach steady state with negative currents, indicating either some Faradaic reduction is occurring at this potential or depletion of positive charges approaching the surface from deeper in the electrode continues for the entire duration of the hold. Since the steady-state currents of both Ox-PS and UnOx rGO show some overlap, Faradaic reduction can be ruled out as the primary contributor to the steady-state current. CV data shows no reduction wave at 0.55 or 0.6 V other than the broad pseudocapacitive quinone peak[38,78,79,120–125], suggesting Ox-PS electrodes should show a larger reduction current since they possess more quinone groups. Therefore, it is likely the negative I_fs at these potentials are the consequence of the CR continuing to bring positive charge to the surface that needs to be removed to maintain the low potential. The negative I_f serves to gradually negatively charge the bulk carbon whose OCP is greater than 0.6 V.

The results discussed above indicate both CR and carbon oxidation play a role in discharging rGO's surface and reveal any variation in the method of charging an electrode can drastically impact I_f measurements as a consequence of CR. It is also evident certain I_f profile features cannot be separated into the outcome of CR or the outcome of oxidation by this experiment alone, such as the I_f response of UnOx rGO at high potentials which could be the result of either significant oxidation, CR, or both. This is because the carbon should lose potential not only from electrons entering as a result of oxidation, but also as a result of charges moving away from the pore mouths to the depths of the rGO where the potential is lower. Therefore, a transmission line circuit used to model a pore was studied to evaluate what the I_f response would resemble if CR was the only factor causing charge loss from the surface.

6.4 Simulated Float Currents with Charge Redistribution Effects Only

A model pore simulated by a transmission line circuit composed of eight capacitors and resistors in series (modeled after de Levie[50], Experimental) was subjected to an identical charging and holding procedure as the rGO. This was to test the validity of the theories proposed above regarding how CR influences the I_f profile of rGO. Prior to the I_f experiment, all eight capacitors were charged to 0.8 V. This simulated a uniform open-circuit voltage (OCV) throughout a pore, near the OCP recorded for rGO in the microcavity electrodes.

Consistent with rGO, holding voltages further from the pore's simulated OCV result in higher magnitude I_fs, and the I_fs fall with time (Fig. 6.6). In addition, a dip in the I_f recorded for the model pore is observed at 0.6 V suggesting CR effects alone are likely responsible for the dips in the I_f profiles of rGO.

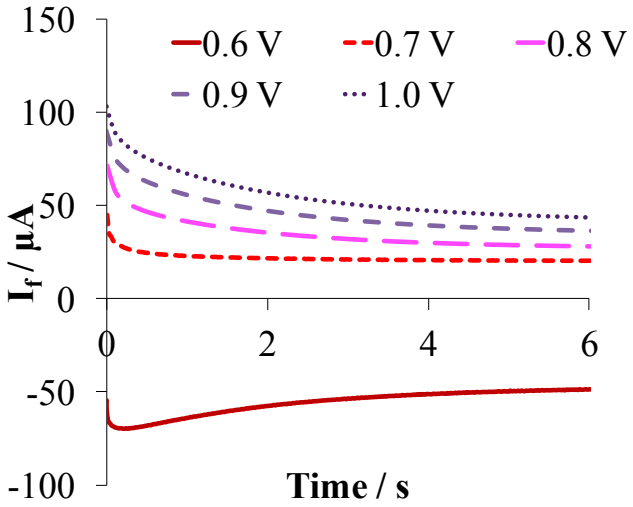

Figure 6.6. I_fs recorded for a model pore.

Immediately after charging, capacitors deep within the circuit (*e.g.* Capacitors 7 and 8) remain near the circuit's simulated OCV of 0.8 V (Fig. 6.7a), mimicking the predicted response of the pore base in rGO where the high pore resistance would prevent the charging from reaching all the way down the pores. Subsequently, charge from

Capacitor 8 (*i.e.* the pore base) will redistribute up towards Capacitor 1 (the pore mouth), lowering the voltage at the pore base and meriting the flow of negative current to eliminate these positive charges (Fig. 6.7a). With time, the voltage gradient within the pore decreases and the entire pore approaches the hold voltage, reducing the magnitude of the recorded I_f.

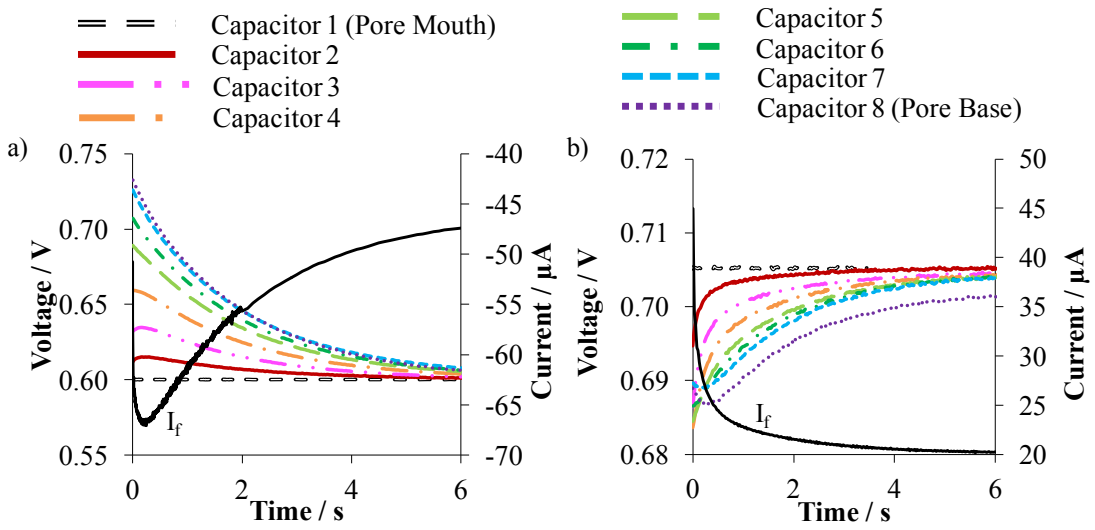

Figure 6.7. Voltages on Capacitors 1-8 in a transmission line hardware circuit modeling voltage changes in the pores of rGO with a hold at a) 0.6 V and b) 0.7 V following 100 mV s^{-1} charging, mirroring the experiment conducted on UnOx rGO. The corresponding I_f is displayed in a black solid line and labeled.

At 0.6 V, the voltages of Capacitors 2 and 3 briefly rise, while the potentials on Capacitors 4-8 fall (Fig. 6.7a), explaining the dip in the I_f profile. Charge leaves regions near the pore base (*e.g.* Capacitors 7 and 8) and approaches the pore mouth (Capacitor 1) to reduce the voltage gradient within the model pore. An increase in current magnitude (or current dip) is required early in the experiment to eliminate the positive charge that comes to the surface from the depths of the pore, as depicted in Fig. 6.3c. As more charges are eliminated, the voltage gradient within the pore decreases, the remaining charge spreads out, and less negative current is needed to maintain a 0.6 V voltage (Fig.

6.7a). Since a negative I_f is needed to maintain a positive voltage at the pore mouth, and parasitic Faradaic reactions are not a possibility, the transmission line model shows that the I_f dip for rGO is consistent with charge redistributing within the material.

Capacitors deeper in the circuit (Capacitors 6, 7, and 8) reach a lower voltage when charged to 0.7 V compared to when charged to 0.6 V (Fig. 6.7); this is consistent with a longer charge time accessing and removing charge from surface area deeper in the pore (Fig. 6.5). Recall, a negative charge is being performed in this scenario, since the voltages on all capacitors are lower than the simulated OCV. These results support the theory illustrated in Fig. 6.5 explaining why the I_f dips appear later in the experiment when the rGO is charged for a longer time (Fig. 6.4); the increased charge time results in charge being removed from greater pore depths.

Fig. 6.7b shows that for a 0.7 V hold, the I_f is positive, even though the hold voltage is below the OCV of the model pore. rGO data from UnOx, Ox-NS, and Ox-PS carbons similarly show positive currents initially (Fig. 6.2). It is evident from model pore data (Fig. 6.7b) the positive I_fs serve to replace the charge removed during the initial discharge and charging from 0.5 V, as illustrated in Fig. 6.3b. These results support the theory proposed to explain why potentials of 0.6 and 0.55 V, which are too low to promote oxidation, result in positive I_fs initially for all carbons in this study (Fig. 6.2). Then, as the charges removed from regions near the pore mouth are replaced, the I_f rapidly switches to negative for rGO at 0.7 V to cancel the charge approaching the surface from the depths of the pore.

Contrary to rGO data, the I_f of the model pore at 0.7 V remains positive throughout the hold and shows no clear dip. This is likely the outcome of the decreased

resistance of the model pore compared to rGO. The resistance of the pores of activated carbon was determined to be more than 10 times greater[45] than the resistance used in the transmission line circuit studied herein, and it is likely the resistance within the pores of rGO is on a similar scale. Following the step down to 0.5 V and charge to 0.7 V, the voltage at the model pore base (Capacitor 8) is below 0.7 V (Fig. 6.7b), and a positive current is required to raise the voltage of the entire pore to 0.7 V. For pores in rGO, which would have much higher resistance, the 100 mV s^{-1} charge to 0.7 V is likely insufficient to alter the potential at the base of the pore; the pore base remains at OCP (~0.8 V). With time, charges from these depths approach the surface, necessitating the eventual flow of negative current to cancel these charges and maintain a potential below OCP at the carbon surface. Essentially, the depletion zone created during the initial discharge extends the length of the model pore (at 0.7 V), whereas in rGO the depletion zone would remain near the pore mouths and the potential at the pore bases would likely not be affected significantly.

Nonetheless, this model pore confirms CR can generate a dip in the I_f profile. Additionally, the simulated pore shows a negative I_f is recorded if the voltage applied is lower than the voltage of the bulk material (Fig. 6.7a), and shows a positive I_f is recorded when regions near the pore mouth are below the desired voltage (Fig. 6.7b). These data support the proposed theory for the current dips observed within the profiles of UnOx and Ox-NS rGO, and the negative I_fs recorded at potentials below the OCP of UnOx rGO; the negative I_fs likely serve to continue lowering the potential deep within the pores of the carbon.

6.5 Conclusions

rGO can be significantly oxidized through cycling in acid, confirmed by the development of reversible quinone/hydroquinone peaks. I_fs confirmed a relationship between the degree of rGO oxidation and the extent of SD. At high positive potentials, unoxidized rGO displays steady-state I_fs that are consistently higher in magnitude than oxidized rGO, congruous with oxidation occurring to a greater extent with unoxidized carbon, thereby identifying carbon oxidation as a cause of SD for this material. SD of carbon EC materials is generally more severe if the carbon is abundant with oxygen-containing surface functionalities[7,52–54]. This is likely because these groups are oxidizing and causing electrons to enter the carbon similar to the SD described for carbon cloth in the literature[36]. However, the data reported herein confirm oxidation is not the only contributor to rGO SD in aqueous electrolyte.

It is evident another mechanism is influencing the I_f response of rGO since oxidized rGO shows higher positive I_fs initially than unoxidized rGO at potentials of 0.8 V and below. Since these carbons were significantly oxidized beforehand, confirmed by the steady-state CV quinone/hydroquinone peak size[38,78,79,120–125], positive I_fs exceeding those of unoxidized rGO cannot be explained by oxidation. These results highlight CR, likely due to the need to replace the charge removed from these carbons during cycling to 0 V, as an important factor contributing to the SD of oxidized rGO. Differences in the I_fs recorded for equally-oxidized rGO cycled up from 0 V vs. down from 1.0 V prior to initiating charging confirm rGO is very susceptible to CR effects and slight variations in charging method can result in different potential gradients, and therefore different CR effects, within the carbon. This is an important consideration for

any group attempting to compare across literature results where different charging methods were employed, or anyone wishing to perform other electrochemical techniques prior to measuring SD in rGO.

Current dips, or rapid switches from positive to negative current, followed by a decrease in magnitude of negative current, are observed in the I_f profiles of unoxidized rGO, and oxidized rGO if it is cycled through high potentials immediately before charging to the hold potential, as well as a model pore. However, these dips are absent from the current profiles of oxidized carbons that were cycled down to 0 V prior to the I_f experiment, also highlighting the significant impact CR has on I_fs. The key difference that distinguishes the oxidized carbon cycled through low potentials before charging from the other carbons is that a large amount of charge was removed from this carbon prior to starting the I_f measurement. This suggests the dip in current is an outcome of CR, where the spike of negative current witnessed for oxidized negative-sweep and unoxidized rGO, as well as the model pore, is necessary to negate excess positive charge approaching the pore tips from deeper within the rGO's pores.

Furthermore, oxidized carbons exhibit negative I_fs at low potentials on par with unoxidized rGO, which has significantly less quinone functionality, arguing against quinone reduction as the cause of the negative I_fs and leaving CR as the most plausible explanation for rGO SD from potentials below its OCP. Results collected from this experiment prompted the SD experiments discussed in Chapter 7, where the SD of unoxidized and oxidized rGO is investigated with and without controlling charge redistribution within the carbon, and using OCP measurements with which mechanistic information about SD can be obtained.

Chapter 7 Separation of Carbon Oxidation and Charge Redistribution as Causes for Self-Discharge in rGO

7.1 Introduction

Self-discharge (SD) is a spontaneous potential loss that occurs when a device is left in open-circuit configuration, which drastically lowers device performance and reliability. Since many applications of ECs rely on the device being able to supply lots of charge quickly in a time of need, even after considerable time spent resting idle, minimizing SD is crucial. An abundance of literature reports note SD of carbon-based ECs is typically enhanced with the presence of surface heteroatoms[7,51–54]. For carbon-cloth electrodes, carbon oxidation has been identified as a cause of SD, and oxidized carbons have displayed less SD than their unoxidized counterparts[36]. This is because at the positive potentials carbon electrodes reach in most EC applications, oxygen-containing surface functionalities oxidize and electrons lost from the functional groups enter the carbon, discharging the electrode[36]; since these functional groups are affixed to the electrode surface, this process is activation-controlled.

However, in many of the high-surface-area carbons currently under investigation, the effect of charge redistribution (CR), the spontaneous movement of charge that arises when a potential gradient exists within an electrode, also has a significant influence on SD[40–47]. Subramanian and coworkers have recently evaluated SD in rGO supercapacitors, and found a combination of CR and ohmic leakage to be the mechanism[47]. Their work encompassed testing full cells with organic electrolyte[47]. In this work, aqueous electrolyte and a three-electrode half-cell setup are used. The half-cell setup allows for the elimination of ohmic leakage concerns while focusing on the SD of just one electrode,

rather than the full cell, which cannot separate how the positive and negative electrode individually contribute to SD. Aqueous electrolytes are deemed more environmentally friendly than organic electrolytes, owing to the toxicity and flammable nature of organic electrolytes[56]. Moreover, aqueous electrolytes can offer enhanced capacitance as a result of their smaller ion size[57], impart higher conductivity[131], and in the case of this work allow for investigation of how carbon oxidation, which is known to influence SD in other carbons[36], plays a role in rGO SD.

While progress has been made identifying SD mechanisms, challenges still lie in the separation of CR vs. activation-controlled Faradaic SD in high-surface-area carbons, where both phenomena are known and expected to occur. This is because CR and activation-controlled mechanisms can result in similar SD profiles, *i.e.* a linear potential drop vs. log(t) following a potential plateau[37–40]. In addition, both phenomena result in similar changes in SD profiles with multiple charge/SD cycles, for example slower potential declines and less overall charge loss with each consecutive cycle[36,46]. In this chapter, the SD of rGO resulting from CR and from activation-controlled carbon oxidation are evaluated for the first time as separate mechanisms, and their effects on the SD profile of rGO are distinguished. rGO was chosen as it is a promising EC material owing to its high surface area and conductivity[15,55], but its oxygen-containing functional groups and pores mean it is likely that carbon oxidation and CR play a role in its SD. This makes rGO a good candidate for testing if these two phenomena can be distinguished.

The work discussed in this chapter is pivotal in understanding and reducing EC SD, which can improve device performance, because it provides a method to identify

which process, CR or carbon oxidation, is the dominant contributor to SD in a system. The method could easily be applied to other porous carbons where CR and oxidation will likely both occur. Upon identifying the dominant cause for SD in a system, an appropriate method of SD prevention can be developed to optimize EC performance and reliability.

Four rGO conditions were studied: oxidized, unoxidized, oxidized CR-reset, and unoxidized CR-reset, using glassy carbon electrodes drop-coated with rGO suspensions made from sonicating rGO in EtOH (Experimental). The carbons underwent four charge/SD cycles to investigate the effect of the electrode becoming more fully charged with each cycle, in the case of non-CR-reset carbons, and the effect of the carbon becoming more oxidized with each cycle, in the case of unoxidized carbons. The similarities and differences among the various carbon conditions are compared and contrasted, allowing for a SD mechanism for rGO to be proposed and the outcome of oxidation and CR to be evaluated individually. In addition, the effect of the sonication step employed to create rGO-EtOH suspensions is briefly discussed through analysis of XPS data.

7.2 Effect of Sonication on rGO

Since ultrasonication has been shown to alter carbon surface oxides[91,132], the effect of sonication on the rGO samples was investigated via XPS. Analysis of the survey scan data for rGO samples (Table 10) shows sonication slightly reduces the carbon surface under study, indicated by the decrease in relative percent oxygen as sonication time is increased. Fitting of the C_{1s} spectra (Fig. 7.1, Table 10) cannot statistically indicate which, if any, surface functional groups are selectively reduced since the relative

percentages of the various groups remain the same within error. Given that occasional resonication was required to resuspend the rGO in EtOH, which could result in an inconsistent degree of reduction for rGO, unoxidized electrodes were all made from rGO-EtOH suspensions that were sonicated for 15 minutes total, allowing any effect of sonication to be neglected in the data analysis. The 5500 CV cycles employed to oxidize rGO would overcome any discrepancies in rGO oxidation as a result of variation in sonication time for oxidized rGO.

Table 10. Relative percentages of oxygen and carbon present on rGO sample surfaces as detected via XPS survey scan and percent concentrations of surface groups as determined by fitting of the C_{1s} spectra with errors representing one standard deviation determined by Monte Carlo simulations.

Survey Scan					
rGO Sample	C_{1s} (%)	O_{1s} (%)			
As-received	91.6 ± 0.7	8 ± 1			
3 x 5 min Sonicated	93.6 ± 0.6	6.4 ± 0.9			
7 x 5 min Sonicated	95.2 ± 0.6	4.8 ± 1			
C_{1s} Spectra					
rGO Sample	C=C (%)	C-O (%)	C=O (%)	COOR (%)	π –π* (%)
As-received	56 ± 2	21 ± 2	8.4 ± 0.7	4.7 ± 0.9	10 ± 1
3 x 5 min Sonicated	57± 1	21 ± 1	8.0 ± 0.7	3.9 ± 0.8	10 ± 1
7 x 5 min Sonicated	57 ± 1	21 ± 1	7.9 ± 0.6	3.8 ± 0.9	10 ± 1

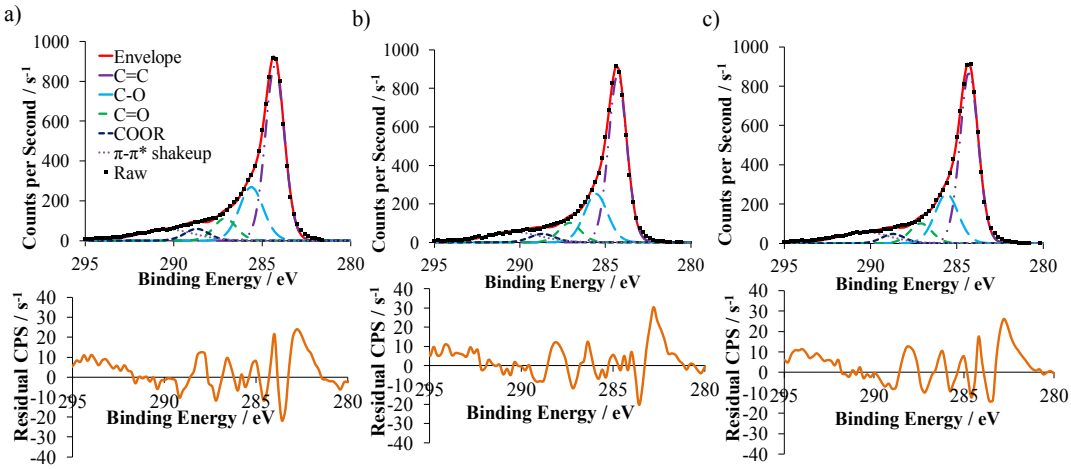

Figure 7.1. Background-subtracted C_{1s} spectra showing fit and peaks used to fit the data and the residual (in orange below) for a) as-received rGO, b) rGO sonicated for 15 minutes total, and c) rGO sonicated for 35 minutes total.

7.3 Effects of Carbon Oxidation and Charge Redistribution on rGO Self-Discharge during Open-Circuit Potential Measurements

7.3.1 Oxidation of rGO via Cyclic Voltammetry

To evaluate the influence carbon oxidation has on rGO SD, the SD profile of carbons that were oxidized prior to starting SD experiments, and thus are unable to lose significant charge as a result of oxidation, are compared to unoxidized carbons, which are susceptible to oxidation. Oxidation of rGO on GC electrodes was achieved though the same cycling procedure applied to the rGO microcavity electrodes in Chapter 6: 5500 CV cycles in a 0.0-1.0 V window at 100 mV s^{-1} in 1 M H_2SO_4. With cycling in this range, the rGO develops clear, reversible quinone peaks[38,78,79,120–125] between 0.4 and 0.65 V (Fig. 7.2) that grow initially and then come to steady state while the oxidation wave at high potentials diminishes with time, in agreement with microcavity data (Chapter 6).

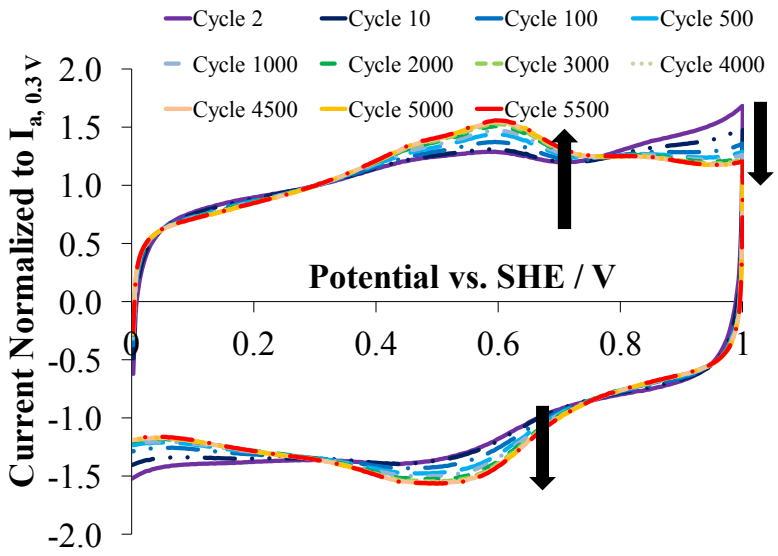

Figure 7.2. Representative CVs of rGO on GC showing the growth of quinone peaks with cycling.

7.3.2 Open-Circuit Self-Discharge Measurements of rGO

Although comparing rGO with differing levels of oxidation offers insight into whether carbon oxidation causes SD in this carbon, CR is another significant contributor to SD for porous materials[40–47]. Because both oxidized and unoxidized rGO undergo the same charging and SD procedure, these carbons will experience identical CR effects; both carbons will become more fully charged with each cycle, as illustrated in Fig. 7.3.

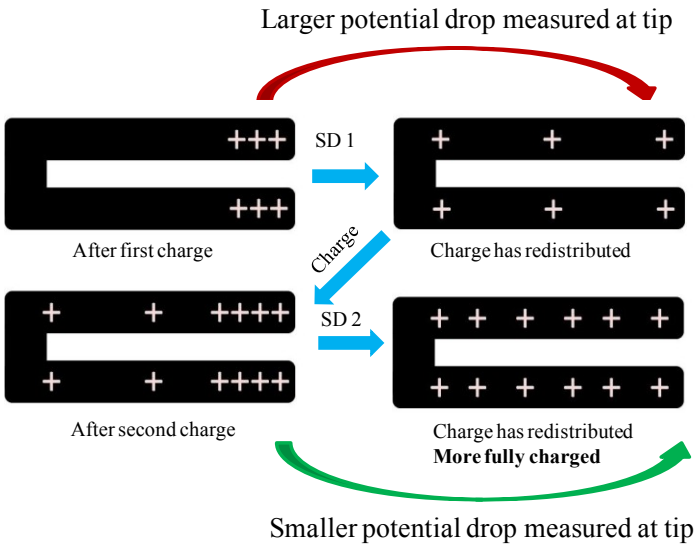

Figure 7.3. Illustration depicting how charge redistribution can result in an electrode becoming more fully charged with each consecutive charge/SD cycle.

Since oxidized rGO should not undergo significant oxidation, the majority of its SD can likely be attributed to CR. However, it is difficult to ascertain whether CR or carbon oxidation is dominating the SD of unoxidized rGO, since both these processes are expected with rGO (possibly simultaneously) and generate similar SD profiles[36,40]. Thus, carbons with CR-reset steps prior to each charge/SD cycle were also investigated. The CR reset serves to remove any charge that redistributed deep into rGO's pores during SD, thereby preventing the carbon from becoming more fully charged with each cycle and ensuring the same amount of CR takes place during every SD cycle. When CR is kept constant, any resulting differences in SD must be due to differences in the degree of oxidation. Thus, changes to the SD profile with consecutive cycling for rGO without reset CR can be assigned as being predominantly the result of the carbon becoming more fully charged (as a result of CR) or more fully oxidized.

Representative SD profiles of unoxidized and oxidized rGO, with and without reset CR, and plotted versus log(t) and $t^{1/2}$, are presented in Figure 7.4. Applying

Conway's method of analysis, the linear potential drop observed versus log(t) preceded by a potential plateau (Fig. 7.4a, b, c, and d), is characteristic of either SD due to an activation-controlled process[37–39] or SD due to CR[40]. Most likely, for unoxidized rGO in this scenario, SD results from a combination of both processes. The absence of linearity with $t^{1/2}$ (Fig. 7.4e, f, g, and h) negates the possibility of a diffusion-controlled Faradaic reaction as the SD mechanism[37–39].

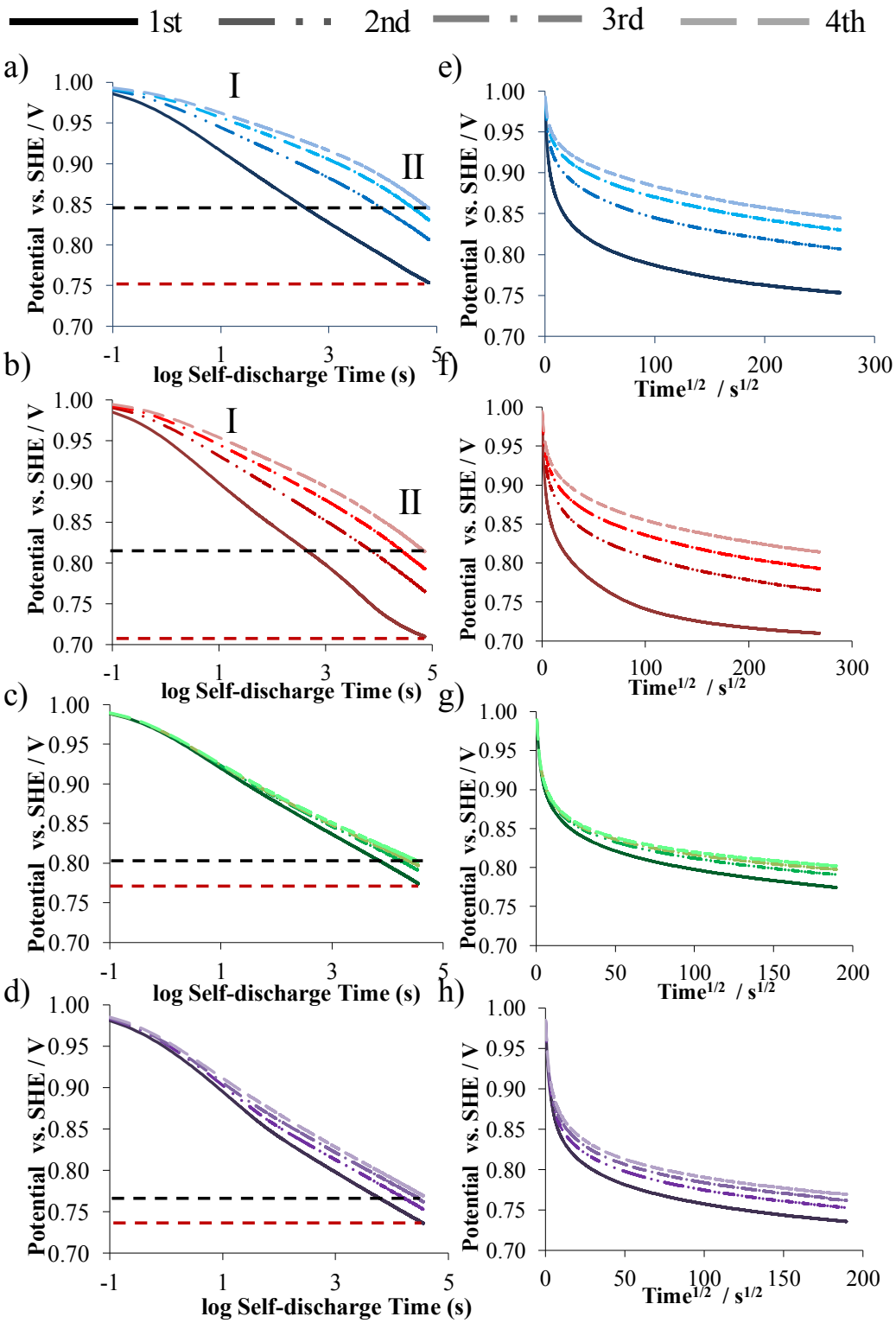

Figure 7.4. Potential decay plotted vs. log(t) (a-d) and $t^{1/2}$ (e-h) during four consecutive SDs of a representative oxidized (a and e), unoxidized (b and f), oxidized CR-reset (c and g), and unoxidized CR-reset (d and h) rGO electrode. Red and black dashed lines indicate the final potential reached during SD 1 and 4, respectively.

Because the unoxidized carbons have available sites for oxidation, these materials exhibit greater SD than their oxidized analogues (comparing Fig. 7.4a to b and Fig. 7.4c to d), evidenced by faster potential decay and lower final potentials when comparing the same SD cycle. This indicates carbon oxidation is playing a role in rGO SD and that the SD can be minimized if the carbon is oxidized prior to use. Interestingly, when CR is reset, the carbons experience similar degrees of SD in all cycles, whether they are oxidized or not (comparing Fig. 7.4c to d, and repetitive cycles within one panel), suggesting CR is the dominant SD mechanism, with oxidation playing a minor role, evidenced by the slightly greater SD of the unoxidized carbons (Fig. 7.4c vs. d).

The slight increase in final potential from SD 1 to 4 observed with the CR-reset experiments (Fig. 7.4c and d) suggests either some oxidation is still occurring or that the 20 hour hold implemented between each charge/SD cycle is insufficient to completely eliminate variation in the CR effects. To verify whether the 20 hour hold sufficed to fully reset the CR effects, an identical SD experiment was conducted with a 40 hour hold time between each cycle (Fig. 7.5); doubling the hold time will have no impact on SD if oxidation is responsible for the slight SD difference between cycles, but will reduce or eliminate the differences if they are due to CR. Since raising the hold time by a factor of two does not significantly change the differences in final SD potentials, these differences between cycles are not from CR, but are likely due to some slight carbon oxidation, perhaps at regions deep in the pores that were not accessed during cycling. These results also show that a 20 hour hold at 0.6 V effectively resets the CR between SD measurements.

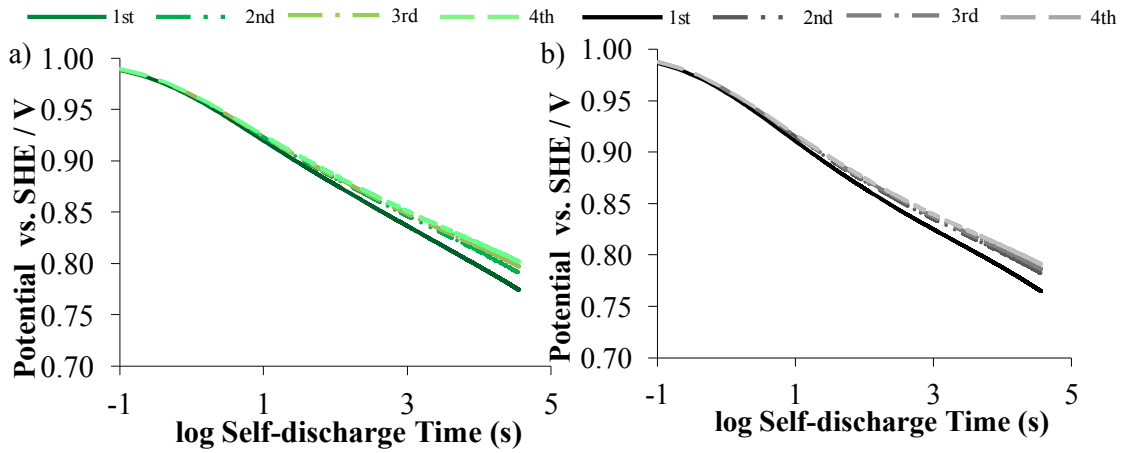

Figure 7.5. SD profile of an oxidized carbon with a CR-reset hold at 0.6 V for a) 20 hours and b) 40 hours.

As previously mentioned, oxidized carbon had its active sites already consumed, and is thus not susceptible to significant oxidation during SD. Nonetheless, both oxidized carbon types still undergo significant SD, with the SD being more severe, especially in later cycles, for the carbon with its CR reset (Fig. 7.4). Likewise, although the unoxidized carbons are equally prone to oxidation, those with reset CR undergo much greater SD in their later cycles than their analogues that are more fully charged in the later cycles; carbons with reset CR show similar potential loss during each SD, while carbons without reset CR undergo less SD with each consecutive cycle (Fig. 7.4). In fact, the SD profiles differ more between carbons with different degrees of CR than between those with varying degrees of oxidation. If site-limited oxidation was the primary cause of SD, oxidized rGO should show a similar and minor potential loss whether its CR was reset or not, and both types of unoxidized carbon should show a greater variation in final potential with repetitive cycling as their active sites are consumed. Since this is not observed in the data, it is convincing that although there is a contribution from carbon oxidation, the SD of rGO is primarily controlled by CR. The decrease in SD with each

consecutive cycle for carbons without their CR reset is likely the result of the rGO becoming more fully charged (the potential in its pores rising) as charges redistribute down its pores.

Figure 7.6 displays replicates of the first and last SDs for various types of rGO. Interestingly, the first SDs of all the carbons are similar, with unoxidized carbons displaying slightly accelerated potential decays, as expected. By SD 4, the SD profiles of carbons with their CR reset cannot be distinguished, no matter what their degree of oxidation was initially. In addition, rGO with reset CR experiences much more SD in its final cycle compared to its analogues that can gain more charge with each charge/SD. This further supports redistribution of charge as the primary cause for SD in rGO; eliminating CR as a variable results in indistinguishable SD profiles independent of degree of oxidation. Carbons with their CR reset undergo nearly identical SD with repetitive charge/SD cycling because they experience an identical amount of CR during every SD.

In contrast, carbons that do not have their CR reset between each cycle become more fully charged with each cycle (Fig. 7.3). Consequently, the potential within their pores increases as cycling continues. In cycle 1, a large potential gradient exists between the pore base and mouth, so the rGO loses significant potential as CR occurs. By the next cycle, charge has redistributed and a smaller potential gradient exists within the pores. Thus, less potential is lost as CR takes place in this cycle, explaining the decrease in degree of SD in the later cycles for carbons without reset CR.

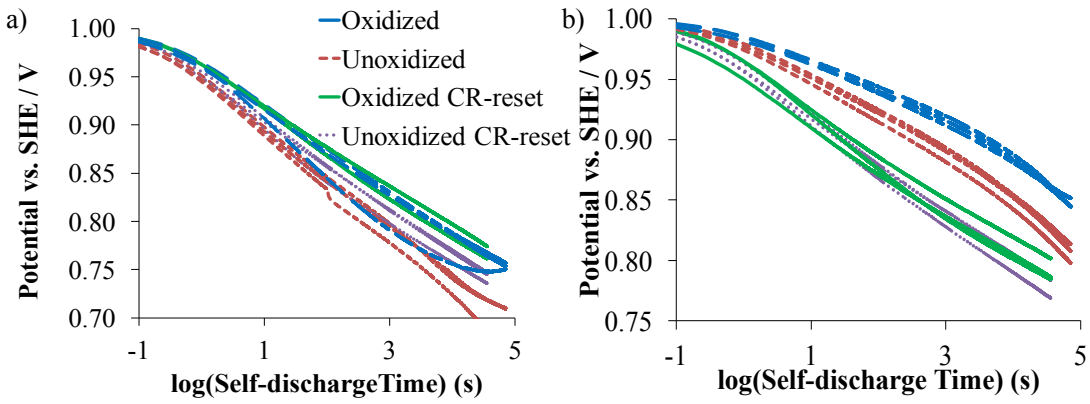

Figure 7.6. Replicates of SD cycles 1 (a) and 4 (b) for all electrode conditions.

Unlike the CR-reset carbons, carbons without reset CR show final SD profiles that differ depending on their initial degree of oxidation; unoxidized carbons show more severe potential loss. By the final cycle, unoxidized rGO should be significantly oxidized from the time spent at high potentials during the preceding SDs. Thus, the difference in degree of SD observed for unoxidized vs. unoxidized rGO in SD 4 cannot be explained by varying susceptibilities to oxidation. In order to explain the differing SD profiles, both oxidation and CR must be considered in unison.

During SD, oxidized carbons will not lose significant charge from carbon oxidation at the surface because their active sites have already been consumed. So, essentially all the charge added to oxidized rGO can redistribute, raising the potential throughout the material, and further oxidation of oxidized rGO will only occur much later in the SD once the charge has migrated sufficiently deep within the pores. On the contrary, during unoxidized rGO SD, carbon oxidation occurs immediately resulting in electrons that enter the carbon and cancel some of the positive charge. Thus, some charge has already been removed from these carbons, resulting in less charge available to redistribute down the pores, meaning a smaller potential after equilibration than that for oxidized carbons. Because of the lower potential within the pores of the unoxidized rGO,

it will experience greater potential loss as CR occurs during subsequent SDs than oxidized rGO.

Ultimately, these results highlight that although repetitive charge/SD cycling of carbon-based ECs can minimize SD via decreasing the potential lost to CR, carbons that are oxidized initially will retain more charge with each cycle than unoxidized carbons. This is an important consideration for the development of rGO-based ECs. Both cycling to steady-state and full oxidation of the carbon electrodes should be completed before they are used in commercial devices.

In Fig. 7.4 the potentials of all carbons fall relatively linearly following the initial plateau. However, carbons without their CR reset exhibit an increase in slope later in the SD (~10^4 seconds). A slope increase signifies the SD mechanism is changing and that charge loss is faster than it would be if the initial process responsible was the sole contributor to SD. The SD accelerates at more comparable times than potentials, inconsistent with a new Faradaic reaction taking over the SD. Moreover, a faster potential decay at a lower potential cannot correspond to an increased reaction rate or a new redox reaction starting because a lower potential means less energy to drive these reactions; a drop in potential would cause charge transfer to happen slower, or simply discontinue.

These results point to CR as the most plausible explanation for the heightened potential decline and allow a mechanism to be proposed. Likely, the SD slope increases once positive charge has redistributed deep enough within the rGO's pores to raise the potential there sufficiently to promote oxidation (Fig. 7.7); oxidation can occur at active sites at the depths not accessed during the relatively rapid charging step. These depths are also inaccessible with CV cycling, rendering oxidized and unoxidized rGO equally

susceptible to oxidation at this location and explaining the similar SD profiles observed for these carbons.

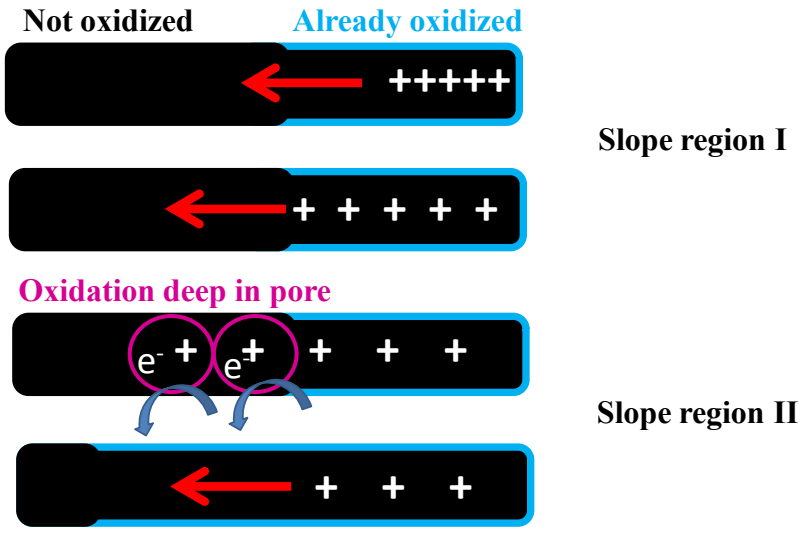

Figure 7.7. Illustration depicting how CR resulting in oxidation deep in the pores of rGO could result in a faster rate of potential loss.

Remarkably, the slope change is absent from the profiles of carbons that had their CR reset. This can be explained by considering the low potential hold used to reset the CR in these carbons. During the CR reset, all of the charges from previous charge/SD cycles are removed. Therefore, even as charges redistribute during the following SD, the potential within the pores of CR-reset rGO likely cannot be raised as high as it can for rGO without reset CR; the significantly larger potential gradient within CR-reset carbons allows CR to dominate their entire SD. Thus, the rate of potential loss for CR-reset rGO is controlled by the same mechanism throughout the entire SD and no change in SD rate is observed.

7.4 Conclusions

Numerous literature reports find carbon-based ECs show increased SD with increasing concentration of heteroatoms present on the carbon surface[7,51–54]. Since carbon

oxidation has been identified as a cause for SD in carbon cloth[36], it is likely oxidation is contributing to SD for many other carbons. This work indicates that carbon oxidation indeed plays a role in rGO SD, evidenced by unoxidized rGO showing greater SD than its already-oxidized counterparts. Nonetheless, oxidized rGO still shows a considerable degree of SD, even though it is not susceptible to significant oxidation, highlighting a different mechanism as the dominant cause for rGO SD. Herein, CR is identified as the primary SD mechanism of rGO in acidic-aqueous electrolyte.

Oxidized carbons with their CR reset before each SD lose much more charge than those without their CR reset. By including a CR-reset step, any positive charges that redistributed to the depths of the pores during SD are removed, but without the CR reset carbons become more fully charged with each SD. This is because the positive charge that redistributed down the carbon's pores remains there while more charge is added to the carbon during the following cycle. This also explains why the SD slope change is absent in the profiles of carbons with reset CR; significant charge is removed during the CR reset step, meaning that as charges redistribute during SD, the potential at the depths of the pores of CR-reset rGO is not raised as high as it is in rGO without reset CR. The potential within the pores of CR-reset rGO is much lower at the beginning of the SD, allowing CR to dominate the entire SD of CR-reset rGO as a consequence of the larger potential gradient within these carbons. When CR is reset, the depths of the carbon remain at the same low potential prior to starting every charge/SD cycle and cannot become more fully charged as cycling continues. Therefore, these carbons experience identical CR effects during each cycle, generating very similar SD profiles with consecutive cycling.

Ultimately, these findings highlight that although high-surface-area carbons are of interest for ECs, their narrow, long, and often twisting pores can result in significant SD due to CR. Furthermore, the results identify carbon oxidation as a cause of SD for rGO and address how critical the impact of CR is on SD in rGO. By evaluating rGO electrodes in a three-electrode setup and employing a method of separating carbon oxidation from CR, this work provides a deeper understanding of SD in rGO that can aid in reducing device SD and designing better, more reliable ECs.

Chapter 8 Conclusions and Future Work

8.1 Conclusions

8.1.1 Impact of Degree of Hydration on the Electrochemical Performance of Manganese Oxide Films

The comprehensive analysis of how the degree of hydration of MnOx influences a vast scope of electrochemical properties presented in this thesis allowed for an innovative MnOx film synthesis combining the advantages of both hydrous and heat-treated MnOx to be designed. Films made via this double-deposition synthesis demonstrate enhanced properties across all parameters critical to EC performance, including energy storage and delivery, power and rate capability, and stability, effectively offering the benefits of both hydrous and heat-treated MnOx while minimizing their drawbacks.

The degree of hydration of transition metal oxide films is known to increase capacitance by facilitating the cation movement required for pseudocapacitive charge storage[2,28,34,65], but its effect on other parameters that impact device performance, such as film usage, EE, and CE, had not been thoroughly investigated in one unique system prior to this work. Hydrous MnOx outperforms heat-treated MnOx in the energy storage domain through offering elevated film usage, capacitance, and energy. This means a device powered by hydrous films could store more charge than a device of the same size and volume powered by anhydrous films and could operate for longer before needing to be recharged. Moreover, maximizing hydration through wet storage prevents film chipping, enhancing physical stability, and wet-stored films impart higher CEs, indicating more of the charge stored on hydrous films is available to power a device.

On the other hand, heat-treated films are preeminent in power-related functions. The heat treatment imparts a low resistance, similar to literature reports[30–32], but this work suggests the low resistance is primarily the result of an improved MnOx-substrate connection, rather than the improved electronic conductivity of films lacking water content[26,33]. This is because low resistance is achieved when the layer of MnOx in direct contact with the substrate is oven-dried, independent of the thickness of this layer; if resistance was largely controlled by the ability of the MnOx to transport electrons, resistance should be inversely related to the fraction of heat-treated film. These findings highlight heat treatment, while detrimental to pseudocapacitive charge storage, is likely necessary to ensure a strong MnOx adherence to the smooth substrate and to keep electrode resistance to a minimum. The decreased resistance achieved through a better connection allows for high EE, meaning less wasted energy, and increased power and rate capabilities suitable for the applications in which ECs are typically used.

When evaluated in an expanded potential window of 0.0-1.0 V, 10:90 and 200 °C oven-dried films function well while their fully hydrous counterparts promptly delaminate from the stainless steel. Additionally, because power and energy are related to the operating voltage of the device[9,15,113], wet single-deposition films are clearly limited by their instability in wider windows, rendering them impractical for use in commercial ECs. Nevertheless, the loss of active material from heat-treated films as a result of film chipping during drying is also undesirable.

The systematic evaluation of how drying/storage procedures influence important electrochemical parameters that affect EC performance provide guidance for any group desiring to create MnOx-based electrodes. The findings discussed herein allow for the

intelligent choice of a drying/storage method best suited for the desired application of the device based on what figures of merit are most advantageous for that application. However, it is evident from the data presented in Chapter 4 that both hydrous and anhydrous films possess unique advantages and disadvantages and that no one drying/storage method results in optimal performance when all parameters critical to a good EC are considered.

The high energy vs. low resistance problem is dealt with through the novel MnOx film synthesis involving both a heat-treated base layer of film and a second layer kept wet presented in Chapter 5. The base layer provides good connection to the current collector, lowering resistance, while the hydrous portion of film boosts pseudocapacitive energy storage. This method, termed the double-deposition method, effectively combines the merits of both hydrous and heat-treated films as long as the ratio of anhydrous to hydrous film is chosen wisely.

Of the various ratios tested, 10:90 films, made with only 10% of their film heat-treated, dominate in terms of electrode performance. 10:90 films demonstrate that as long as a film has significant water content, achieved through having a mostly hydrous film, the high capacitance, energy, CE, and film usage of fully hydrous films can be attained without sacrificing the low resistance and high rate capabilities of the fully heat-treated films. This is because the thin heat-treated layer provides adequate adherence to the current collector while being thin enough as to not significantly hinder pseudocapacitive charge storage. These results not only confirm the advantages of hydrous and anhydrous films can be achieved simultaneously, but also highlight the importance of a solid film-substrate connection that can be achieved via heat treatment. Moreover, the 10:90 double-

deposition method provides a decreased degree of SD compared to both fully hydrous and fully anhydrous single-deposition films, indicating these electrodes would have an extended shelf life and be more reliable to power a critical device in a time of need, such as an emergency exit door[12], after spending significant time resting idle.

While the results discussed in Chapters 4 and 5 confirm the advantages of both hydrous and anhydrous MnOx can be combined to optimize device performance, it is important to note work still needs to be done to address stability concerns during long-term cycling for these electrodes before they can be used in commercial applications. Like many other MnOx electrodes[9,20–25], all electrode conditions have resulted in some form of dissolution, observable as discoloured electrolyte or precipitate and Mn deposits on the counter electrode. Additionally, these MnOx films show changes with cycling; currently, changes as a result of oxidation (film dissolution or irreversible film conversion) and changes that arise from CR effects cannot be distinguished. Likely, all three are taking place in the system under study. Nonetheless, this comprehensive evaluation of a wide selection of electrochemical properties and how film hydration influences them proves valuable to progressing the development of MnOx as a cheaper, more abundant, and environmentally friendly alternative[13] to the EC materials currently in use.

8.1.2 Separating the Roles of Carbon Oxidation and Charge Redistribution as Causes for Self-Discharge in Reduced Graphene Oxide Electrodes

The second project of this thesis advances the current understanding of the role both carbon oxidation and CR play in promoting SD in rGO in aqueous electrolyte through examining the carbon in a three-electrode setup. CR effects have a significant impact on SD in high-surface-area carbons[40–46], as well as in rGO-based full-cell ECs

with organic electrolyte[47]. Other than Subramanian's recent work[47], SD of graphene-based materials is considered underexplored[15], including investigation of rGO SD in water-based electrolytes where carbon oxidation poses a concern.

In acidic-aqueous electrolyte, carbon oxidation has recently been shown to instigate carbon SD[36], but whether and how oxidation impacts rGO SD had not been determined prior to this study. The work presented in Chapters 6 and 7 confirms both CR and carbon oxidation influence rGO SD, and a novel method designed to separate these two phenomena identifies CR as the dominating factor, but establishes the effect of oxidation cannot be ignored. I_f measurements highlight the cycling method employed to oxidize the rGO creates potential gradients within the material that impact the currents required to maintain the carbon at a desired potential.

At high potentials, unoxidized rGO shows higher I_fs, consistent with the greater concentration of active sites for oxidation on this carbon. However, at 0.8 V, which is sufficiently high to promote oxidation, oxidized rGO shows higher initial I_fs than its unoxidized analogues, indicating that another phenomenon must contribute to the I_f profile of this carbon since it is already oxidized. Thus, the elevated I_fs for oxidized carbon can only be explained by CR; charge removed from the preceding cycling to 0 V needs to be replaced at the onset of the hold to maintain the desired potential. This is an important consideration for any group comparing literature SDs where different charging methods were employed or where other electrochemical techniques (*e.g.* cycling to steady state) were performed prior to open-circuit measurements.

Stepping the rGO to below its OCP prior to the I_f experiment creates a depletion zone in the pores where the potential is below OCP and the I_f potential. Dips in the I_f

profile of unoxidized carbons, where the I_f starts positive, rapidly switches to negative, and then remains negative while decreasing in magnitude, suggest CR contributes to the recorded I_f. The initial positive current compensates for the charges moving to raise the potential of the depletion zone generated from the discharge employed before charging. The current switches sign once positive charge from the base of the pores (at OCP and above the hold potential) reaches the surface, requiring cancellation to maintain the potential at the surface below OCP. This theory is consistent with data collected with a transmission line circuit model pore; positive currents are recorded for the model pore at a voltage below the simulated OCV when the voltage of capacitors past the pore mouth are below the hold voltage (*i.e.* a depletion zone exists) (Chapter 6). Negative currents result when the voltages on capacitors deep within the circuit remain near OCV and feed charge up through the circuit causing the voltage of the capacitors representing the pore base to fall while voltages near the pore mouth rise, until the entire pore reaches equilibrium (Chapter 6).

The clear impact CR has on rGO I_fs complicates analysis of how carbon oxidation influences SD. For unoxidized rGO, positive I_fs at high potentials could be explained by both phenomena, with no way to distinguish them. Oxidized carbons highlight CR can occur for a significant time, evidenced by the positive I_fs recorded for these carbons at high potentials even though they cannot undergo significant oxidation. Thus, the preliminary results collected via the I_f method inspired the experimental design used to separate carbon oxidation and CR in open-circuit SD measurements.

Similar to I_f measurements, separation of SD due to CR and SD as a result of oxidation poses a challenge in typical open-circuit SD evaluations. In these SD

measurements, both activation-controlled Faradaic SD[37–39] and SD due to CR[40] produce the same potential profile: a linear decay with log(t). Since the porosity and presence of functional groups on rGO[73–75] make the material susceptible to both oxidation and substantial CR effects, both of which contribute to the SD of carbons[36,40–47], a method of isolating SD effects from both phenomena is critical in understanding and preventing graphene-based EC SD.

In open-circuit potential SD measurements (Chapter 7), unoxidized rGO shows more severe SD compared to its oxidized analogues, yet all carbons show a significant decrease in SD with repetitive charge/SD cycling, whether they are oxidized or not. In the case of unoxidized rGO, this trend can be the outcome of either the consumption of active oxidation sites[36] or the result of the material becoming more fully charged with cycling[46]. Employing the CR reset method described in this work eliminates differences in state-of-charge as a cause for any changes in SD, allowing for the SD due to oxidation to be isolated and the dominant cause for SD in rGO to be determined. In this method, the potential gradient within the pores of rGO is reset prior to each charge/SD cycle by holding the rGO at 0.6 V for 20 hours. The low-potential hold removes any charge that had redistributed down the carbon's pores during the preceding SD, without inducing extra carbon oxidation, thereby allowing differences resulting from varying levels of oxidation between carbons to be isolated. With this method, CR was determined to be the primary cause for a decrease in SD with repetitive cycling for rGO; CR-reset rGO displays a similar potential loss with repetitive cycling and substantially more charge loss in its later cycles compared to its counterparts, which become more fully charged with each SD.

Nonetheless, unoxidized rGO consistently shows greater potential loss than oxidized rGO, confirming that the contribution from carbon oxidation to SD is important and merits careful consideration. It is evident that in order to minimize SD in rGO effectively, the carbon should be both fully oxidized and subjected to repetitive charge/SD cycling to sufficiently to eliminate potential gradients within the material that result in potential loss due to CR. In addition, the novel CR reset experiment designed to separate oxidation effects from those of CR proves useful in identifying the primary cause of SD in a system and determining if both processes play a role, and can be applied to other systems where both oxidation and CR are likely to occur.

Furthermore, open-circuit potential SD experiments highlight SD due to carbon oxidation and SD due to CR are related; as positive charge redistributes through the carbon, the potential deep within its pores will rise, eventually causing oxidation to take place at this depth. Once oxidation and CR occur in unison at great pore depths, potential loss accelerates; this is evidenced as an increase in slope when potential is plotted vs. log(t) for carbons without reset CR.

This work is pivotal in the expansion of our understanding of SD in rGO and provides a method to separate SD due to oxidation and SD due to CR. This bears significance since both processes present similar SD profiles, similar changes in SD with cycling[36,40], and are likely both occurring in many other carbons currently under investigation as EC materials. To effectively reduce SD in rGO and maximize its potential for use in commercial applications, the carbon should be both fully oxidized and cycled to steady state to ensure minimal potential loss to CR and oxidation following charging.

8.2 Future Work

While the innovative double-deposition synthesis offers a simple method to significantly enhance the performance of MnOx films, thoughtful expansion of the double-deposition method would prove beneficial in bringing MnOx closer to being used in commercial ECs. Likewise, while identification of both carbon oxidation and CR as causes of rGO SD in acidic-aqueous electrolyte is an important contribution to the development of more reliable devices, a deeper understanding of the oxidation process is of utmost importance to minimize rGO SD.

With respect to the MnOx project, addressing the stability of MnOx films is a necessary next step. While the double-deposition method provides enhanced stability over a variety of single-deposition drying/storage conditions through preventing chipping, cracking, and delamination, the extended cycling in the 0-1.0 V window confirmed these films still dissolve and occasionally degenerate. However, since ECs are expected to endure hundreds of thousands of cycles, before MnOx can properly serve as a cheap, abundant, and environmentally benign substitute for other EC materials, improving its stability requires exploration.

Certainly, the MnOx film is not the only component that contributes to the stability of the electrode during cycling; how the electrolyte contributes to MnOx dissolution and substrate effects also require consideration. Komaba and coworkers suggest adding buffer species such as $NaHCO_3$ and Na_2HPO_4 to electrolyte can suppress MnOx dissolution, likely through minimizing local pH changes near the MnOx surface that promote dissolution[23,133]. They propose the insoluble nature of the salts of Mn^{2+} and the buffer anions also help reduce dissolution[23]. Of course, testing and optimizing the

10:90 double-deposition with other substrates is also a viable next step to improve stability and practicality. While stainless steel serves as an ideal substrate for the quick visual analysis of physical stability of MnOx films necessary for this work, rougher surfaces commonly used with MnOx, such as nickel foam[67,134,135], should facilitate a better MnOx-substrate connection and provide a higher surface area to enhance charge storage. Investigation of 10:90 films in electrolyte with additives analogous to Komaba's[23,133] and on rougher substrates is a feasible route to bring the fundamental work discussed herein closer to use in a commercial EC. In addition, since SEM images reveal increasing the drying temperature increases the severity of film cracking, but films heat-treated at 100 °C display resistances comparable to those dried at 200 °C, finding a lower heat-treatment temperature at which a good substrate-MnOx connection is achieved while minimizing film cracking could also improve stability. Moreover, as these films, like other MnOx films in the literature[46,113], show relatively modest film usage ratios, identifying just how thin these films can be made so that they offer high usage ratios and waste less material without sacrificing energy storage capability is a reasonable route to improving MnOx's practicality and usefulness for applications in energy storage.

Regarding the rGO project, results confirm CR plays a significant role in controlling how much SD rGO experiences[47], as it does with many other porous materials[40–46]. A reasonable path to follow is designing an experiment that could serve as an electrode pre-treatment to reduce SD. This proves challenging because although oxidizing the carbon at great pore depths could be achieved through applying an extended potential hold at high potentials or using a slower sweep rate CV, the latter has destroyed the carbon under study in our lab. Thus, it is clear considerable thought must be put into

experimental design to try to develop a method of suppressing SD via minimization of both CR and carbon oxidation without using harsh conditions that destroy the material.

Secondly, identifying which particular surface functionalities are primarily responsible for carbon SD is also relevant to this work. If certain carbon treatments could result in selective elimination of these groups, then a relationship between concentration of specific surface functionalities and degree of SD could be determined. This would prove to be a lengthy study since the functional groups on specific rGO samples would have to be identified and quantified prior to being correlated to degree of SD. In the long-term, a suitable future step would be to optimize synthesis methods of carbons to maximize energy storage by optimizing pore size to allow for a high surface area without having such narrow, winding pores that significant charge is lost to CR, and without a surplus of detrimental surface groups. Therefore, control of surface oxides coupled with a balance between a surface area high enough to store considerable charge without having overly narrow and deep pores that take charge from the surface by means of CR is an important experimental route. While of significant importance, this would be a challenging, largely synthetic project that is beyond the scope of this lab.

References

(1) Conway, B. E. *J. Electrochem. Soc.* **1991**, *138* (6), 1539.

(2) Conway, B. E. *Electrochemical Supercapacitors: Scientific Fundamentals and Technological Applications*; Kluwer Academic/Plenum Publishers: New York, 1999.

(3) Conway, B. E.; Birss, V.; Wojtowicz, J. *J. Power Sources* **1997**, *66*, 1–14.

(4) Conway, B. E.; Pell, W. G. *J. Solid State Electrochem.* **2003**, *7*, 637–644.

(5) Winter, M.; Brodd, R. J. *Chem. Rev.* **2004**, *104*, 4245–4269.

(6) Frackowiak, E.; Béguin, F. *Carbon* **2001**, *39*, 937–950.

(7) Pandolfo, A. G.; Hollenkamp, A. F. *J. Power Sources* **2006**, *157*, 11–27.

(8) Frackowiak, E. *Phys. Chem. Chem. Phys.* **2007**, *9*, 1774.

(9) Wang, G.; Zhang, L.; Zhang, J. *Chem. Soc. Rev.* **2012**, 797–828.

(10) Miller, J. R.; Burke, A. F.; Miller, J. R.; Burke, A. F.; Burke, A. F. *Electrochem. Soc.* **2008**, *17*, 53–57.

(11) Zhang, Y.; Feng, H.; Wu, X.; Wang, L.; Zhang, A.; Xia, T.; Dong, H.; Li, X.; Zhang, L. *Int. J. Hydrogen Energy* **2009**, *34*, 4889–4899.

(12) Zhang, L. L.; Zhao, X. S. *Chem. Soc. Rev.* **2009**, *38*, 2520.

(13) Suhasini. *J. Electroanal. Chem.* **2013**, *690*, 13–18.

(14) Liu, T.; Pell, W. G.; Conway, B. E. *Electrochim. Acta* **1997**, *42*, 3541–3552.

(15) Yang, W.; Ni, M.; Ren, X.; Tian, Y.; Li, N.; Su, Y.; Zhang, X. *Curr. Opin. Colloid Interface Sci.* **2015**, *20*, 416–428.

(16) Kötz, R.; Carlen, M. *Electrochim. Acta* **2000**, *45*, 2483–2498.

(17) Gu, W.; Yushin, G. *Wiley Interdiscip. Rev. Energy Environ.* **2014**, *3*, 424–473.

(18) Shi, F.; Li, L.; Wang, X.; Gu, C.; Tu, J. *RSC Adv.* **2014**, *4*, 41910–41921.

(19) Long, J. W.; Bélanger, D.; Brousse, T.; Sugimoto, W.; Sassin, M. B.; Crosnier, O. *MRS Bull.* **2011**, *36*, 513–522.

(20) Wei, W.; Cui, X.; Chen, W.; Ivey, D. *Chem. Soc. Rev.* **2011**, *40*, 1697–1721.

(21) Reddy, R. N.; Reddy, R. G. *J. Power Sources* **2003**, *124*, 330–337.

(22) Yan, J.; Khoo, E.; Sumboja, A.; Lee, P. S. *ACS Nano* **2010**, *4*, 4247–4255.

(23) Komaba, S.; Tsuchikawa, T.; Tomita, M.; Yabuuchi, N.; Ogata, A. *J. Electrochem. Soc.* **2013**, *160* , A1952–A1961.

(24) Wei, W.; Cui, X.; Chen, W.; Ivey, D. G. *Electrochim. Acta* **2009**, *54*, 2271–2275.

(25) Pang, S.; Anderson, M. A.; Chapman, T. W. *J. Electrochem. Soc.* **2000**, *147*, 444–450.

(26) Chang, J.; Chen, Y.; Tsai, W. *J. Power Sources* **2004**, *135*, 344–353.

(27) Ragupathy, P.; Vasan, H. N.; Munichandraiah, N. *J. Electrochem. Soc.* **2008**, *155*, A34–A40.

(28) Ghaemi, M.; Ataherian, F.; Zolfaghari, A.; Jafari, S. M. *Electrochim. Acta* **2008**, *53*, 4607–4614.

(29) Chun, S. E.; Pyun, S. Il; Lee, G. J. *Electrochim. Acta* **2006**, *51*, 6479–6486.

(30) Chen, Y.; Wang, J. W.; Shi, X. C.; Chen, B. Z. *Electrochim. Acta* **2013**, *109*, 678–683.

(31) Chang, J.-K.; Tsai, W.-T. *J. Electrochem. Soc.* **2005**, *152*, A2063–A2068.

(32) Dolah, B. N. M.; Deraman, M.; Suleman, M.; Othman, M. A. R.; Jasni, M. R. M.; Nor, N. S. M. *Int. J. Electrochem. Sci.* **2017**, *12*, 2466–2484.

(33) Kim, H.; Popov, B. N. *J. Electrochem. Soc.* **2003**, *150*, D56–D62.

(34) Jang, G.; Tsai, E.; Rajeshwar, K. *J. Electroanal. Chem.* **1989**, *263*, 383–397.

(35) Rolison, D. R.; Hagans, P. L.; Swider, K. E.; Long, J. W. *Langmuir* **1999**, *15*, 774–779.

(36) Oickle, A. M.; Tom, J.; Andreas, H. A. *Carbon* **2016**, *110*, 232–242.

(37) Conway, B. E.; Pell, W. G.; Liu, T. *J. Power Sources* **1997**, *65*, 53–59.

(38) Niu, J.; Pell, W. G.; Conway, B. E. *J. Power Sources* **2006**, *156*, 725–740.

(39) Niu, J.; Conway, B. E.; Pell, W. G. *J. Power Sources* **2004**, *135*, 332–343.

(40) Black, J.; Andreas, H. A. *Electrochim. Acta* **2009**, *54*, 3568–3574.

(41) Black, J. M.; Andreas, H. A. *J. Phys. Chem. C* **2010**, *114*, 12030–12038.

(42) Black, J.; Andreas, H. A. *J. Power Sources* **2010**, *195*, 929–935.

(43) Kaus, M.; Kowal, J.; Sauer, D. U. *Electrochim. Acta* **2010**, *55*, 7516–7523.

(44) Kowal, J.; Avaroglu, E.; Chamekh, F.; Senfelds, A.; Thien, T.; Wijaya, D.; Sauer, D. U. *J. Power Sources* **2011**, *196*, 573–579.

(45) Graydon, J. W.; Panjehshahi, M.; Kirk, D. W. *J. Power Sources* **2014**, *245*, 822–829.

(46) Andreas, H. A.; Black, J. M.; Oickle, A. A. *Electrochim. Acta* **2014**, *140*, 116–124.

(47) Subramanian, S.; Akkaraparambil Johny, M.; Malamal Neelanchery, M.; Ansari, S. *IEEE Trans. Power Electron.* **2018** [Online early access]. DOI: 10.1109/TPEL.2018.2810889. Published online: Feb 28, 2018. https://ieeexplore.ieee.org/document/8304821/ (accessed Mar 1, 2018).

(48) Yaniv, M.; Soffer, A. *J. Electrochem. Soc.* **1976**, *123*, 506–511.

(49) Pell, W. G.; Conway, B. E.; Adams, W. A.; De Oliveira, J. *J. Power Sources* **1999**, *80*, 134–141.

(50) de Levie, R. *Electrochim. Acta* **1963**, *8*, 751–780.

(51) Lota, G.; Frackowiak, E. *Fuel Cells* **2010**, *10*, 848–855.

(52) Kierzek, K.; Frackowiak, E.; Lota, G.; Gryglewicz, G.; Machnikowski, J. *Electrochim. Acta* **2004**, *49*, 515–523.

(53) Zhang, Q.; Cai, C.; Qin, J.; Wei, B. *Nano Energy* **2014**, *4*, 14–22.

(54) Hsieh, C. T.; Teng, H. *Carbon* **2002**, *40*, 667–674.

(55) Wang, J.; Ding, B.; Hao, X.; Xu, Y.; Wang, Y.; Shen, L.; Dou, H.; Zhang, X. *Carbon* **2016**, *102*, 255–261.

(56) Blomquist, N.; Wells, T.; Andres, B.; Bäckström, J.; Forsberg, S.; Olin, H. *Sci. Rep.* **2017**, *7*, 1–7.

(57) Burke, A. *J. Power Sources* **2000**, *91*, 37–50.

(58) Sharma, P.; Bhatti, T. S. *Energy Convers. Manag.* **2010**, *51*, 2901–2912.

(59) Bockris, J.; Reddy, A.; Gamboa-Aldeco, M. *Modern Electrochemistry 2A: Fundamentals of Electrodics*, 2nd ed.; Kluwer Academic/Plenum Publishers: New York, 2000.

(60) Hu, C.; Liu, F.; Lan, H.; Liu, H.; Qu, J. *J. Colloid Interface Sci.* **2015**, *446*, 359–365.

(61) Nagarajan, N.; Cheong, M.; Zhitomirsky, I. *Mater. Chem. Phys.* **2007**, *103*, 47–53.

(62) Nguyen, T.; Boudard, M.; Carmezim, M. J.; Montemor, M. F. *Electrochim. Acta* **2016**, *202*, 166–174.

(63) Wang, J.; Chen, Y.; Chen, B. *J. Alloys Compd.* **2016**, *688*, 184–197.

(64) Toupin, M.; Brousse, T.; Bélanger, D. *Chem. Mater.* **2004**, *16*, 3184–3190.

(65) Vukovic, M.; Valla, T.; Milun, M. *J. Electroanal. Chem.* **1993**, *356*, 81–91.

(66) Long, J. W.; Swider, K. E.; Merzbacher, C. I.; Rolison, D. R. *Langmuir* **1999**, *15*, 780–785.

(67) Zhu, T.; Zheng, S. J.; Chen, Y. G.; Luo, J.; Guo, H. B.; Chen, Y. E. *J. Mater. Sci.* **2014**, *49*, 6118–6126.

(68) Chun, W.; Shin, M.; Choi, B.; Qian, A.; Bae, J.; Chung, C. *Sci. Adv. Mater.* **2016**, *8*, 89–95.

(69) Xue, L.; Hao, H.; Wei, Z.; Huang, T.; Yu, A. *J. Solid State Electrochem.* **2011**, *15*, 485–491.

(70) Chmiola, J. *Science* **2006**, *313*, 1760–1763.

(71) Simon, P.; Gogotsi, Y. *Acc. Chem. Res.* **2013**, *46*, 1094–1103.

(72) Bonaccorso, F.; Colombo, L.; Yu, G.; Stoller, M.; Tozzini, V.; Ferrari, A. C.; Ruoff, R. S.; Pellegrini, V. *Science* **2015**, *347*, 1246501-1–1246501-9.

(73) Dreyer, D. R.; Park, S.; Bielawski, W.; Ruoff, R. S. *Chem. Soc. Rev.* **2010**, *39*, 228-240.

(74) Pei, S.; Cheng, H. M. *Carbon* **2012**, *50*, 3210–3228.

(75) Luo, J.; Kim, J.; Huang, J. *Acc. Chem. Res.* **2013**, *46*, 2225–2234.

(76) Raccichini, R.; Varzi, A.; Passerini, S.; Scrosati, B. *Nat. Mater.* **2014**, *14*, 271–279.

(77) Andreas, H. A. *J. Electrochem. Soc.* **2015**, *162*, A5047–A5053.

(78) Choo, H.; Kinumoto, T.; Nose, M.; Miyazaki, K. *J. Power Sources* **2008**, *185*, 740–746.

(79) Nose, M.; Kinumoto, T.; Choo, H.; Miyazaki, K.; Abe, T.; Ogumi, Z. *Fuel Cells* **2009**, *9*, 284–290.

(80) Siroma, Z.; Tanaka, M.; Yasuda, K.; Tanimoto, K.; Inaba, M.; Tasaka, A. *Electrochemistry* **2007**, *75*, 258–260.

(81) Hong, K.; Cho, M.; Kim, S. O. *ACS Appl. Mater. Interfaces* **2015**, *7*, 1899–1906.

(82) Huang, G.; Zhang, Y.; Wang, L.; Sheng, P.; Peng, H. *Carbon* **2017**, *125*, 595–604.

(83) Amutha, B.; Subramani, K.; Reddy, P. N.; Sathish, M. *Chemistry Select* **2017**, *2*, 10754–10761.

(84) Nishimura, K.; Douzono, T.; Kasai, M.; Andou, H.; Muranaka, Y.; Kozono, Y. *J. Power Sources* **1999**, *81–82*, 420–424.

(85) Ataherian, F.; Lee, K. T.; Wu, N. L. *Electrochim. Acta* **2010**, *55*, 7429–7435.

(86) Gummow, R. J.; de Kock, A.; Thackeray, M. M. *Solid State Ionics* **1994**, *69*, 59–67.

(87) Raut, A. S.; Parker, C. B.; Glass, J. T. *J. Mater. Res.* **2010**, *25*, 1500–1506.

(88) Christen, T.; Carlen, M. W. *J. Power Sources* **2000**, *91*, 210–216.

(89) Leal, M.; Walther, D. C.; Dunn-Rankin, D. *Prog. Energy Combust. Sci.* **2005**, *31*, 422–465.

(90) Liang, C.-H.; Hwang, C.-S. *Japanese J. Appl. Phys. Chem.* **2008**, *47*, 4682–4686.

(91) Tom, J.; Andreas, H. A. *Carbon* **2017**, *112*, 230–237.

(92) Watts, J. F.; Wolstenholme, J. *An Introduction to Surface Analysis by XPS and AES*; Wiley: West Sussex, 2003.

(93) Sarkar, A.; Kumar Satpati, A.; Kumar, V.; Kumar, S. *Electrochim. Acta* **2015**, *167*, 126–131.

(94) Hu, C.; Tsou, T. *Electrochem. Commun.* **2002**, *4*, 105–109.

(95) Tom, J. The Influence of Carbon-Oxygen Surface Groups and a Water-miscible Primary Alcohol on the Voltammetric Detection of Bovine Hemoglobin in Aqueous Electrolyte using Carbon Electrodes. Ph.D. Dissertation. Dalhousie University, Halifax, NS, 2017.

(96) Cachet-Viviera, C.; Vivier, V.; Cha, C. S.; Nedelec, J. Y.; Yu, L. T. *Electrochim. Acta* **2001**, *47*, 181–189.

(97) Papirer, E.; Lacroix, R.; Donnet, J.; Nanse, G.; Fioux, P. *Carbon* **1994**, *32*, 1341–1358.

(98) Okpalugo, T. I. T.; Papakonstantinou, P.; Murphy, H.; McLaughlin, J.; Brown, N. M. D. *Carbon* **2005**, *43*, 153–161.

(99) Kangasniemi, K. H.; Condit, D. A.; Jarvi, T. D. *J. Electrochem. Soc.* **2004**, *151*, E125–E132.

(100) Kamau, G. N.; Willis, W. S.; Rusling, J. F. *Anal. Chem.* **1985**, *57*, 545–551.

(101) Nkrumah-Amoako, K.; Roberts, E. P. L.; Brown, N. W.; Holmes, S. M. *Electrochim. Acta* **2014**, *135*, 568–577.

(102) Ren, L.; Yang, F.; Li, Y.; Liu, T.; Zhang, L.; Ning, G.; Liu, Z.; Gao, J.; Xu, C. *RSC Adv.* **2014**, *4*, 63048–63054.

(103) Ganguly, A.; Sharma, S.; Papakonstantinou, P.; Hamilton, J. *J. Phys. Chem. C* **2011**, *115*, 17009–17019.

(104) Valdés, H.; Sánchez-Polo, M.; Rivera-Utrilla, J.; Zaror, C. A. *Langmuir* **2002**, *18*, 2111–2116.

(105) Biniak, S.; Szymański, G.; Siedlewski, J.; Światkoski, A. *Carbon* **1997**, *35*, 1799–1810.

(106) Swiatkowski, A.; Pakula, M.; Biniak, S.; Walczyk, M. *Carbon* **2004**, *42*, 3057–3069.

(107) Velo-Gala, I.; López-Peñalver, J. J.; Sánchez-Polo, M.; Rivera-Utrilla, J. *Carbon* **2014**, *67*, 236–249.

(108) Kundu, S.; Wang, Y.; Xia, W.; Muhler, M. *J. Phys. Chem. C* **2008**, *112*, 16869–16878.

(109) Lin, C.-K.; Chuang, K.-H.; Lin, C.-Y.; Tsay, C.-Y.; Chen, C.-Y. *Surf. Coatings Technol.* **2007**, *202*, 1272–1276.

(110) Devaraj, S.; Munichandraiah, N. *J. Electrochem. Soc.* **2007**, *154*, A80–A88.

(111) Tsang, C.; Kim, J.; Manthiram, A. *J. Solid State Chem.* **1998**, *32*, 28–32.

(112) Pourbaix, M. *Atlas of Electrochemical Equilibria in Aqueous Solution*; NACE International: Houston, 1974.

(113) Nam, K.-W.; Kim, M. G.; Kim, K.-B. *J. Phys. Chem. C* **2007**, *111*, 749–758.

(114) Toupin, M.; Brousse, T.; Be, D. *Chem. Mater.* **2002**, *14*, 3946–3952.

(115) Liu, M.; Gan, L.; Xiong, W.; Xu, Z.; Zhu, D.; Chen, L. *J. Mater. Chem. A* **2014**, 2555–2562.

(116) Jacob, G. M.; Zhitomirsky, I. *Appl. Surf. Sci.* **2008**, *254*, 6671–6676.

(117) Brousse, T.; Toupin, M.; Dugas, R.; Athouël, L.; Crosnier, O.; Bélanger, D. *J. Electrochem. Soc.* **2006**, *153*, A2171–A2180.

(118) Wang, Y.; Zhang, D.; Xiang, Z. *J. Taiwan Inst. Chem. Eng.* **2016**, *59*, 547–552.

(119) Guo, S.; Sun, W.; Yang, W.; Li, Q.; Shang, J. K. *RSC Adv.* **2015**, *5*, 53280–53288.

(120) Bleda-Martínez, M.; Lozano-Castelló, D.; Morallón, E.; Cazorla-Amorós, D.; Linares-Solano, A. *Carbon* **2006**, *44*, 2642–2651.

(121) Garten, V.; Weiss, D. *Aust. J. Chem.* **1955**, *8*, 68–95.

(122) Kinoshita, K.; Bett, J. *Carbon* **1973**, *11*, 403–411.

(123) Hallum, J. V; Drushel, H. V. *Sect. Title Fuels Coal Prod.* **1958**, *62*, 110–117.

(124) Drushel, H. V; Hallum, J. V. *J. Phys. Chem.* **1958**, *62*, 1502–1505.

(125) Andreas, H. A.; Conway, B. E. *Electrochim. Acta* **2006**, *51*, 6510–6520.

(126) Gallagher, K. G.; Fuller, T. F. *Phys. Chem. Chem. Phys.* **2009**, *11*, 11557–11567.

(127) Sanecki, P. T.; Skitał, P. M. *Electrochim. Acta* **2008**, *53*, 7711–7719.

(128) Untereker, D. F.; Bruckenstein, S. *Anal. Chem.* **1972**, *44*, 1009–1020.

(129) Boehm, H. P. *Carbon* **1994**, *32*, 759–769.

(130) Willsau, J.; Heitbaum, J. *J. Electroanal. Chem.* **1984**, *161*, 93–101.

(131) Béguin, F.; Presser, V.; Balducci, A.; Frackowiak, E. *Adv. Mater.* **2014**, *26*, 2219–2251.

(132) Guittonneau, F.; Abdelouas, A.; Grambow, B.; Huclier, S. *Ultrason. Sonochem.* **2010**, *17*, 391–398.

(133) Komaba, S.; Ogata, A.; Tsuchikawa, T. *Electrochem. Commun.* **2008**, *10*, 1435–1437.

(134) Hassan, S.; Suzuki, M.; Abd El-Moneim, A. Presented at the First International Conference on Innovative Engineering Systems (ICIES) [Online]. Alexandria, Egypt. December 7-9, 2012. Institute of Electrical and Electronics Engineers Xplore Digital Library. https://ieeexplore.ieee.org/document/6530846/ (accessed Mar 5, 2017).

(135) Pang, M.; Long, G.; Jiang, S.; Ji, Y.; Han, W.; Wang, B.; Liu, X.; Xi, Y. *Electrochim. Acta* **2015**, *161*, 297–304.